University of Piraeus

Department of Industrial Management &Technology

PhD thesis

"Experimental and computational investigation on the mechanical characteristics of a self-setting calcium phosphate bone cement intended for biomedical applications"

Bimis Alexios

Piraeus 2017

Supervisor

Prof. D. Karalekas

University of Piraeus

Jury

Prof. D. Karalekas[**]

University of Piraeus

Prof. S. Kourkoulis[**]

National Technical University of Athens

Prof. D. Manolakos[**]

National Technical University of Athens

Prof. S. Zaoutsos

TEI of Thesally

Prof. D. Sidiras

University of Piraeus

Asst. Prof. I. Giannatsis

University of Piraeus

Asst. Prof. C. Siontorou

University of Piraeus

*** Supervising Committee*

1

Contents

Figures

Tables

Chapter 1

Introduction

1.1. Information about biomaterials and bone cements

From ancient times, humans started to seek solutions to relieve illnesses and heal injuries, wounds, bone fractures/defects etc. Surgical instruments, medicines and other elements, discovered throughout all these years, proved the continuous evolvement of medical field from the early ages of human civilization. Also, an initial development of intervening in the human body by adding materials either for decorative or medical purposes is also evident, such as dental implants that were used to substitute rotten or damaged teeth (Fig. 1.1.). The outburst of technology, in the recent years, led to a strong systematic development of medical field, while a lot of new innovative materials intended for medical reasons (e.g. implants) are being researched, like biomaterials.

Fig. 1.1. : Dental implants, connected in copper "bridges" with the rest teeth, in a discovered ancient skull (**1**).

The term "biomaterials" refers to any material or substance that has been engineered to interact with biological systems for a medical purpose - either a therapeutic (treat, augment, repair or replace a tissue function of the body) or a diagnostic one (2). The field of this class of materials

is quite extended and several examples are illustrated in Fig. 1.2. Some typical biomaterials, such as bone implants, metals plaques, polymers and scaffolds are used in orthopedics, dentistry and cardiology. A useful and widespread category of biomaterials involves ceramics, polymers and glasses, mainly used as bone defect fillers or cements in orthopedics and dentistry, termed as "bone cements".
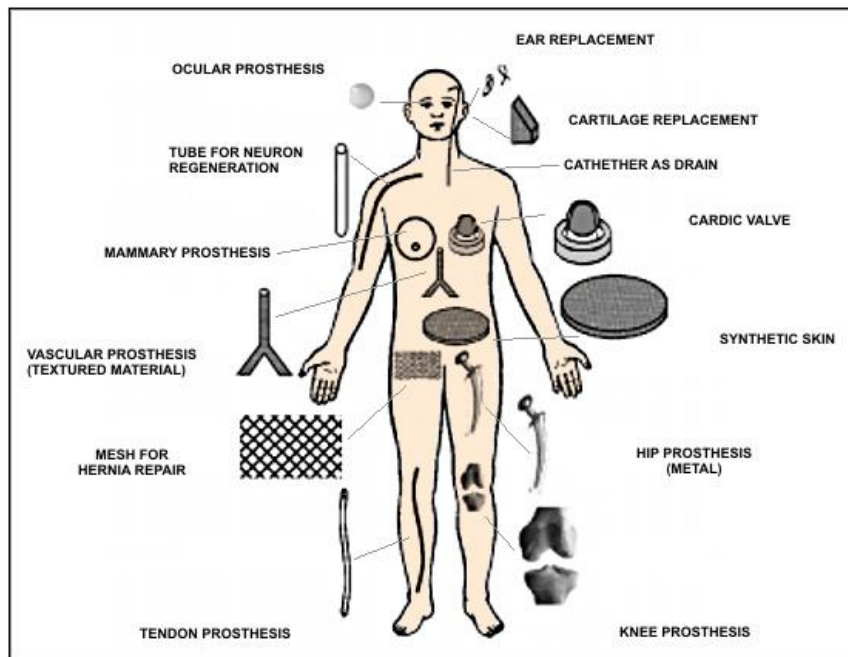
Fig. 1.2 : Various implants or devices, used in cases of diseased or damaged issues or organs (**3**).

The use of bone cements is met in occasions where parts of the human bones are destroyed (e.g car/sport accidents, diseases like cancer etc.), hence the use of proper materials for mechanical support and bone structural integrity is of significant importance. A well-known bone cement is polymethylmethacrylate (PMMA) cement, discovered in the 1950s, which is widely used in various orthopedic and trauma surgery (e.g. total hip arthroplasty-THR). It is consisted of two primary components: (i) a powder consisting of copolymers based on the substance polymethylmethacrylate and (ii) a liquid monomer, methylmethacrylate (MMA). Upon the mixture of these two components, the liquid monomer polymerizes around the pre-polymerized powder particles, forming hardened PMMA (4). During this process heat is generated, due to a strong exothermic reaction between the powder and the liquid. Although the overall mechanical properties of this bone cement are shown to be able to lead to long-term stability

(5), several disadvantages are reported: generation of heat during curing, that causes necrosis of the surrounding tissue (6), exhibited toxicity of the monomer (7), embrittlement of the PMMA bone cement due to aging (8), osteolysis caused by wear debris formation (9) etc.

In 1980s a new promising biomaterial was discovered: Calcium Phosphate Cements (CPCs). This class of materials exhibits excellent biocompatibility, bioactivity, osteoconduction and osteogenesis. Moreover, CPCs are more biocompatible with the human bone than many other ceramic and inorganic nanoparticles (10). For the fabrication of CPCs, a calcium phosphate compound [e.g α or β Tricalcium Phosphate (α/β-TCP), TeTracalcium Phoshate (TTCP)] is mixed with an aqueous solution.

Fig. 1.3 : Classification of the most common calcium phosphate cements, various hardening mechanisms and the resulted final products **(11)**.

The mixture results in a malleable paste that progressively solidifies and subsequently hardens in a liquid media. Water, aqueous solutions of various salts or acid-based solutions are used as hardening liquid of CPCs (12), while a hardening process by sintering CPCs in high temperatures ($>700\ ^0$C) is also reported in the literature (13), (14). Unlike acrylic bone cements, which harden through a polymerization reaction, CPCs set as a result of a dissolution and precipitation process, in the case of hardening in a liquid media. Specifically, 3 stages occur: (a) dissolution of particles of solid phases in the hardening liquid until its saturation, with respect to calcium ions and phosphate ions, (b) interaction of these ions in solution to form nuclei of crystallization from solution phase and (c) crystal growth of this phase (Fig. 1.4). The recrystallization can occur in parallel with the change in the crystal size and phase transformation (12). The dissolution of a-TCP is an exothermic process, while the formation of crystals (precipitation process) from an aqueous solution without foreign ions is endothermic (15). Despite the large number of possible formulations, the CPCs developed up to now have only two different end products: precipitated hydroxyapatite (HA) or brushite (DCPD) (16). All the above are characteristically illustrated in Fig. 1.3.
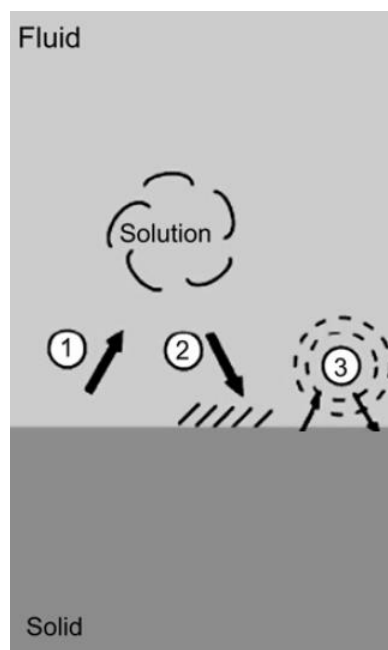
Fig. 1.4 : A representative illustration of the phenomena that take place at the interface between a calcium phosphate cement and the surrounding environment, during hydrolysis: (1) dissolution of biocement; (2) precipitation from solution; (3) ion exchange and structural rearrangement and growth of the crystals (**17**).

Calcium phosphate cements also exhibit variable stoichiometry, functionality, and dissolution properties (10) which, combined with their intrinsic porosity, enable the potential to be used as drug delivery systems. Currently 3 ways could achieve this goal: (a) as individual molecules dissolved in the liquid within the pores, (b) adsorbed or chemically bound to the crystals surface or (c) in a solid form, as drug crystals or aggregates (Fig. 1.5)
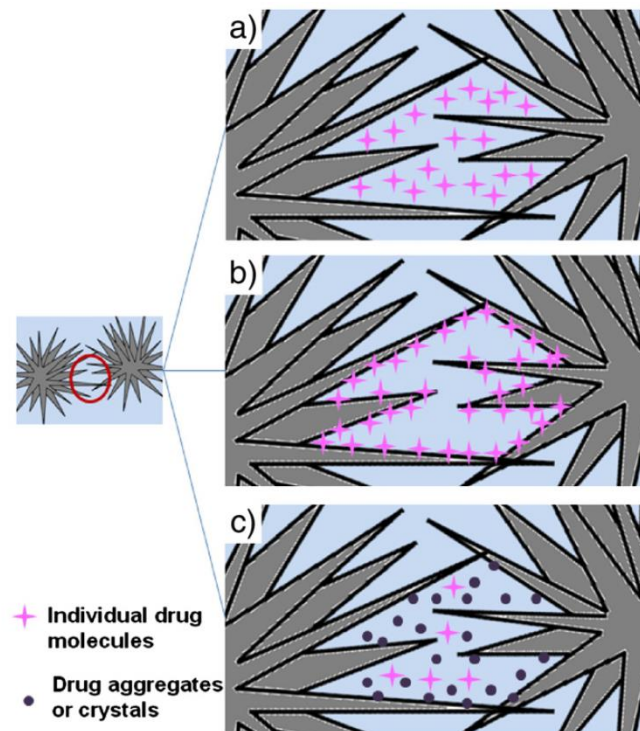
Fig. 1.5 : Schematic representation of the different ways a drug can be loaded in a CPC matrix **(16)**.

Despite CPCs' numerous advantages, a number of limitations have to be addressed in order to satisfy the clinical requirements. Apart from bad injectability (18), (19) and weak cohesion of CPC pastes (20), they also exhibit low mechanical properties (6), thus their use is limited to low-load bearing applications (6), (21). Several published works have focused on dealing with the aforementioned challenges by adding various additives either to the powder or to the liquid of CPCs (22), (23), (24), (25), (26). In these works, an improvement in handling properties, desired porosity or bioactivity was achieved, but a decrease in the mechanical strength was also reported. Moreover, the category of self-setting CPCs, like α-TCP, present a unique feature: their mechanical properties can be improved when are immersed in a liquid of similar

composition of human body fluids because of occurred microstructural changes (6), (27), hence are considered as promising CPCs to overcome current mechanical challenges.

As it is demonstrated in Chapter 2, most of the studies that deal with CPCs measure their strength by conducting only compression tests. However compression strength cannot be the only criterion in order to assess the mechanical performance of a CPC, since they are meant to be subjected to complex stress fields developed in human bones (28). Moreover, porosity is not always evaluated despite the fact that is the most detrimental factor to CPC mechanical properties (6). Last but not least, little information exist in the literature about the induced strains during self-setting cements' fabrication. This parameter should be considered of significant importance since any strain fields developed during this period can affect the way CPCs fail under loading.

1.2. Thesis goals and structure

In this work a thorough characterization of a calcium phosphate bone cement is presented, that was fabricated from the mixture of pure α-TCP powder and Na_2HPO_4 aqueous solution and subsequently hardened through hydrolysis reaction. The conducted characterization covers five main sections:

- Detection of any occurred microstructural changes during hardening period
- Evaluation of the exhibited porosity
- Material's mechanical testing
- Material's absorbability in wet environment
- The developed strains throughout characteristic phases of the material's fabrication.

Moreover 2 simulation models are implemented and presented, in order to describe the diffusion phenomenon in wet environments and the induced hygroscopic strains, respectively. Additionally a case study was also simulated in which the use of the studied bone cement in a real life application is investigated. Based on the frame that is set from the abovementioned sections and implemented models, the structure of this thesis was accordingly formed and is described in the following paragraph, while a characteristic illustration can be found in Fig. 1.6.

Initially, in Chapter 2 are reported several studies that set the context within the research falls, as far it concerns calcium phosphate bone cements. Afterwards, in Chapter 3, are presented the used materials and the implemented steps that were followed in order to fabricate the needed bone cement specimens. Moreover, the design and dimensions of the moulds that were used are also presented.

Chapter 4 is composed of 4 main sub-chapters that concern an equal number of the aforementioned main sections of the conducted characterization. Specifically, in the first one are reported the results from scanning electron microscopy (SEM) and X-ray diffractometry (XRD) in samples that were hardened at different levels, in order to investigate the development of any crystal structures during hardening period. The second sub-section concerns the evaluation of the material's porosity with 3 different methods: micro computed tomography (μ-CT), microscopy investigation and confocal microscopy. In the third one the material properties of the examined biocement are determined from the conduction of compressive and diametral compressive testing, as well as from low-load indentations. Furthermore, based on the presented results a failure model is proposed. In the last sub-chapter of Chapter 4 the material's absorbability is investigated by conducting immersion experiments in bone cement samples, in liquid environments.

Passing to Chapter 5, the experimental results of the developed strains are presented and discussed, obtained throughout three characteristic stages during material's fabrication: (i) solidification (ii) hardening and (iii) re-immersion. The experimental data were obtained with the use of non-destructive, optic method (Fiber Bragg Grating-FBG sensor), whose working principle is described in details at the start of the chapter. Furthermore, the strain results are also coupled with the experimental results presented in Chapter 4, in order to investigate any correlation between them.

Chapter 6 includes the implemented models and their results for the diffusion phenomenon, during re-immersion, and the corresponding developed hygroscopic strains. Also the input data and the obtained results are presented and discussed for a simulated case study in which the examined bone cement was used as a fixation mean of a stem implant, in a Total Hip Replacement (THR) case. Finally, in Chapter 7 are summarized the exported conclusions from

this work and several ideas are proposed as future work, in order to further deepen the characterization of such materials.
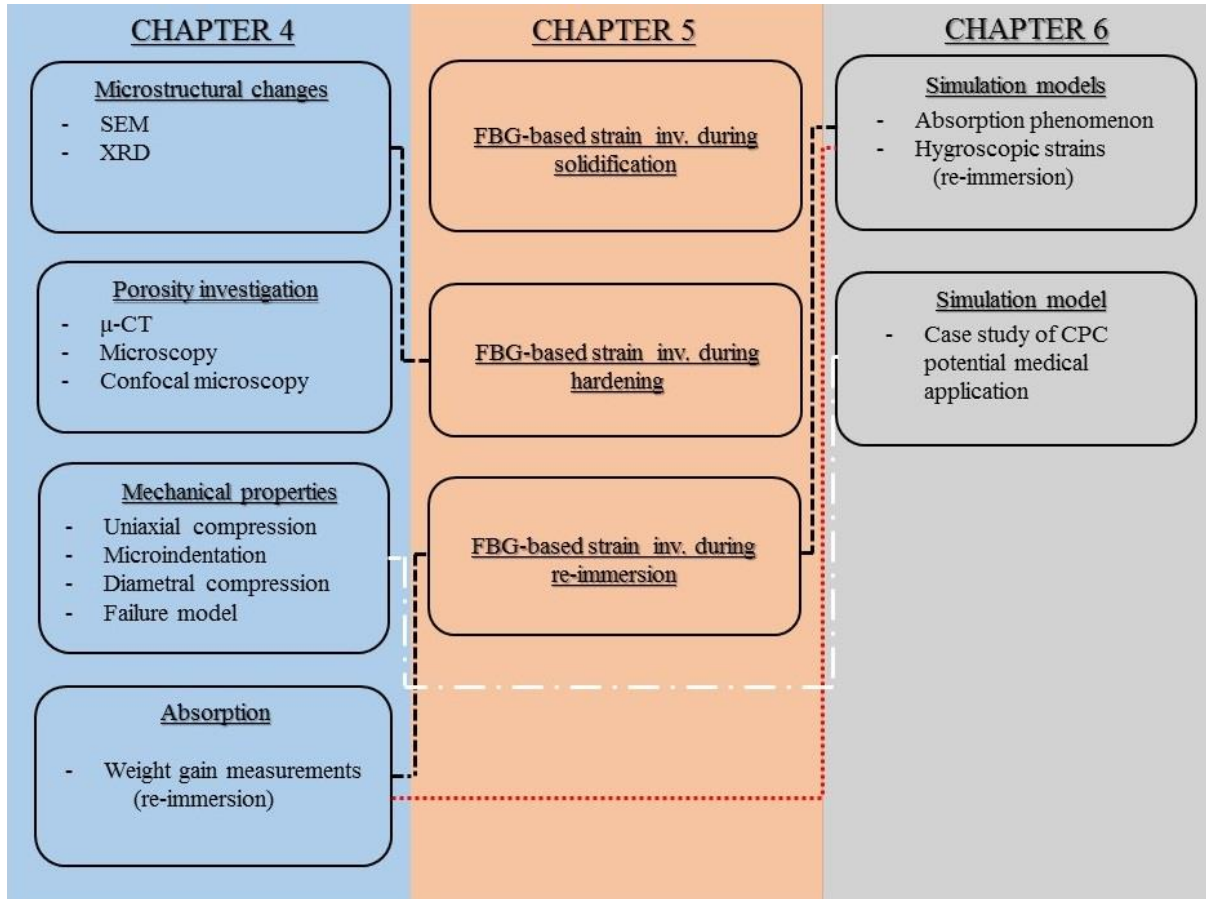
Fig. 1.6 : Illustrative summary of the conducted work.

Chapter 2

State of the art

There are various works on calcium phosphate ceramics that mainly investigate their use in medical applications, their physico-chemical properties after their setting stage or the use of various additives in order to achieve the desired clinical requirements a CPC should exhibit. The following scientific articles were chosen to set the context in which the research, concerning calcium phosphate cements, falls within:

Charriere et al. (29) conducted compression, tension and torsion tests on brushite and precipitated hydroxyapatite cement in moist condition. From the obtained results elastic and strength properties were obtained for each type of fabricated cement. A 10% difference between the compressive and tensile Young's moduli, allowed to fit the full set of strength data to an isotropic Tsai-Wu criterion while elastic data were fitted to a conewise linear elastic. Moreover, from a comparison between the measured mechanical properties and the human cancellous bone it was confirmed the potential use of brushite as a bone filling material and hydroxyapatite cement as a structural biomaterial.

S. Padilla et al. (30) investigated the ability to achieve appropriate mechanical properties for a potential use of prepared hydroxyapatite (HA), by the gel casting method, as bone implant. The mechanical properties of the material was evaluated, while the influence of the solid content on the rheological behaviour of the slurries and, in turn, on the mechanical properties, was investigated. The raw and calcined HA were characterised through a number of experiments: XRD, FTIR, X-ray fluorescence and elemental analysis. The mechanical properties of the green bodies were higher than obtained by other methods, while the final pieces were comparable to those obtained by other techniques. The results suggested that slurries with a solid content that surpasses a threshold value (for which limited contraction occurs) must be used as well as that

the rheological properties of the slurries influence the mechanical properties of the final material.

Combes and Rey (31) published a review paper on amorphous calcium phosphates (ACPs) that provide an update on several aspects of these compounds, since there is lack of indisputable proof of the occurrence of an ACP phase in mineralised tissues of vertebrates. The various synthesis routes of ACPs with different compositions are reported as well as the techniques used to characterise this phase. The study focuses on various physico-chemical properties of ACPs and especially the reactivity in aqueous media, which have been exploited to prepare bioactive bone substitutes for medical or/and dental applications.

The work conducted from Zhang et al. (32) concerned apatite cements, fabricated through α-TCP (α-tricalcium phosphate) hydrolysis, that were subjected in various tests in order to assess their mechanical properties (Young's modulus, fracture toughness and compressive strength), as a function of various parameters (particle size, liquid-to-powder ratio, amount and morphology of porosity, including macropores). The aim of this study was to find a better compromise between strength and biological behaviour.

Montufar et al. (33) used gelatine as an additive to an α-TCP/hydroxyapatite calcium phosphate powder to obtain injectable self-setting hydroxyapatite/ gelatine composite foams for bone regeneration. From the obtained solid foams, it was demonstrated that gelatine addition improved the cohesion and injectability of the cement paste. After setting of the slurry, the foamed paste transformed into a calcium deficient hydroxyapatite. Finally, final porosity, pore interconnectivity and pore size were modulated by modifying the gelatine content in the liquid substance that was mixed with calcium phosphate powder to obtain the investigated solid foams.

Yang et al. (34) reported the preparation and study of a novel calcium sulfate/magnesium phosphate cement (CSMPC) composite. The physical properties were studied, including the phases, the microstructures, the setting properties and the compressive strengths. Also the bio-performances of the CSMPCs were evaluated using in vitro simulated body fluid (SBF) method and cell culture, as well as the dependence of the physical and chemical properties of the studied material on its composition and microstructure.

Le Huec et al. (35) focus on the influence of porosity on the mechanical resistance of hydroxyapatite ceramics under compressive stress and Amrah-Bouali et al. (36) present a research on surface modifications of hydroxy(l)apatite ceramics in various aqueous media of different compositions (distilled water, saline solution, cell culture media, saturated HA solution).

Bohner et al. (37) as well as Habib et al. (38) investigated the ease of CPC pastes' injection, which is strongly dependent on the injection system (e.g. type of syringe, needle size, injection speed). Moreover, it appears that injectability and ease of injection differ between them, since the latter does not consider the quality of the extruded paste in which phase separation may occur and could lead in deviations of the actual composition of the extruded paste from the initial one (39), (37). Consequently, it becomes unclear whether various properties, including mechanical ones, of the extruded cement are still clinically acceptable (40).

Also, numerous scientific articles exist that deal with the chemistry and kinetics of CPCs setting, although the chemistry of the setting reaction in these cement systems does not significantly differ and can be understood by investigating the solubility behavior of the compounds involved (41), (42), (43). Moreover, several researchers deal with the use of additives in powder of liquid compound (44), (45), (46) or composite fibers (47), (48), (49), (50) in order to enhance various properties of the resulting CPC.

Chapter 3

Sample preparation

3.1 Materials used and sample handling

In order to fabricate the specimens needed for this work, amounts of α-TCP powder were produced and provided by Prof. Bouropoulos (Department of Material Science, University of Patras), that required a specialized procedure. Specifically, ball milling was performed in equimolar quantities of calcium carbonate and calcium pyrophosphate for a certain period. Then the resulted mixture was placed in alumina crucible and absolute ethanol was also added to prepare a suspension. The suspension was homogenized using magnetic stirring, dried, then placed in a furnace at high temperature for several hours and eventually rapidly quenched on a metallic surface. The resulted material was finally crushed in the ballmill for certain time periods in order to obtain the powder in its final form. The granules' size (diameter) of the powder varied between 0.5 and 5 μm (51), with a mean particle size diameter of 4.5 μm. More details about powder fabrication can be found in (14).
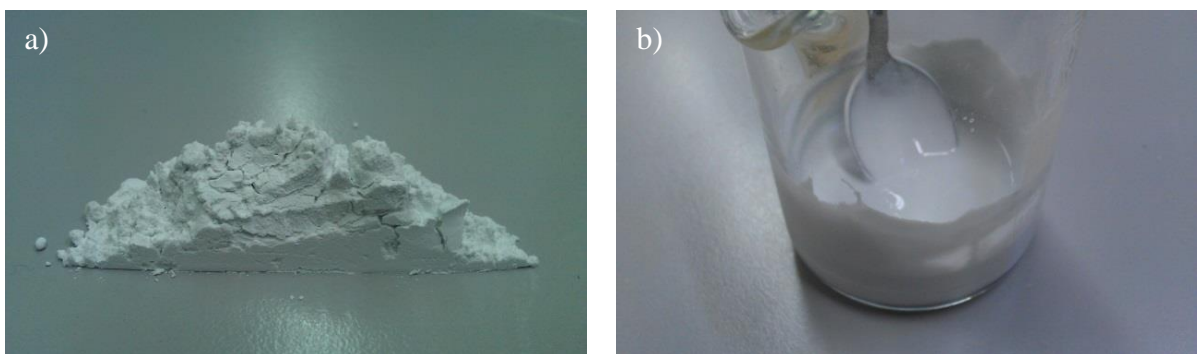
Fig. 3.1 : (a) α-TCP powder (b) the resulted slurry from the mixture of the α-TCP powder with the aqua solution.
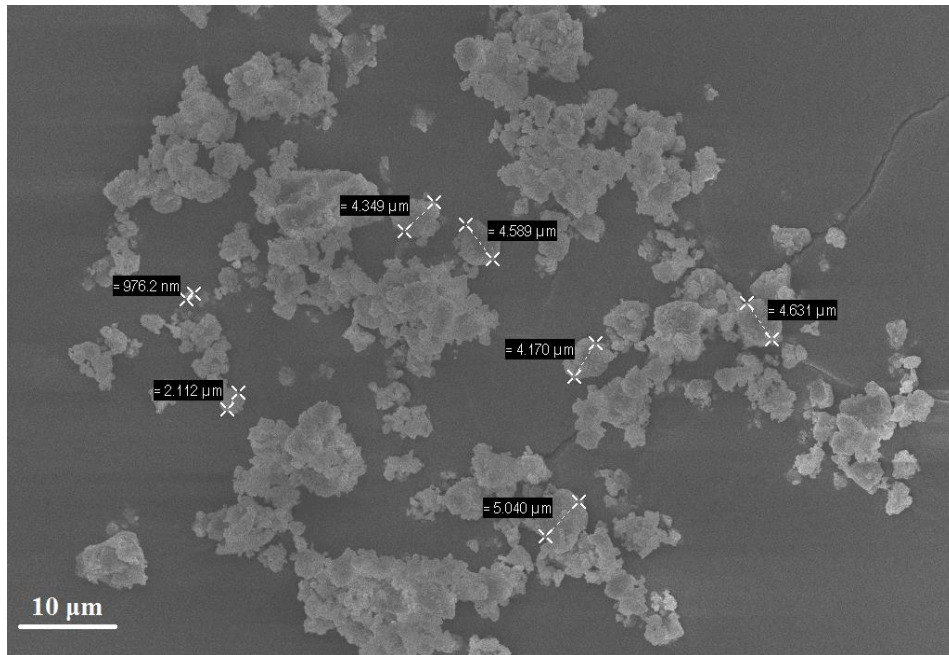
Fig. 3.2 : Characteristic SEM image of granules collected from the α-TCP powder, used for the needs of this work **(51)**.

The fabrication of the samples was implemented through three different steps and more specifically: (I) manual mixture of the α-TCP powder and Na_2HPO_4 aqueous solution , in a ratio of 1 ml : ~2.06 gr, that resulted in a malleable paste (Fig. 3.1b) and casted with a spatula in the moulds (II) the casted paste was let to solidify for at least 4 days, in room temperature (~23 ^{0}C) and (III) the solidified samples were recovered and placed in the Ringer solution that acted as a hardening liquid, as reported in the literature (27), for at least 15 days. The hardening process took place also in a temperature of ~23 ^{0}C except for a number of the specimens intended for low-load indentation (see 4.3.2.2), that were hardened in human body temperature (~37 ^{0}C). Since several specimens were tested in dry state, upon the completion of hardening stage they were dried in an oven at a temperature of ~50 ^{0}C for at least two hours.

3.2 Moulds design and samples geometry

The resulted paste from the mixture was casted into three different type moulds in order the specimens to have the desired geometry. The first one (Type I), made of ABS, was built by a closed chamber FDM Stratasys Elite 3D Printer and consisted of 2 parts that could be

assembled and create a cylindrical cavity of 12 mm in diameter and 40 mm in length (Fig. 3.3a,b). Three samples recovered from this mould, labeled as A, B, D, and subsequently were hardened in the Ringer solution.
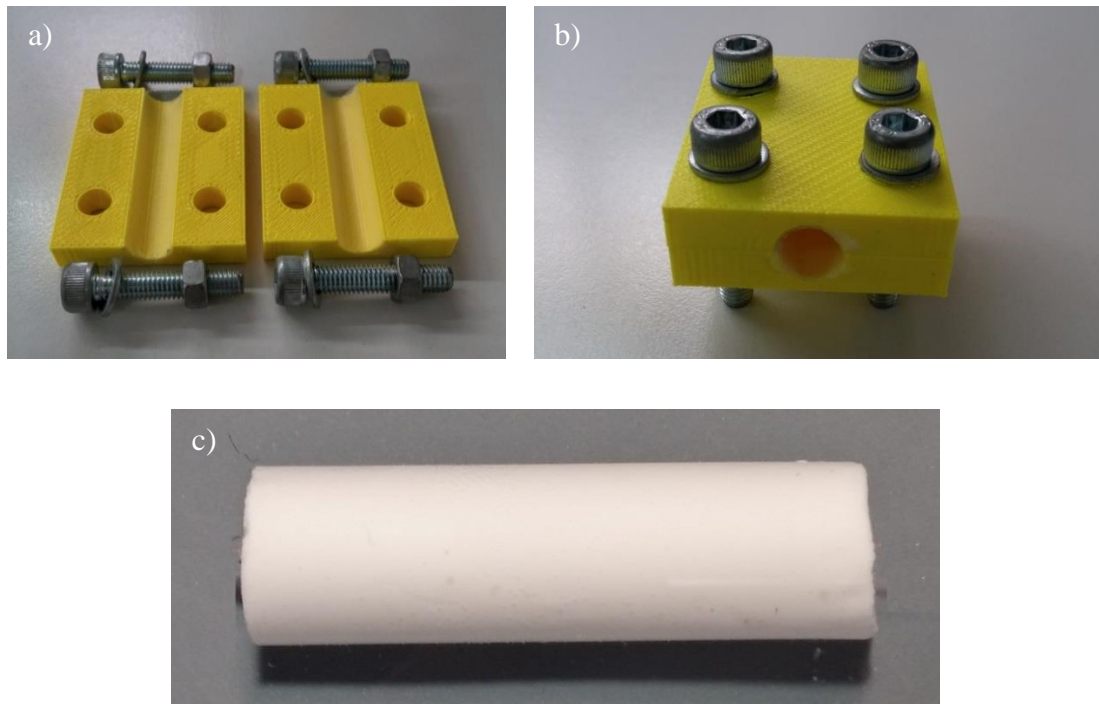
Fig. 3.3: 3-D printed mould for cylindrical specimen: (a) components (b) assembled mould (c) the resulting sample.

Afterwards in sample A a cut was performed, perpendicular to its longitudinal symmetry axis (Fig. 3.4) using a diamond wire saw. As a result two new cylindrical specimens, of 12 mm in diameter and 20 mm in length, were created and denoted as AW1 and AW2. Specimen AW1 was used for μ-CT imaging while AW2 was further cut in 4 pieces, using the same technique, in order to create 4 cross sections that were thoroughly investigated with a microscope. Sample B was also cut perpendicular to its longitudinal symmetry axis with the same way and 8 cylinders, of 12 mm in diameter and 5 mm in length, were created (labeled as BW1-BW8) and intended for indirect compression test. The remaining specimen D was used for the investigation of induced strains with a camera as well as for weight gain measurements, when the specimen was immersed in liquid media.

Fig. 3.4 : Performed cut in a cylindrical CPC specimen using diamond wire saw.

The second mould (Type IIa) was made of silicon, having 10 rectangular cavities of 6x6x12 mm^3 (width x length x height) as it is seen in Fig. 3.5b, in order to recover the specimens easily without damaging their shape. It was fabricated by casting silicon in a "negative" mould (Fig. 3.5a) with attached aluminum blocks that created the desired cavities. Alternatively small 3-D printed moulds (Type IIb) having the same cavity dimensions were used in some cases for the fabrication of same dimensions block CPC samples (Fig. 3.6). Overall, forty two (42) block samples came up from these moulds and were used for XRD, SEM investigation, confocal microscopy and compression tests, after the hardening period was completed.
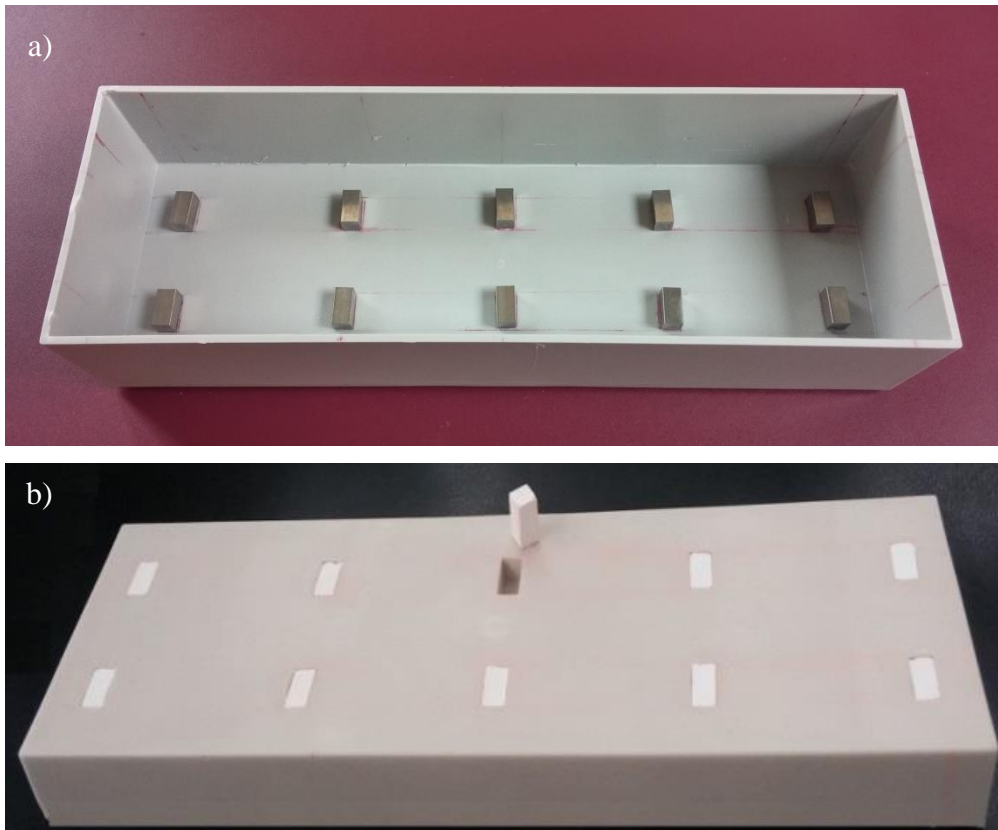
Fig. 3.5: (a) "Negative" mould in which silicon was casted (b) the resulted silicon mould (Type IIa).

The third mould (Type III) was made of aluminum with a cylindrical cavity of 12 mm in diameter and 40 mm in length. It was designed and manufactured in LMAF laboratory of EPFL, in order to allow the proper placement of a 0.125 mm in diameter optical sensor, through the specimens' longitudinal axis. Moreover calibrated weights, placed at the bottom end of the fiber, ensured the proper alignment of the fiber (Fig. 3.7d). Those specimens were intended for strain investigation induced during sample's solidification, hardening and drying. In Table 3.1 a summarized presentation of the prepared specimens and their intended use can be found.
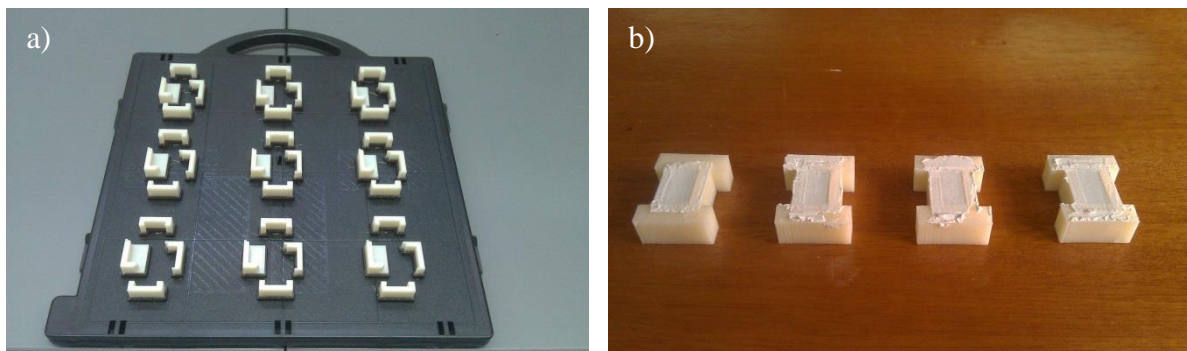
Fig. 3.6 : 3-D printed mould (Type IIb) for block specimens: (a) de-assembled (b) assembled and filled with CPC paste.
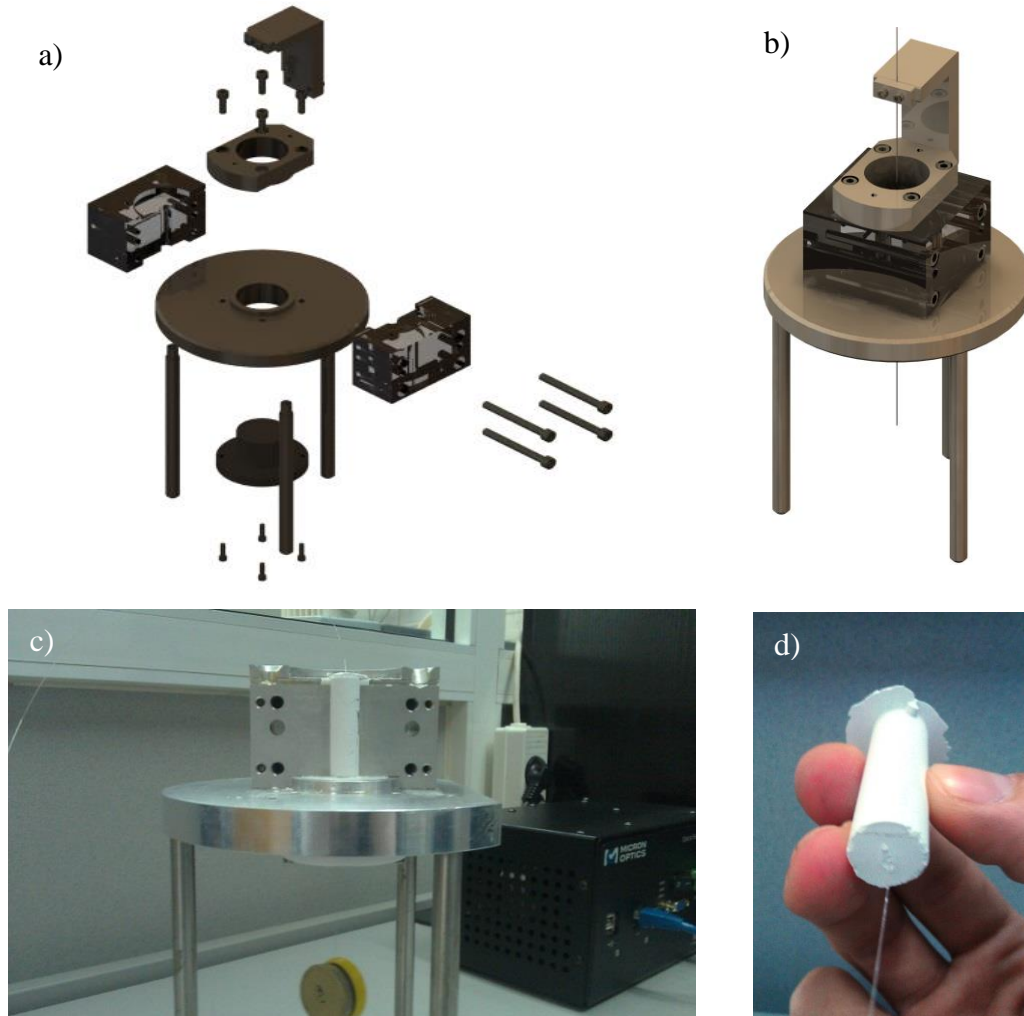
Fig. 3.7 : Custom made mould (Type III) for cylindrical specimens with embedded FBG sensor: (a) its components (b) assembled (c) solidified CPC sample before recovery (d) the resulting sample. *(Fig. (a) and (b) retrieved from* **(52)***).*

Mould Type	Number, Geometry & Dimensions of samples	Sample Label	Specimen Processing	Number, Geometry & Dimensions of new created samples	Label of new samples	Intended use
I	3, Cylindrical, 12 / 40 mm (**D**iameter/**L**ength)	A	Cut with diamond wire saw	2, Cylindrical, 12 / 20 mm (**D/L**)	AW1	μ-CT
					AW2	Microscopy
		B	Cut with diamond wire saw	8, Disk, 12 / 5 mm (**D/L**)	BW1-BW8	Indirect Compr. Test
		D	No	-	-	Camera strain inv.
						Weight gain meas.
II (a or b)	42, Prismatic, 6x6x12 mm (WxLxH)	E1− E8	No	-	-	SEM
		X1− X10	No	-	-	XRD
		C1 − C9	No	-	-	Compr. Test
		L1− L15	No	-	-	Low-load indentation
		F1,F2	No	-	-	Confocal Microscopy
III	8, Cylindrical+FBG 12 / 40 mm (**D**iameter/**L**ength)	S1 − S6, M1,M2	No	-	-	FBG strain inv.

Table 3.1 : Summary of the fabricated specimens and their intended use.

Chapter 4

Material characterization

4.1 Microstructural changes

4.1.1   Scanning Electron Microscopy

During hardening stage and at different time periods, 8 prismatic specimens (E1‑E8) were recovered in couples, each time, from the isotonic solution and dried in order to stop any reaction in progress. These time periods concerned the first hours of immersion and specifically 48, 72, 96, 144, 192 and 240 hours (i.e. 2, 3, 4, 6, 8, and 10 days) since hardening period commenced. Based on previous studies, it has been demonstrated (27), (53) that the microstructural changes take place and evolve within 12-15 days of immersion in aqueous media. After the recovery process was completed those prismatic specimens were used for SEM investigation. Morphological characterization was performed on gold coated specimens using a Field Emission Scanning Electron Microscope (FE-SEM, LEO SUPRA 35VP).

In Fig. 4.1 some representative SEM images from the examined samples at different reaction times are presented. By comparing them one concludes that microstructural changes took place when the bone cement was immersed into the hardening liquid. Initially, after 48 hours of immersion commencement a-TCP particles exhibit a sandy texture and on these particles an early creation of a layer composed of small crystal structures can be distinguished as seen in (4a). After 72 hours (3 days) and 96 hours (4 days) of immersion significantly larger crystal structures were observed having either leaf-like or needle-like shapes, leading to the conclusion that growth of these structures was taking place (4b and 4c). In the next presented image (4d), referring to 144 hours (6 days) of immersion, an entanglement of the previously observed structures having uniform size is observed. However, there are also areas on cement's surface where the size of the crystal structures varies. This finding is also verified by (4.3a) where a higher resolution was applied, suggesting that the growth of these structures was still in

progress. After 192 hours (8 days) of immersion, as seen in (4.1e), the created layer on a-TCP particles has now become an entangled network of crystals and it is enough dense so that particles' initial geometry has altered. Finally, after 240 hours (10 days) of immersion, in (4.1f), the crystals' network appears to be more compact, clearly supported from the image of a higher magnification presented in (4.2b). It is seen that a thick layer of a complex crystals network has been created occupying the existing voids between α-TCP particles.
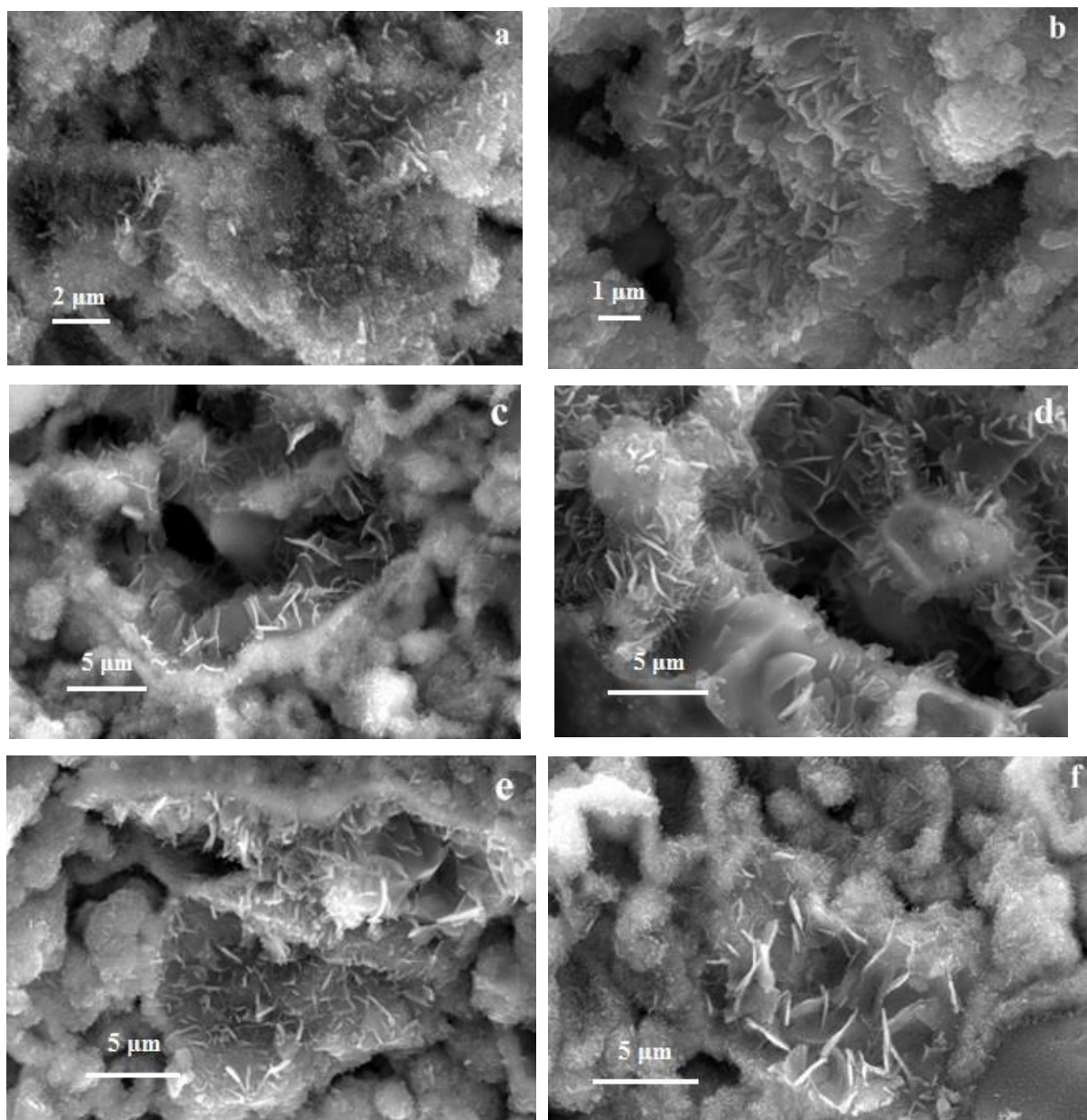
Fig. 4.1 : SEM images in various reaction times: (a) 48 h (b) 72 h (c) 96 h (d) 144 h (e) 192 h and (f) 240 h.

The findings demonstrated that microstructural changes took place during the followed hardening stage, as it is also supported by several studies (27), (53), (54) regarding self-setting biocements. Moreover, the different geometry of the observed crystal structures is strongly related with the size of α-TCP powder, as it is presented in Fig. 4.2. After 6 days (144 hours) of immersion, a clear entanglement of these structures was observed for the first time from the SEM images. In the following days, the entanglement became more complex as it is depicted from the captured images at 8 and 10 days (192 and 240 hours) of immersion.

Ginebra et al. (27) and Komlev et al. (53) have conducted SEM investigations in self-setting calcium phosphate bone cements during hardening stage. They have reported that the observed microstructural changes were completed after 12-15 days of samples' immersion into the hardening liquid instead of ~25 days obtained in the present study. However, Zhang et al. (6) reports that various parameters such as smaller particle size, higher setting temperature and low liquid-to-powder ratio can affect kinetics and as a consequence CPCs' setting time. Considering that the aforementioned parameters were not the same with the ones of the present study, such differences in the time period where microstructural changes take place are expectable.

Fig. 4.2 : Correlation between size of calcium phosphate powder's granules and the developed crystal structures, during hardening stage **(16)**.
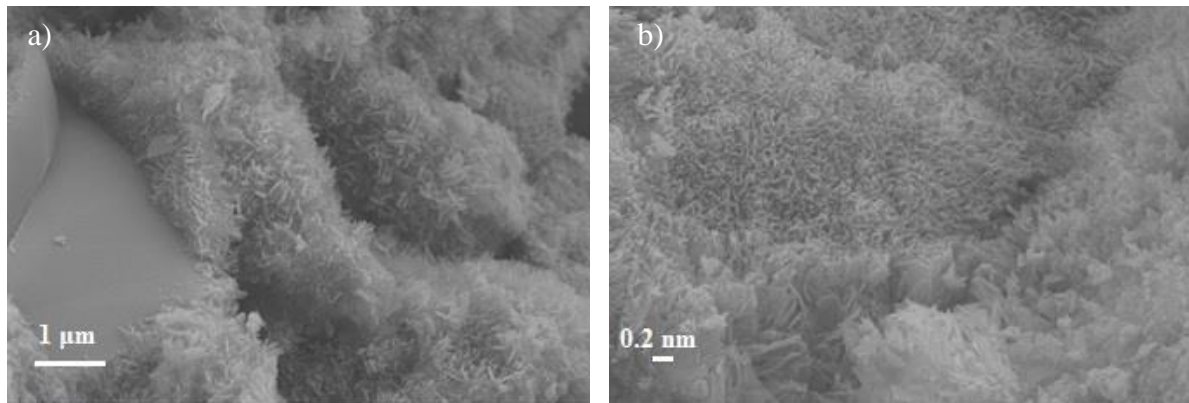
Fig. 4.3 : SEM images using higher magnification at selected reaction times: (a) at 144 h and (b) at 240 h.

4.1.2 X-Ray Diffractometry

Ten prismatic specimens (X1-X10) recovered at 72, 120, 168, 264 and 432 hours (i.e. 3, 5, 7 ,11, and 18 days) after their immersion in the hardening liquid, were dried and then used for XRD characterization of the material. All solids were characterized using a Siemens/Bruker D5000 X-ray diffraction with CuKα radiation.

Fig. 4.4 depicts the XRD patterns of the: (i) standard powders (α-TCP, β-TCP, hydroxyapatite), (ii) α-TCP powder that was used in this study, as well as the examined cement specimens at different hardening times. The specimens, for clarity reasons, are labeled in the figure with a number and a letter, where the number corresponds to the time period, in days, the specimen stayed in the hardening liquid while the letters designate a sequential numbering. The XRD diffractogram of the powder used in this work besides α-TCP peaks exhibits the characteristic peaks of β-TCP. The presence of β-TCP polymorph is common when quenching is not fast enough or when the reactant components contain impurities which promote the nucleation of β-TCP (27). In the case of the cement specimen remained in hardening liquid for 24 hours, it is clear that new peaks are emerged in the 2θ:30-35o indicating the formation of apatite. Moreover, in the following days the peaks of apatite correspond to (211), (112) and (300) reflections are overlapped, due to peak broadening. This is probably due to the presence of carbonate ions in the apatite structure or to the formation of calcium deficient hydroxyapatite because of a-TCP conversion (55), which is directly related with the crystal structure growth. In addition, the fact that a-TCP was detected for the last time after 7 days, since hardening

period started, suggests that a-TCP conversion was nearly completed around this time period. Finally, residual α-TCP was detected for the last time in the specimens recovered after 7 days of immersion in the hardening liquid.
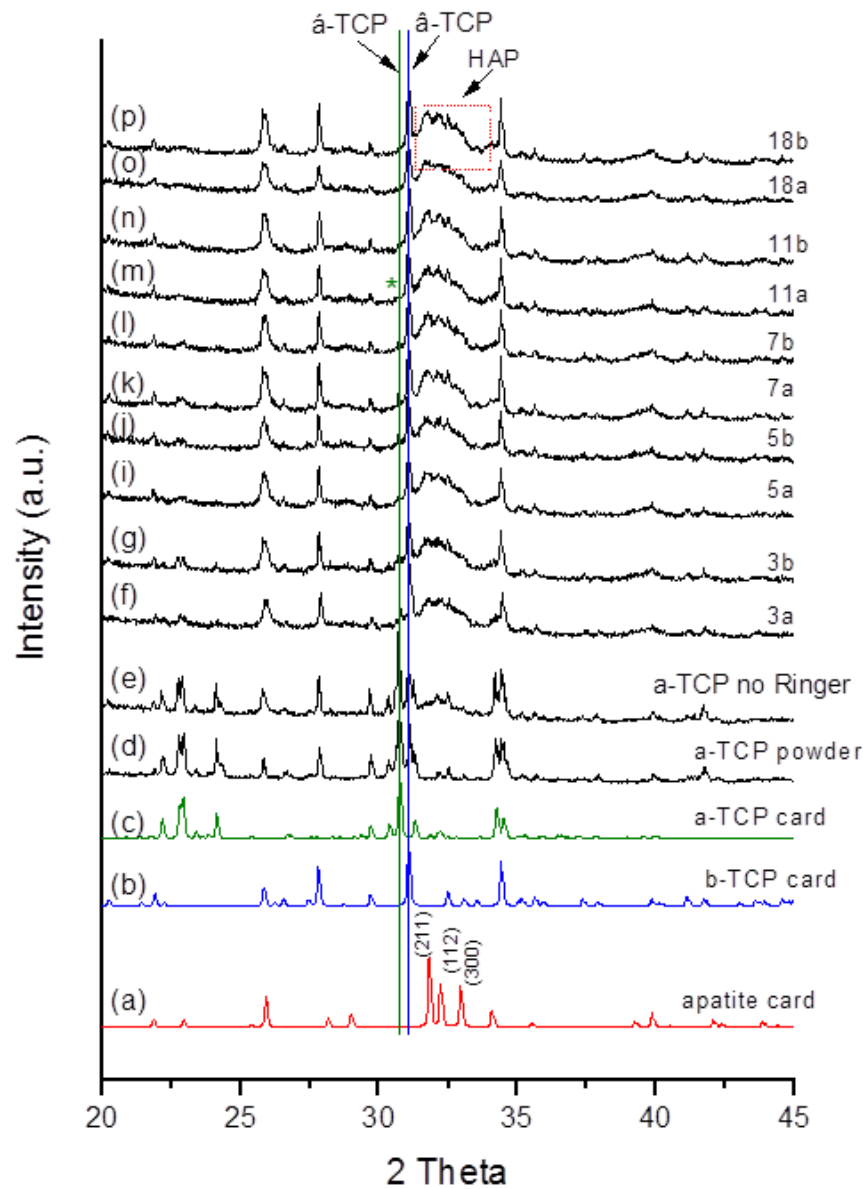
Fig. 4.4 : XRD patterns of a) JCPDS card for hydroxyapatite 9-0432, b) JCPDS card for β-TCP, c) JCPDS card for α-TCP, d) starting powder e) cement before immersion in Ringer solution f) cement after immersion in Ringer solution for 3,5,7,11 and 18 days. Asterisk denotes the disappearance of α-TCP peak after 7 days.

4.2 Porosity investigation

4.2.1   Micro computed tomography imaging

Micro computed tomography or "micro-CT" is a three dimensional (3-D) imaging using X-rays. Specifically a micro-focus X-ray source penetrates the examined object and a planar x-ray detector collects the projection images. Based on hundreds of angular views acquired (Fig. 4.5), a 3-D reconstruction of a stack of virtual cross section slices through the object is achieved with the use of a software program.
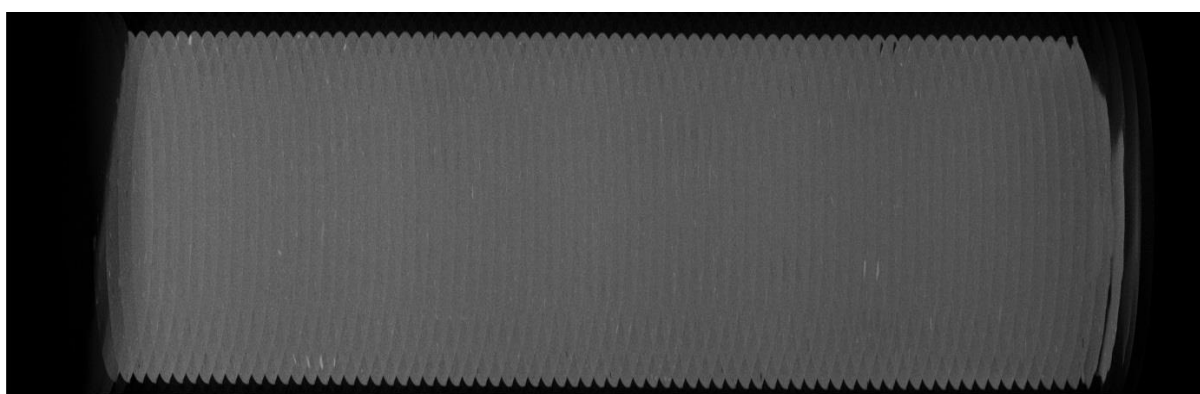
Fig. 4.5 : Sequential angular captured pictures, from μ-CT imaging, of the examined cylindrical bone cement sample.

One of the two cylindrical specimens, denoted as AW1, was dried and used for micro computed tomography (μ-CT) imaging (Bruker microCT, Kontich, Belgium). In this work, the highest resolution was applied which corresponds to 9 μm voxel size. The resulting images were software processed (CTAN image analysis) to construct the 3-D image of the specimen. The calculation of the material's porosity is based on voxel's brightness: low brightness voxels represent low density areas (pores) while high brightness voxels represent bulk material (56), (57). Then porosity is given as the fraction of the low brightness voxels over the total amount of them. However, the main challenge of this technique is the definition of a threshold in brightness value that distinguishes the two different voxel "categories". In this work, the resulted μ-CT images were mainly employed to check the extent of pores due to the trapped air and the uniformity of the material microstructure.
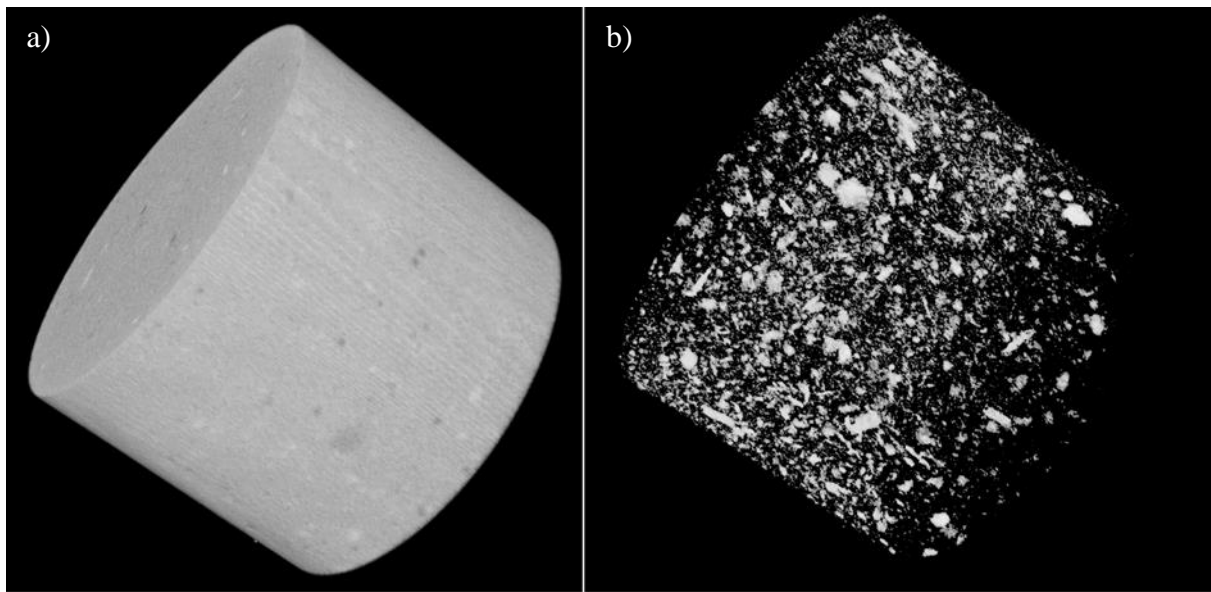
Fig. 4.6: Micro-tomography image of the CPC specimens showing (a) the macro-porosity and (b) the crystals' agglomeration developed during the hardening stage.

A characteristic view of the final 3-D reconstructed image is presented in Fig. 4.6a. Several grey and black spots are observed in the specimen. Those spots are small voids created from trapped air during casting or the materials' macro porosity that exceeded the size of several tens of microns. However the examined CPC has pores which their size is below that limit as one can observe in the Fig. 4.1c and d that were recorded from SEM investigation of the examined material. Thus, not all macro pores can be adequately depicted from the micro-CT imaging since their size is on the edge or lower than 9 μm that corresponds to lowest applicable voxel size. Consequently, a value for the threshold brightness can't be defined with certainty. However if the threshold brightness value is increased several regions of higher brightness voxels, compared to the rest of the specimen, are revealed (Fig. 4.6b). These regions are dispersed in a uniformly way and the high brightness suggests that the density of these regions is higher than the rest of the material. In the literature is well established that during hydrolysis of α-TCP (hardening period), crystal structures are developed and entangled that enhance the bone cement's mechanical response (12), (27), (54). Thus, the distribution of the crystals has a significant influence in the mechanical behavior of the material. The 3D images obtained from the micro-CT investigation can provide qualitative information on the crystals distribution.

4.2.2 Microscope investigation

Specimen AW2 was dried and the 4 created cross sections from the performed cut (see Section 3.2) were polished with a 4000 paper grid before observed with an optical microscope in order to investigate the porosity. Characteristic images were captured and afterwards processed with software, in order to estimate the porosity based on the occupied surface of the pores.
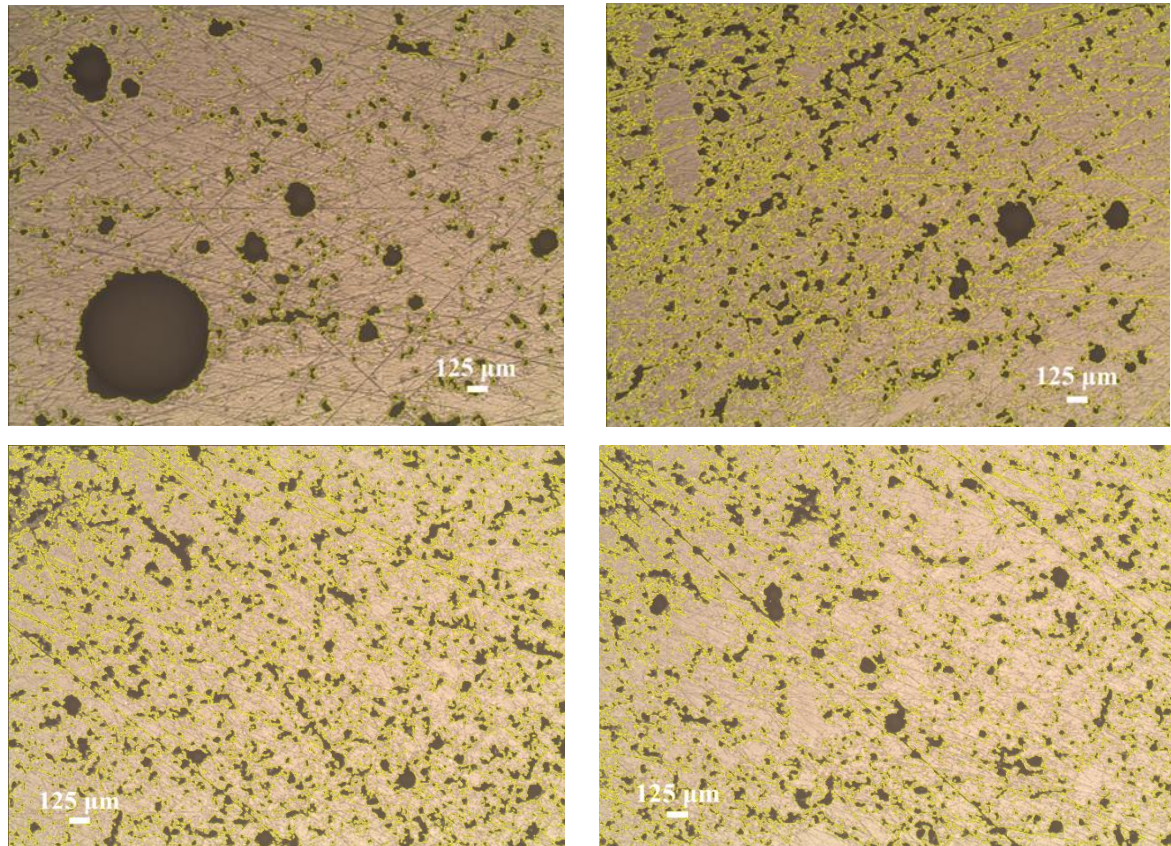
Fig. 4.7 : Characteristic images from the microscopy investigation.

In Fig. 4.7 four captured images during the bone cement's investigation with the optical microscope, are presented. The yellow lines are the perimeters of the areas that software detected as pores, based on the brightness of the pixels. In general, pores of different size exist: some of them are of several hundreds of microns while the rest vary in the order of tens of microns. However, the majority of them are between <10 μm and 50μm, hence the pores of this size mostly determine the porosity of the examined CPC. The pores which their size was above ~50-70 μm are voids that were created due to the entrapment of air during casting, like the ones detected in μ-CT imaging. This is supported by the fact that their shape is close to a

circular geometry and not irregular, like the rest of the pores. The porosity was calculated as a fraction of the pixels surrounded by the yellow lines over the total amount of pixels the image has. In the four presented pictures it varies between 27% and 32.1%.

This evaluation comes in accordance with the calculated porosity that was based on experimental data, presented in Section 4.4. The specimen used to acquire these results was cylindrical, having 12 mm in diameter and 40 mm in length (i.e., same dimensions with the specimen used for microscope investigation), with a weight at the dry state equal to ~6 gr. The specimen was immersed in the Ringer solution and weighted after saturation. Saturation was considered when additional weight gain is negligible for relatively long time (for this study, saturation was achieved in ~5 minutes and the experiment was interrupted after 13 days of immersion). The results indicated a mass increase of ~25 % (or ~1.5 gr). Considering a density of ~1.007 gr/cm3 for Ringer solution (58), which is a typical value provided by the material suppliers, the volume of the absorbed liquid was found. By dividing it over the volume of the specimen specimen's porosity was obtained: ~33 % which is very close to the porosity evaluated using the optical microscope images. It is worth noticing that since saturation of the specimen in the Ringer solution is achieved very fast, diffusion, as relatively slow process, is considered negligible. The data also suggest that the specimen possess a network of open porosity.

4.2.3   Confocal microscopy

Confocal microscopy is an optical imaging technique that gives the ability for enhanced optical resolution and contrast of a micrograph by adding a spatial pinhole positioned at the confocal plane of the lens to eliminate out-of-focus light. Through this technique a 3-D reconstruction of 3 the acquired images can be succeeded, by collecting sets of images at different depths within a thick object (59). The specimens intended to be investigated with the confocal microscopy technique (F1 and F2) were cut perpendicular to their longindutinal axis with a razor, mounted on the cross head of a testing machine and as a result a raw planar surface was created in each specimen (Fig. 4.8).
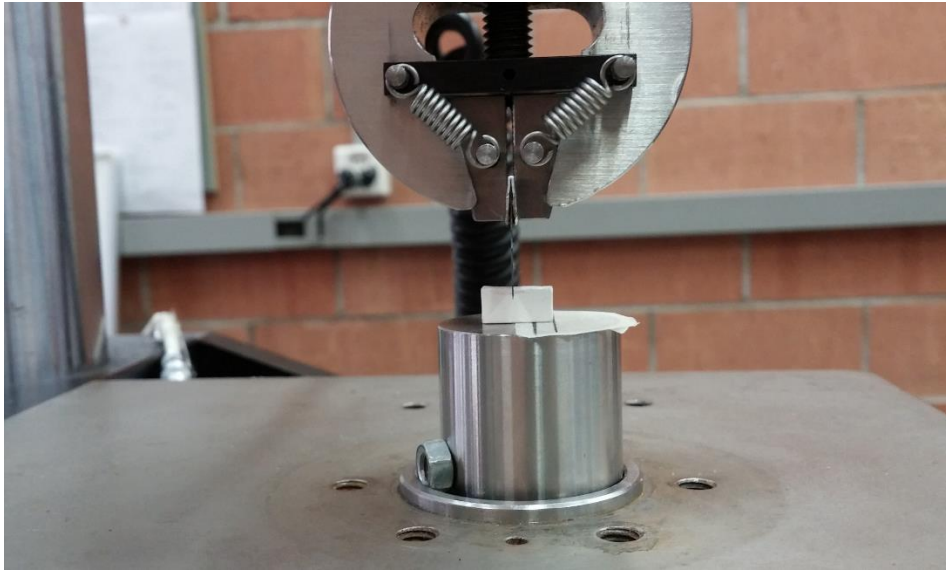
Fig. 4.8 : Performed cut in a specimen intended for confocal microscopy investigation.

Subsequently, the created raw surfaces were divided in 25 equal areas of 0.8x0.8 mm size each, that were investigated and images were recorded. Finally the obtained images were stitched in order to reconstruct a 3-D image which is the final result. For each specimen, the images were acquired in a different way: in the case of specimen F1 the scanning of the surface was cross sectional (Fig. 4.9a) while in F2 specimen was from the top to the bottom (Fig. 4.9b). Although some pores can be observed, it is obvious that the maximum applied resolution was not high enough in order to depict the majority of the pores. Consequently, this technique is not efficient in investigating the porosity of the studied CPC.
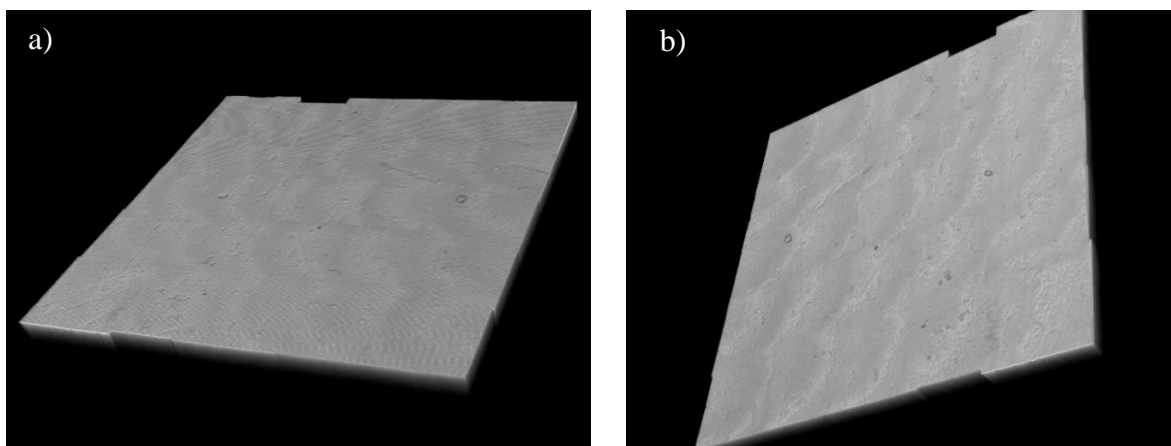
Fig. 4.9 : 3-D reconstruction of the surfaces investigated with confocal microscopy technique: (a) cross sectional scanning (b) top-to-bottom scanning.

4.3 Mechanical properties

4.3.1 Compressive testing

The compressive testing was carried out in specimens that were hardened in the hardening liquid (Ringer solution) for several days, in order to obtain the final mechanical strength. Specifically nine block specimens, denoted as C1 – C9, were recovered in preselected time periods: after 9 and 14 days after the hardening process started, in groups of three, that were tested in wet state. Additionally three fully hardened specimens (14 days of hardening) were also tested in dry state. Each specimen was loaded up until its catastrophic failure (Fig. 4.10b). The compressive strength tests were performed using a MTS Insight testing machine equipped with a 10 kN load cell and metallic platens while the cross head was displacement controlled with a rate of 1.5 mm/min. It is noted that the followed testing method is also reported in several published studies that conducted compressive testing in CPCs (14), (60).
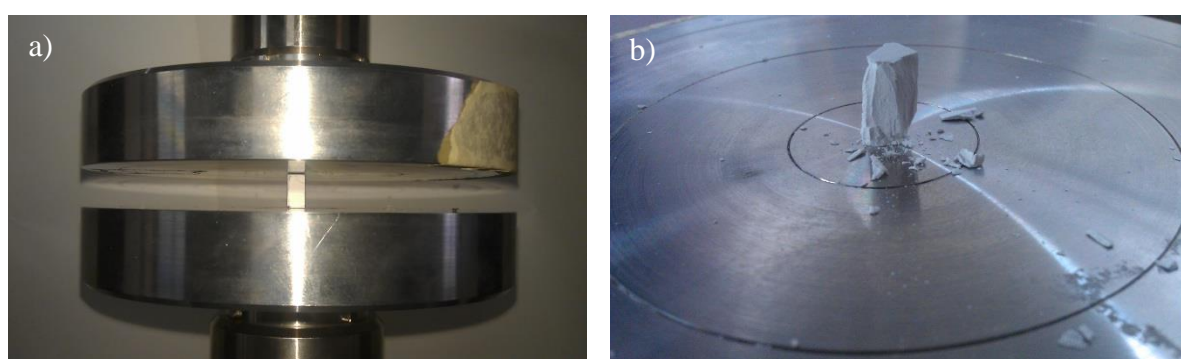
Fig. 4.10 : A block specimen a) during compressive testing b) after its failure.

The obtained stress–strain curves, presented in Fig. 4.11 and Fig. 4.12 are plotted based on the apparent stress (MPa) and strain (%) values determined by dividing the load value by the initial cross-sectional area of each test specimen and the deformation values by the initial specimen height, respectively. Additionally, the elastic modulus was measured as the tangent at the longer linear part of the stress–strain curves. The average elastic constants (Young's modulus and strength) in compression are shown in Table 2.
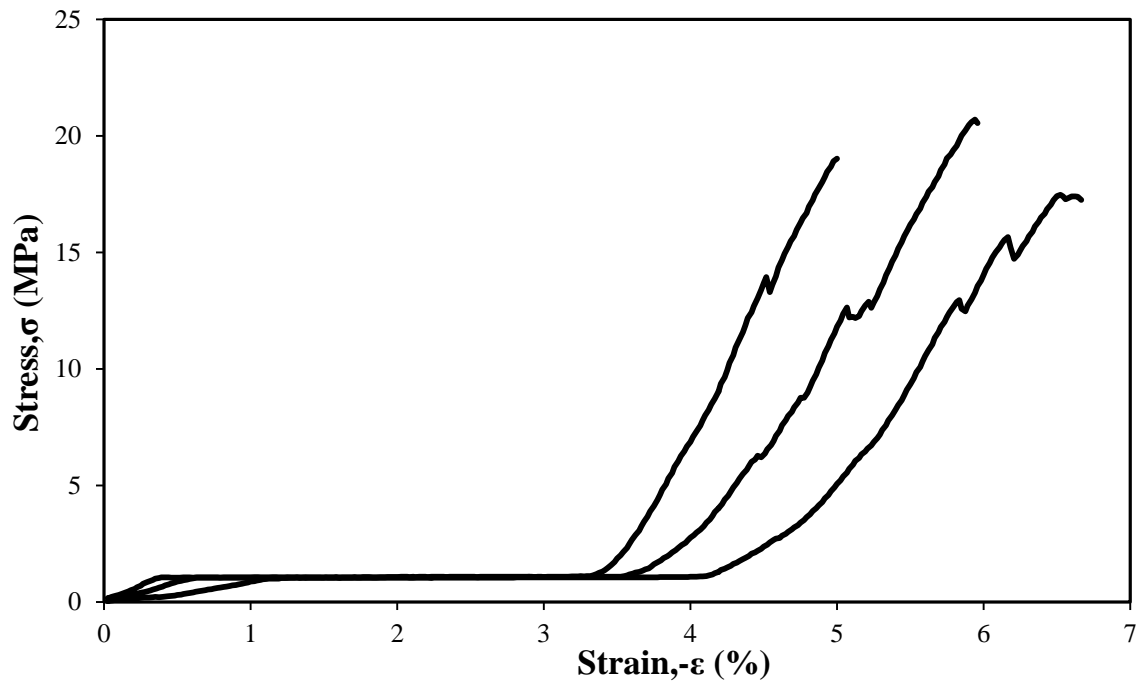
Fig. 4.11 : Stress–strain curves of compressively tested specimens, previously immersed during hardening stage in Ringer solution for 9 days.
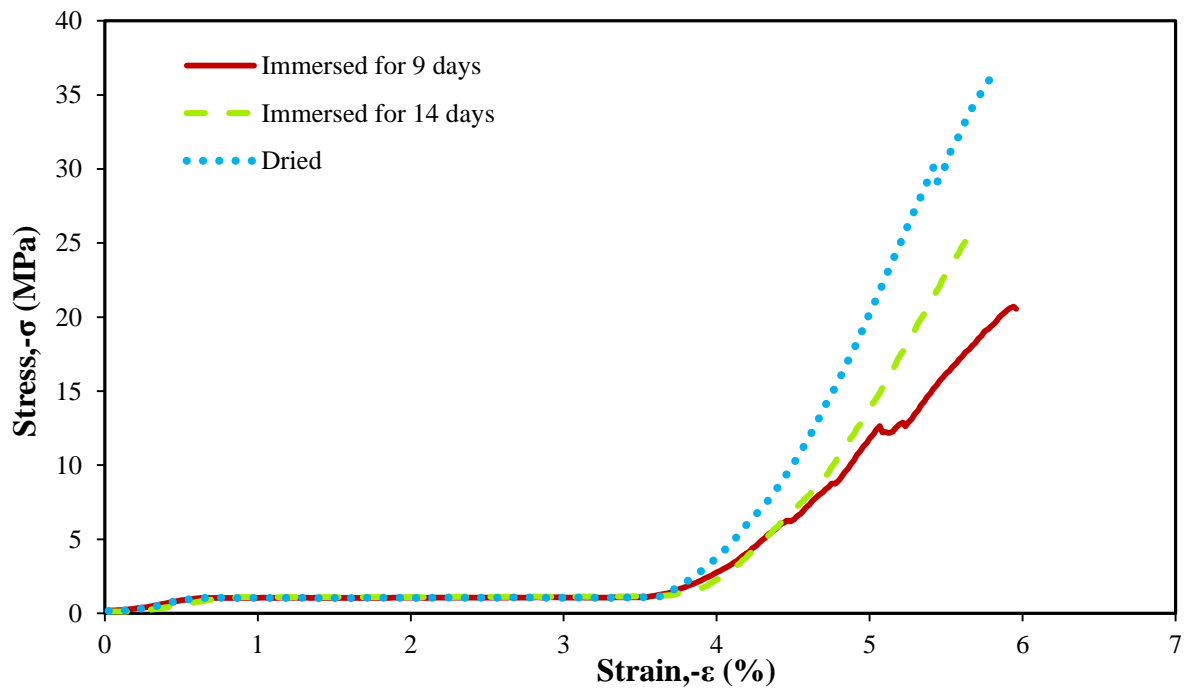
Fig. 4.12 : Characteristic stress–strain curves of specimens treated at different conditions

Examining the stress–strain graphs the following similar trends (patterns) of compressive behavior are observed. First, on the onset of the applied deformation a small linear behavior is observed. Then, a long stress plateau is observed followed by a second, longer, elastic deformation region up to failure. The stress plateau behavior may be explained by the fact that the tested cement samples are highly porous. As the specimens were put under compressive loading the macropores can't carry any additional load as the pores are crushing. At the end of this densification event the compressive load bearing ability of the material increases leading to a larger elastic deformation region at which the modulus was calculated. The majority of the samples exhibited the appearance of small load slips when compressed beyond the stress plateau. These slips are related to the generation of cracks oriented parallel to the direction of loading. The same failure modes have been also observed in (61) during the mechanical characterization of dense calcium phosphate bioceramics, where it is reported that one explanation to the fact that the observed fracture of samples is not caused by maximum shear stresses could be due to the presence of friction between the sample and the compression platens. Comparing the results in Table 4.1 is observed that Young Modulus was increased considerably when the tested samples were immersed in the liquid media for several days.

In a study conducted by Andriotis et al. (14) a similar calcium phosphate cement is investigated and among other results Young Modulus and compressive strength in unhardened state is reported: 410 MPa and 19.1 MPa respectively. Although care should be taken in comparing the absolute values of this study with the one reported in Table 4.1, since in the published work the applied ratio powder/liquid is lower, it is safe to conclude that both compressive strength and Young modulus are considerably increased after hardening period. Moreover, an increasing value of strength as a function of the time of hydration is also reported in (62). The improvement of the exhibited mechanical properties is purely attributed in the growth of the crystal structures, during hardening period, demonstrated in section 4.1. When dried, all test specimens exhibited higher properties compared to the unhardened specimens.

Stage	Mechanical strength (MPa)	Young modulus (GPa)
Immersed for 9 days	18.9	1.2

Immersed for 14 days	21.8	1.7
Dried	31.5	2.0

Table 4.1: Average compressive mechanical properties of the studied bone cement.

4.3.2 Low-load indentation

Instrumented indentation is a common method for characterizing the mechanical properties of a material. This technique is capable of testing small volumes of material at low loads and small displacements and allows for simple sample preparation compared to traditional tension or compression tests (63). In this work, a spherical indenter was chosen in order to test a relatively large zone, as compared to a sharp one, and reduce the influence of material's porosity (64). The set-up as well as the resulting print ($\sim$ 952 μm in diameter) in the indented surface are presented in Fig. 4.13a and b.
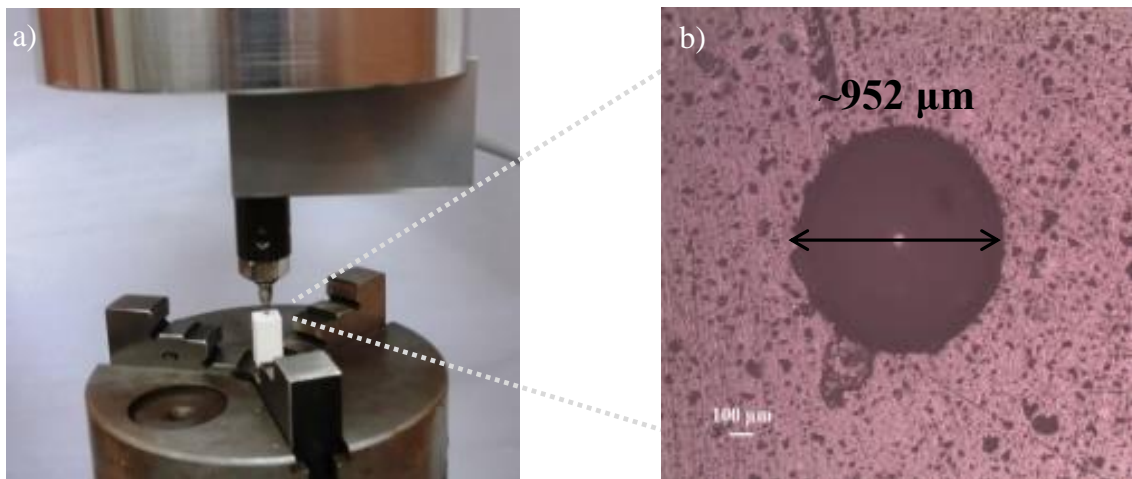
Fig. 4.13 : (a) Indentation of a block specimen (b) indentor's print on the sample's surface.

The indentation test was performed in an Instron 5848 Microtester test machine equipped with 100 N load cell, at room temperature. The crosshead was displacement controlled with a rate of 0.24 mm/min, during loading part, and 0.06 mm/min for the unloading part. The total crosshead displacement was set to 0.4 mm, towards specimens' surface. Before the indentation was performed, specimens' surfaces were polished in order to ensure parallelism. For the results analysis, Oliver and Pharr's method (65) was used in order to calculate penetration depth

($h_{contact}$), contact area (A) and reduced Young's modulus (E_r), as a function of the indenter penetration:

$$h_{contact} = h - e\frac{P}{S} \quad (4.1)$$

$$A = 2\pi R h_{contact} - \pi(h_{contact})^2 \quad (4.2)$$

$$E_r = \frac{S\sqrt{\pi}}{2\beta\sqrt{A(h_{contact})}} \quad (4.3)$$

Where (P) is the applied load and (S) is the stiffness ($\frac{dP}{dh}$), in the unloading part, that was calculated by linear fitting of the first 25% of the unloading curve. The value of e depends on the indenter's geometry: for a spherical indentor e=0.75 (66). Then the specimen's Young's modulus (E_s) was obtained using Eq. (4.6):

$$\frac{1}{E_r} = \frac{1-v_s^2}{E_s} + \frac{1-v_i^2}{E_i} \quad (4.4)$$

For the given bone cement and indentor, the following values were used respectively: v_s=0.28 (67), E_i=220 GPa, v_i=0.3. The measurements were repeated at least 3 or 4 times in every indented surface in order to determine the error in the presented results and the maximum error in the Young modulus was found to be ±25 MPa. However for the unhardened specimen as well as the specimens hardened for 2 and 4 days, only one measurement was successful due to the fact that the material was too brittle for the applied load. The latter is attributed in low crystal development since the hydrolysis of the bone cement was still in early stages.

4.3.2.1 Room temperature

Seven prismatic specimens (L1– L7) were recovered at 48, 96, 144, 192 and 240 hours (i.e. 2, 4, 6, 8, 10, 12 and 14 days) after the immersion in the hardening liquid commenced, under a room temperature (~25 ^{0}C) while one specimen was indented unhardened. In Fig. 4.14 the load-displacement curves from the obtained test data, are presented. As it can be observed the achieved maximum load was low in the unhardened specimen but was considerably increased during bone cement's stay in the hardening period. Based on these data, the corresponding effective Young modulus was obtained and presented in the Fig. 4.16 while the dependence of

(E_r) on the indentor's penetration depth ($h_{contact}$) is shown in the inset graph of Fig. 4.14, indicating that it was levelled off at the achieved depth in the conducted experiments.
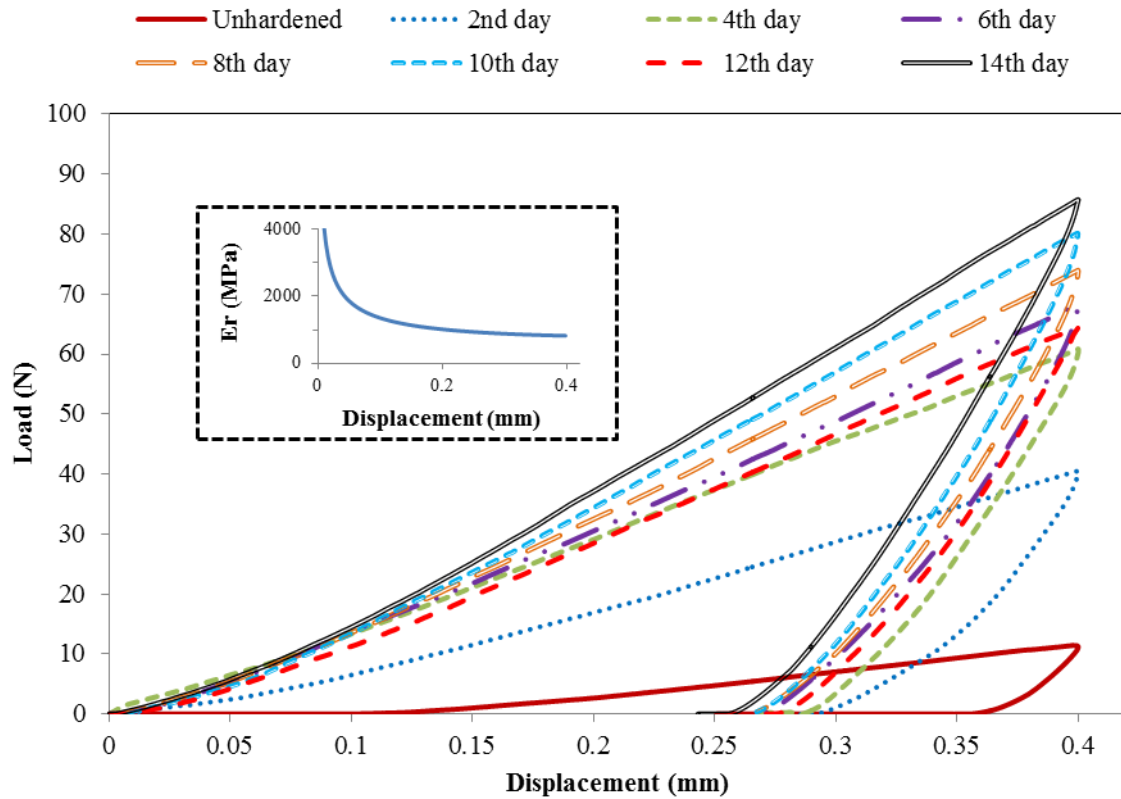
Fig. 4.14 : Load - displacement curves from indentation tests in samples hardened at 25 ^{0}C. Inset: Evolution of the reduced modulus.

It is evident that Young modulus increased at least 50%, reaching a value up to ~721 MPa, due to crystal structure's development that were observed in μ-CT imaging, SEM investigation and also reported in the literature (6), (27), (54). The measurements were repeated at least 3 or 4 times in every indented surface and the error in the Young modulus was found to vary 1.5–3.5%. However for the unhardened specimen as well as the specimens hardened for 2 and 4 days, only one measurement was successful due to the fact that the material was too brittle for the applied load. This is attributed to the limited crystal development in these specimens. As one can conclude, the obtained Young modulus of the studied material after 14 days hardening in the Ringer solution based on compression tests (4.3.1) is considerably higher. Specifically, it was found to be 1.7 GPa, instead of 721 MPa. However in compression tests, as already been reported, after the initial loading the material is becoming more and more compact due to the

fact that the pores start to crush (densification) and eventually fails when enough cracks form the fracture surface (68). Consequently, a higher compressive strength and Young modulus of the material is achieved. On the other hand, a low-load indentation with a spherical indentor causes a purely elasto-plastic response of the material (64). The above lead to the conclusion that the Young modulus, obtained from the conducted indentations, apply during the early stages of loading, until the densification phenomenon starts to occur.
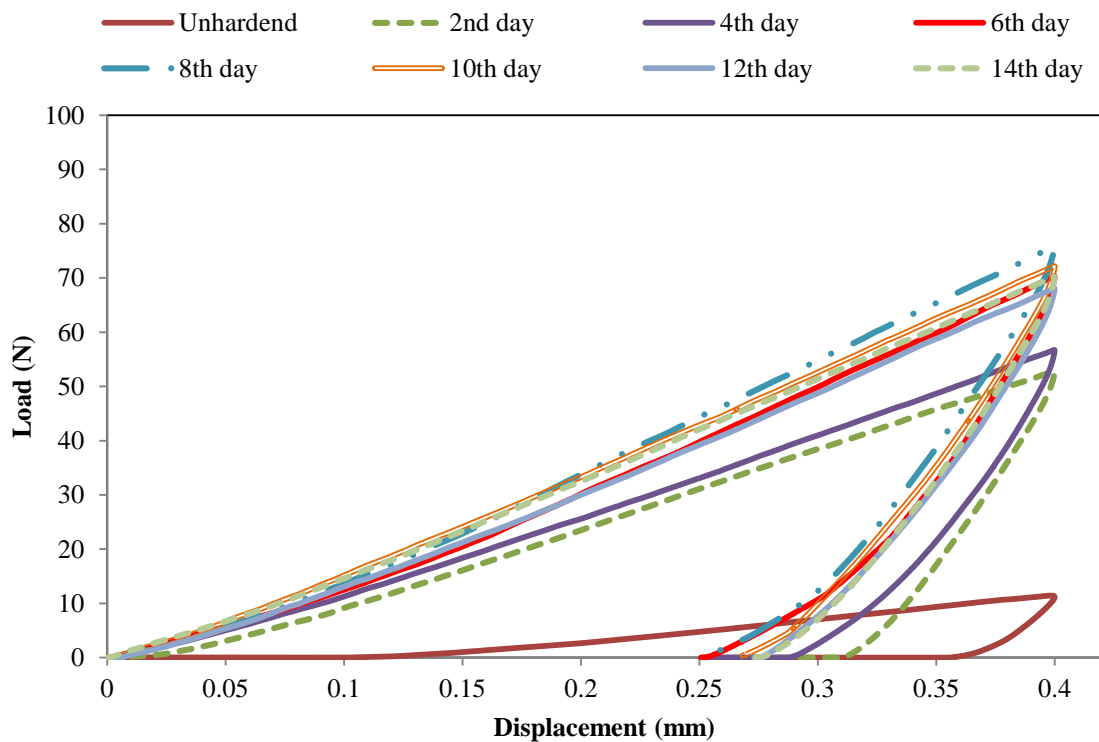
Fig. 4.15 : Load - displacement curves from indentation tests in samples hardened at 37 ^{0}C.

4.3.2.2 Body temperature

Seven more prismatic specimens (L8-L14) were subjected at low-load indentation at the same hardening periods (2, 4, 6, 8, 10, 12 and 14 days) but they were hardened under a human body temperature (~37 ^{0}C). The reason is to investigate of any changes in the final mechanical properties of the examined CPC, due to increased temperature during hardening period. The resulting load – displacement graphs are presented in Fig. 4.15 and it can be observed that the achieved load is increased in the specimens that stayed longer in the hardening liquid.

Moreover, the maximum achieved load was reached after 2 days of hardening, instead of 6 days in the specimens hardened at 25 ^{0}C.

The effective Young modulus is presented in Fig. 4.16, obtained by implementing the same method for the results analysis (Oliver and Pharr method). It can be observed that the final Young modulus is practically the same as the one obtained from the specimens hardened at room temperature. This interesting finding comes in accordance with the literature: according to Ginebra et al. (69) an apatitic calcium cement exhibits an increased rate of reaction during the first 2 days of hardening, when the temperature was increased from 25 to 37 ^{0}C. Hence, the entanglement of the precipitated CDHA crystals is exhibited earlier than in the CPCs hardened at room temperature.
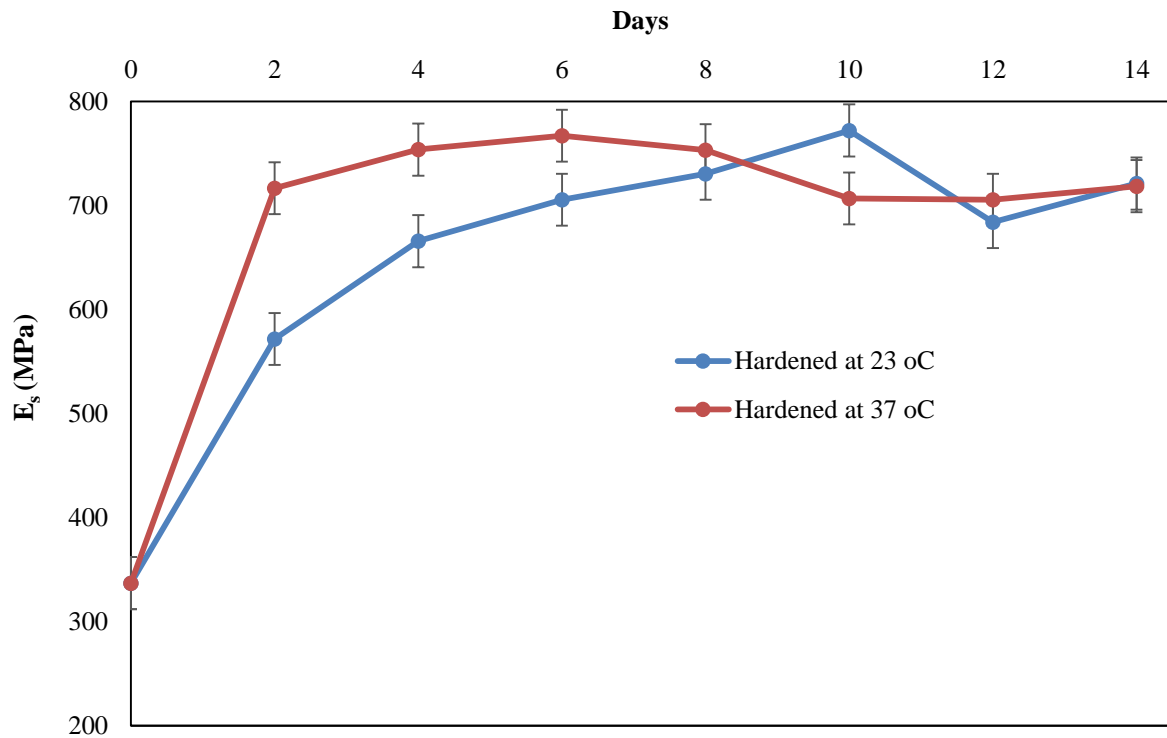
Fig. 4.16 : Evolution of Young modulus, obtained from low-load indentations, at 25 and 37 ^{0}C.

4.3.3   Diametral Compression Test

The diametral compression test allows the measurement of a brittle material's tensile strength, such in the case of ceramics or concrete. Although direct tension tests could be performed for this purpose, they are rarely used in this class of materials due to misalignment problems that are difficult to avoid and as a result tangential stress components could be induced. Hence, the measured strength of the material may be lower than the actual one (70).

The samples used in this kind of test must be disks. They are placed and aligned between the platens of the test machine and a compressive load (P) is applied on the upper and bottom area of the specimen (Fig. 4.17). Between the platens and the specimen, an inset of specific thickness is placed in order to lower the compressive stresses in these regions and avoid the failure commence from this area. During specimen's loading, tensile and compressive stresses are developed until its failure. The test is considered successful when a cleavage occurs at the center of the specimen (Fig. 4.17), on the vertical diametral plane that P loads define and the specimen breaks down in two-half cylinders. The failure occurs due to the fact that maximum tensile stress value σ_x was reached at this region and can be obtained from the following equation:

$$\sigma_x = \frac{2|-P_{max}|}{\pi DL} \tag{4.5}$$

Where P is the maximum applied compressive load, D is the diameter of the specimen and L its length/height. The developed vertical compressive stress value is 3 times higher (71), hence

$$\sigma_y = -3\sigma_x \tag{4.6}$$

In this work, the hardened cylindrical specimens, intended for diametral compression test (Fig.1c), were divided in two groups: half of them, (4), were tested in wet state while the rest of them were dried before the experiment. Their dimensions were 12 mm in diameter and 5 mm in length and verified with a caliper for the sake of accuracy. An Instron 5848 Microtester test machine was used, equipped with a 2 kN load cell and flat metallic platens while the crosshead speed was set to 0.05 mm/min. A cardboard of 0.3 mm thickness was inserted between the platens and the specimens to reduce the stress concentration and avoid damaging them. The experimental procedure in all specimens was in accordance to ASTM D3967 standard test method (72).
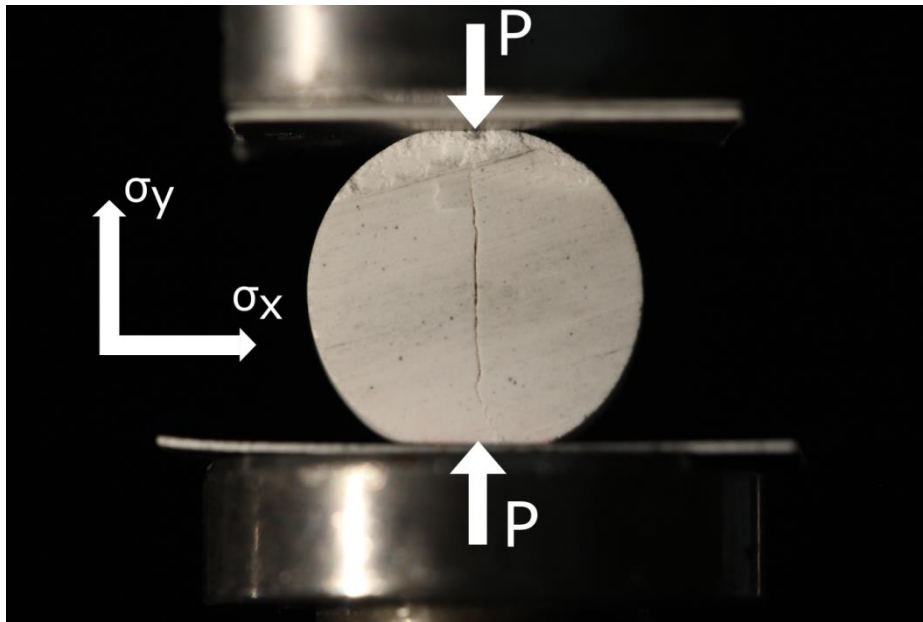
Fig. 4.17 : A disc CPC specimen subjected to indirect compressive testing. The cleavage in the center of the specimen is evident.
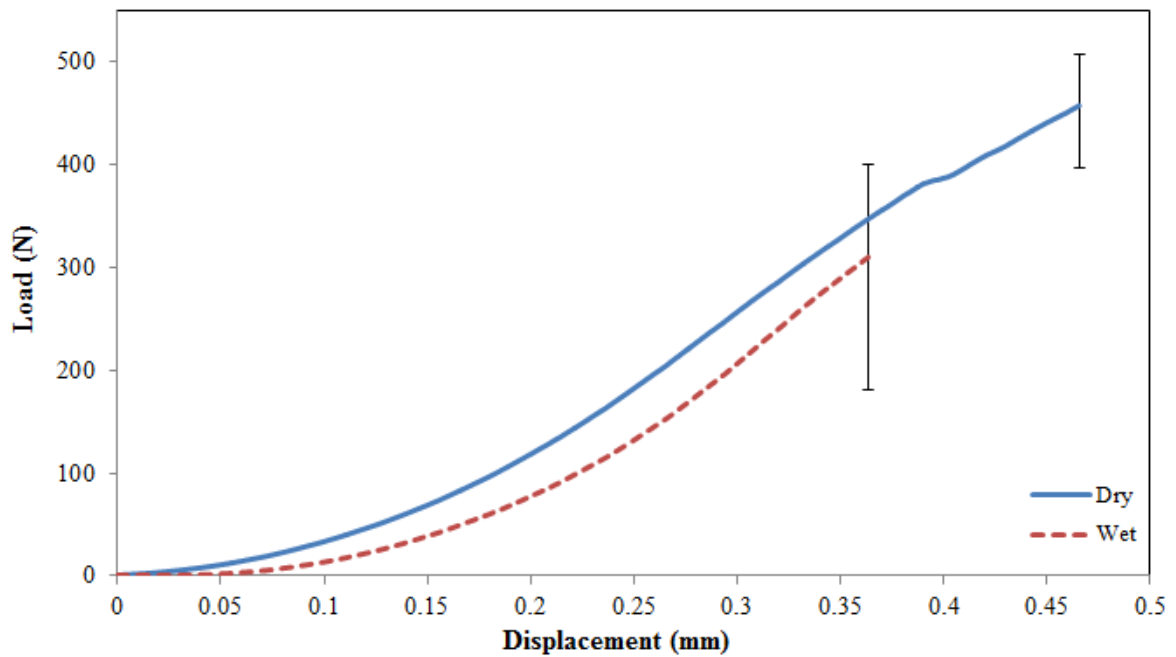
Fig. 4.18 : Representative load-displacement curves of the diametral compression tests in dry and wet CPC specimens.

Representative curves obtained from the diametral compression tests in dried and wet specimens are displayed in Fig. 4.18, with solid and dashed line respectively. One out of four

wet specimens was excluded from the experimental procedure since it presented a large void that could affect the results. The maximum achieved load in dried specimens ranged between 380 and 500 N, while for wet specimens between 180 and 400 N. The corresponding tensile and compressive stress, compiled in Table 4.2 where a good reproducibility is evident. The fact that the obtained values for the wet specimens are lower than for dried specimens is also reported in a study (68), where a similar CPC was investigated.

Test #	Dried specimens		Wet specimens	
	σ_x (MPa)	σ_y (MPa)	σ_x (MPa)	σ_y (MPa)
1	5.0	-15.2	1.9	-5.6
2	4.5	-13.6	2.2	-6.5
3	4.2	-12.7	4.5	-13.4
4	4.9	-14.9	-	-
Mean value	4.7±0.5	-14.1±1.2	2.8±1.41	-8.5±4.3

Table 4.2 : Obtained results from the indirect compression testing in dried and wet samples.

4.3.4   Failure model

The results presented from compression (4.3.1) and indirect compression tests (4.3.2) were exploited in order to propose a failure criterion for the examined bone cement. Mohr Coulomb criterion has been commonly used to characterize the failure of granular materials with different tensile and compressive strengths such as soils (73), rocks (74) and concrete (75). The biocement in this study is also a granular material and the use of a Mohr-Coulomb criterion seems adequate. The strength quantities experimentally obtained suggest that a Mohr-Coulomb failure criterion may be appropriate to predict the CPCs strength in combined loads (76). In Fig. 4.19 the obtained results from compression and diametral compression tests are presented, in Mohr diagram, for wet and dried specimens. The Mohr-Coulomb criterion is practically represented by the line that tangent those circles and is given by the following formula:

$$\tau = c - \sigma \, tan\varphi \tag{4.7}$$

Where τ is the shear stress, c is the cohesion of the material, σ is the normal stress and φ is the internal friction angle, given by the slope of the tangent line. For the given stress values, c and

φ were calculated to be ~5.0 MPa and 40.80 for the specimens in wet state while for the dried state c=~8.0 MPa and φ=39.50. Although the values of the material's cohesion (c) differ in wet and dry state, this does not apply for the internal friction angle where the can be practically considered same. No studies were found reporting similar results for this material, however the internal friction angle for a cementitious material like concrete varies from 37^0 up to 57.5^0 (75). Note that when $\varphi = 0^o$, criterion (4.9) reduces to the Tresca criterion (maximum shear stress criterion) and when $\varphi = 90^o$ to the Rankine maximum normal stress criterion also included in Fig. 4.19 to indicate the failure points assuming a brittle failure under tension loads. Although, uniaxial compression and diametral compression tests can be enough to approximate the parameters of Mohr Coulomb criterion, more realistic tests, i.e., bi-axial compression, pure shear tests, would provide more precise information to better assess the Mohr-Coulomb failure criterion for the present material and obtain cohesion (c) and internal friction angle (φ) values with higher accuracy.
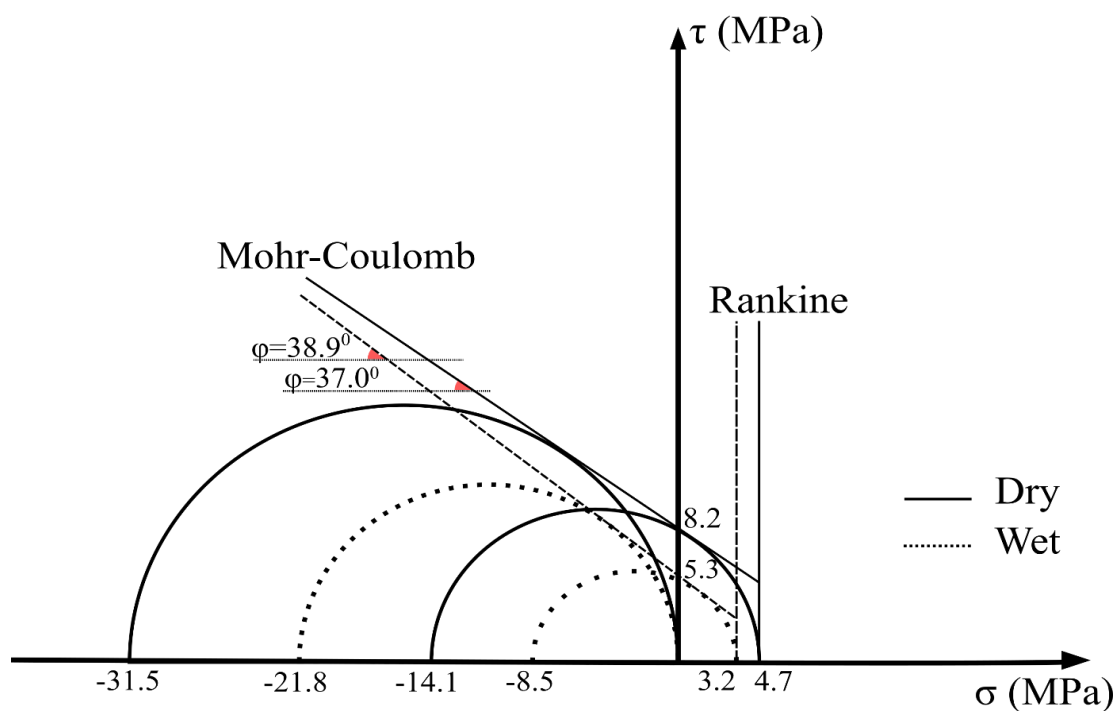
Fig. 4.19 : Mohr diagram resulted from the obtained strain values of compression and indirect compression tests.

4.4 Absorption phenomenon

The denoted D cylindrical specimen was fully dried, after the completion of hardening process, and then re-immersed in a small bath filled with Ringer solution. At certain time periods it was

recovered, its weight was measured and then re-immersed until it was fully saturated. The weight gain of the hardened samples during their exposure in liquid and humid environment was expressed as follows:

$$W = \frac{W(t) - W_{ref}}{W_{ref}} x \ 100 = \frac{\Delta W}{W_{ref}} \ (\%) \qquad (4.8)$$

where, W_{ref} is the specimen's weight at dry state and $W(t)$ its weight at time t. A digital balance of 10^{-3} gr resolution was used for measuring W_{ref} and $W(t)$. Each time the specimen was recovered from the liquid media and before it was weighed, a gentle shake was applied to it in order to remove the excessive amount of liquid on the sample's surface. In Fig. 4.20 the weight gain as a function of sample's immersion time in a liquid environment, is presented and labeled as "C". Since the experiment was conducted twice, the obtained results were numbered as (I) and (II), respectively Both times, the sample's weight gain exhibited two distinct stages: (a) a rapid liquid uptake during the first two minutes of immersion and (b) further evolution of liquid absorption with a lower rate in the following days. More measurements were taken regularly over the next days, since the experiment started, and the results are presented in Fig. 4.21 :. It can be observed that after three days of immersion the weight measurements were practically stabilized indicating that saturation levels were reached. The measurements taken after 11, 12 and 13 days of immersion, of the first experimental run, confirm the latter allegation. As it is obvious, the weight gain evolves rapidly during the first three minutes, while after 14 minutes more than 85% of the total absorbed liquid media has been gained. Hence, the time period of the first 15 minutes is the most crucial for the absorption phenomenon. In order to assure that the results were unaffected from the sample's geometry and size, the experiment was conducted again, using a small block specimen (dimensions: 6x6x12 mm). The results obtained from the block specimen are presented in Fig. 4.20 :, labeled as (B). It is evident that they are practically the same, compared with the results obtained from the cylindrical specimen, apart from the first two minutes of immersion. This difference, reaching up to ~20%, is noted during the period of rapid liquid uptake (first 2 minutes of immersion) and can be attributed to the measurements' error related with the amount of excessive liquid in the specimen's surface.
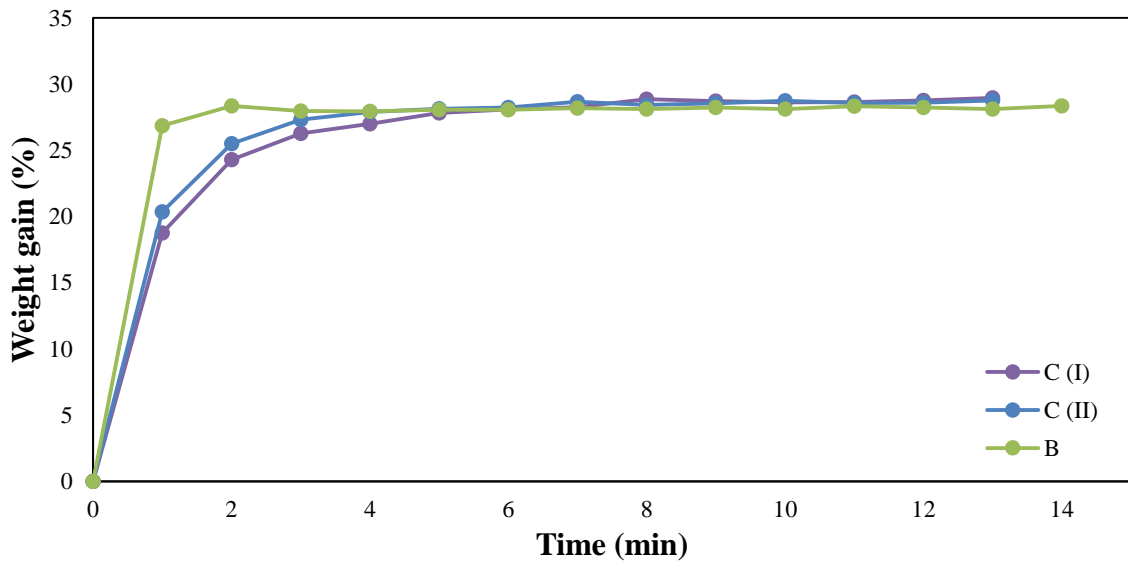
Fig. 4.20 : CPC specimens' weight gain, during first 14 minutes of immersion in Ringer solution.
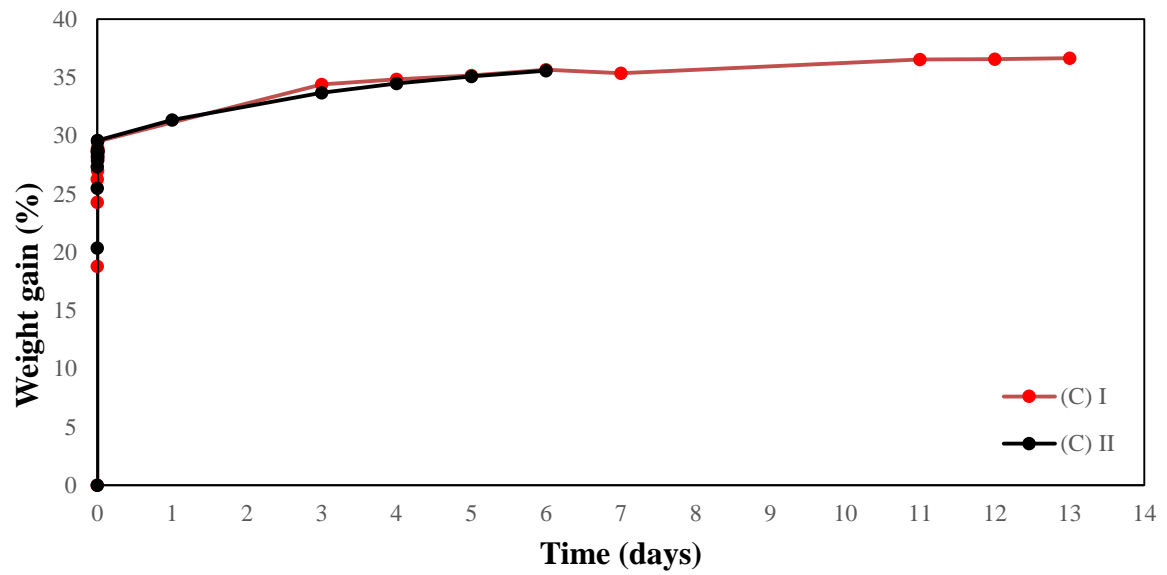
Fig. 4.21 : CPC specimens' weight gain, when immersed in Ringer solution, until saturation levels were reached.

Chapter 5

FBG-based strain investigation

5.1 Implemented method

5.1.1   FBG working principle

Fiber Bragg grating (FBG) sensors have been widely used for measurement of various parameters like pressure, strain, displacement, temperature and humidity in many performance demanding applications in civil engineering, aeronautics, automotive and under sea oil exploration. Their use for sensing applications in biomechanics, although very limited, is becoming increasingly attractive as they combine many advantages over conventional sensors (e.g. strain gages) (77). Such advantages are small size, lightweight, biocompatibility, chemical inertness, immunity to electromagnetic interference and multiplexing capability. The optical fibers used in this work are standard telecom low birefringent, single mode (SM) fibers, having the ability to be equipped with a single Bragg grating of a few millimeters inscribed along their length. A FBG is a periodic modulation of the refractive index of the core of an optical fiber that allows a permanent capability to reflect a narrow light spectrum (78). The FBG reflects light [re(λ)] from an incident broadband source [in(λ)] and transmits without changing all other wavelengths [$\tau(\lambda)$], as Fig. 5.1 represents. The reflected spectrum is characterized by a peak centered on a particular wavelength, λ_B, called Bragg wavelength. The Bragg wavelength, λ_B, is defined by the grating period Λ and the effective index of the propagating mode, n_{eff} (where $n_{eff} = 1.468$), according to the well-known Bragg equation:

$$\lambda_B = 2\, n_{eff}\, \Lambda \tag{5.1}$$

A change in either one of the above parameters changes the reflected wavelength. A temperature increase causes a thermal expansion of the grating resulting to a change of its

period and refractive index. A mechanical strain deforms the FBG and thus changes its period and modifies also the refractive index by photoelastic effects (79). When a FBG sensor experiences a three-dimensional homogeneous thermomechanical strain field, where $\varepsilon_x \neq \varepsilon_y \neq \varepsilon_z$ (z is the direction of the fiber axis) and $\Delta T \neq 0$, the induced change of the refractive index in the cross section of the fiber causes the Bragg peak to split into two distinct ones.
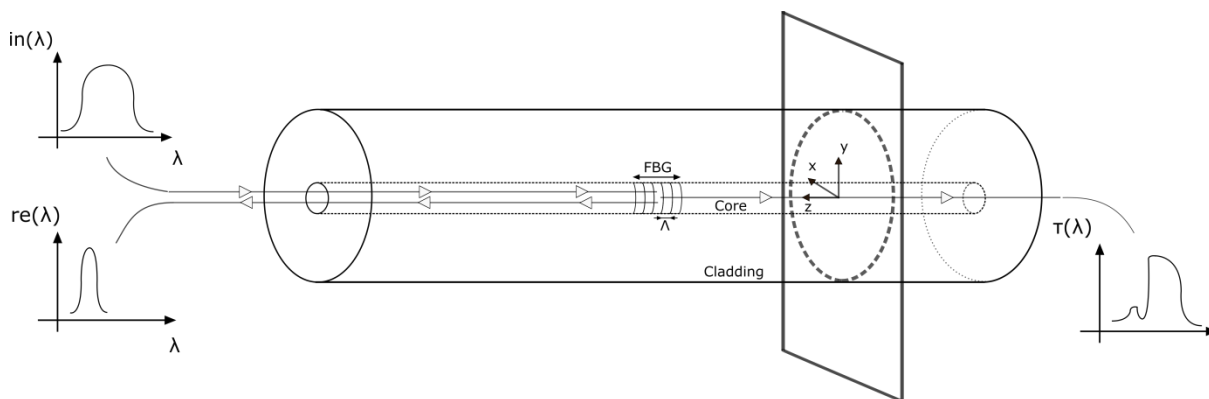
Fig. 5.1: Graphic representation of FBG working principle.

Assuming that the strains of the fiber core are the same as the strains of the optical fiber, the relationship that expresses the wavelength shift versus the three principal strains and the temperature change is given by (78):

$$\frac{\Delta\lambda_{B,x}}{\lambda_{B0}} = \varepsilon_z - \frac{n_{eff}^2}{2}\left[p_{11}\varepsilon_x + p_{12}(\varepsilon_y + \varepsilon_z)\right] + (a_f + \xi)\Delta T \tag{5.2a}$$

$$\frac{\Delta\lambda_{B,y}}{\lambda_{B0}} = \varepsilon_z - \frac{n_{eff}^2}{2}\left[p_{11}\varepsilon_y + p_{12}(\varepsilon_x + \varepsilon_z)\right] + (a_f + \xi)\Delta T \tag{5.2b}$$

In Eq. (2a) and (2b), λ_{B0} is the reference signal (initial Bragg wavelength), p_{11} and p_{12} are the Pockel's strain-optic coefficients ($p_{11} \approx 0.121$ and $p_{12} \approx 0.270$ for silica) and ξ is the thermo-optic coefficient of the fiber (where, $\xi = 8.916 \times 10^{-6}\ {}^0C^{-1}$) (78). In most cases of practical interest the sensor is embedded into a host material, as in the present study, and assuming that the FBG is subjected to axisymmetric loads, that is $\varepsilon_x = \varepsilon_y = -v_f\ \varepsilon_z$, where v_f is the Poisson's ratio of the glass fiber (80) ($v_f = 0.16\text{-}0.19$ for E-glass fiber). Thus $\Delta\lambda_{B,x} = \Delta\lambda_{B,y} = \Delta\lambda_B$, and Equations (2) reduces to the following:

$$\frac{\Delta\lambda_B}{\lambda_{B0}} = (1 - p_e)\varepsilon_z + (1 - p_e)(a_m - a_f)\Delta T + (a_f + \xi)\Delta T + (1 - p_e)\varepsilon_{hugro} \tag{5.3}$$

Where p_e is the effective fiber strain-optic constant defined as $p_e = \frac{n_{eff}^2}{2}[p_{12} - v_f(p_{11} + p_{12})]$ (which renders a value of pe ≈ 0.20). Note that p_e can also be determined experimentally at ambient temperature since the fiber properties can vary according to the manufacturer. Furthermore, α_f is the coefficient of thermal expansion (CTE) of the fiber (where, $\alpha_f = 8x10^{-7}$ °C^{-1} (78)). In the previous equation accounts for the solidification induced residual strains and the term $(\alpha_m - \alpha_f)\Delta T$ for the strains due to thermal expansion mismatch between the optical fiber and the host material. If the strain is constant throughout the sensor, the resulting spectrum appears as a simple sift to a lower or higher wavelength depending on whether the strain is compressive or tensile in nature. When $\Delta T=0$, Eq. (3) reduces to the following simplified version:

$$\frac{\Delta\lambda_B}{\lambda_{B0}} = (1 - p_e)\varepsilon_z \tag{5.4}$$

Additionally, in order to calculate the developed hygroscopic strains due to moisture uptake Eq. 4 takes the following form:

$$\frac{\Delta\lambda_B}{\lambda_{B0}} = (1 - p_e)(\varepsilon_{hygro}) = (1 - p_e)(\varepsilon_z + \beta\frac{\Delta w}{W_{ref}}) \tag{5.5}$$

Where ε_{hygro} are the obtained strains during liquid/moisture absorption and β is the bone cement's coefficient of moisture expansion (CME). In section 5.1.2 is being discussed why the recorded strains ε_z and ε_{hygro} from the FBG sensors correspond to the applied induced strains in the studied bone cement, assuming a perfect interface between the fiber and the material.

5.1.2 Isostrains justification

In order to assume that the recorded strains from the FBG sensors correspond to the applied induced strains from the host material, assuming a perfect interface between the fiber and the material, the strain field must be unaffected from any edge effects. According to a published study (81) in a cylindrical specimen, having the same dimensions as the ones used in this work, the strain field is homogeneous along its longitudinal axis apart from a zone of 8 mm towards cylinder's upper and bottom face. Hence, the strain field in the middle of the specimen, where all the FBG sensors were placed in this study, is certainly not affected by any edge effects.

Additionally, when the cylindrical specimen is subjected to an external strain, a fraction of the applied strain is transferred to the embedded FBG. The amount of strain measured by the FBG is strongly dependent on the ratio of the volume stiffness between the host material and the fiber (82). More specifically, this dependence can be defined from Eq. 5.6:

$$K = \frac{E_m A_m}{E_f A_f} \tag{5.6}$$

Where E_m and E_f is the Young modulus of the material and fiber, respectively and A_m, A_f is the cross section of the cylindrical specimen and fiber, respectively. Numerical studies carried out for the cylindrical specimens employed in this study have shown that values of K as low as ~25 lead to deviations from the isostrains assumption below ~3.2%. This error significantly decreased for higher values of K encountered in this study.

Considering E_m ranging from 350 to 721 MPa during the hardening stage (see Section 3.3), E_f = 72 GPa (83), A_m = 113.040 mm², A_f = 0.012 mm², Eq. (5.6) provides values of K between 45 and 94. Therefore, these values of the stiffness ratio are of considerable magnitude and consequently, it is possible to consider that the isostrain assumption is fulfilled and the measured strains on the FBG sensor can be considered equal to the axial strains on the host material (83).

5.1.3 Multiplexed sensing

As one can conclude, single FBG sensors can be used in order to monitor effectively the strains induced in the host material, in which are embedded. However these measurements concern only the near area close to Bragg grating and as a consequence provide limited information about the overall strain field in the material. Multiplex sensing was developed in order to face this crucial limitation, with two different concepts: serial and parallel multiplexing (84). The working principle is similar as in the case of a single FBG: a broad band light source is introduced through fiber's core however each FBG sensor reflects back a different, unique wavelength. The serial multiplexing has the advantage of using a single source of light while interrogating all the FBG sensors simultaneously. As a result in this work, apart from using single FBGs, serial multiplexing also assisted the investigation of the host material's strain field in order to interrogate a wider area as well as to corroborate the results obtained from

single FBGs. Attention was given from the manufacturer in order the response of each sensor won't overlap the reflected wavelength of the sensors next to them, in loading conditions. On the other hand, in large structures parallel multiplexing is more common since it allows sensing at different locations that can be very distant among each other.

5.2 Experiments

5.2.1 Technical details

5.2.1.1 Single FBGs

Six cylindrical specimens, denoted as S1-S6 in Section 3.2, were fabricated with embedded FBG optical sensors placed along their longitudinal axis while Bragg gratings were located in the middle of them (~20 mm) (Fig. 5.2). Full spectrum measurements from the FBGs were taken using a Micron Optics sm125 optical sensing interrogator, from which the reflected wavelength was obtained. The length of Bragg gratings were of a few millimeters and varied between 1 and 10 mm.
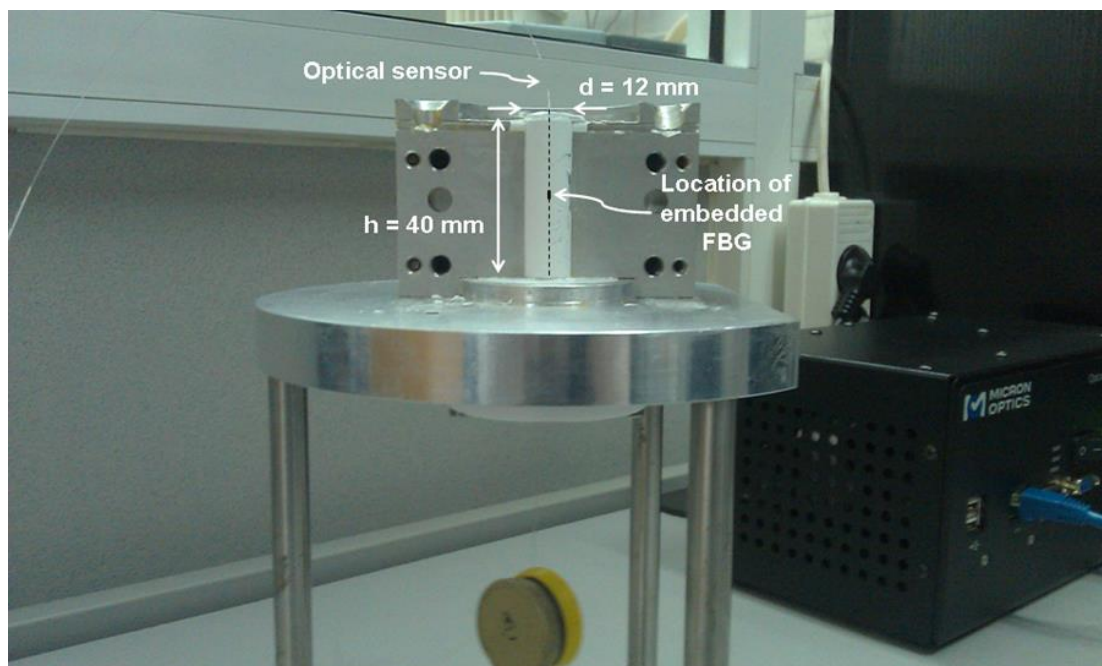
Fig. 5.2 : Embedded single FBG sensor in the middle of a CPC specimen.

The specimens with embedded single FBG sensors underwent through the 2 main stages of a CPC preparation: (a) solidification and (b) hardening. Additionally, a third stage was added, in

which the specimens were dried and subsequently exposed to a liquid and humid environment, respectively. At the same time, the embedded FBGs were interrogated frequently. The ultimate goal was to investigate if any strains are induced in the material, during the main stages of a CPC preparation (solidification and hardening), as well as to monitor the material's hygroscopic response in liquid and wet environment.

5.2.1.2 Multiplexed FBGs

The investigation of induced strains during solidification and hardening period was repeated, by fabricating two more cylindrical specimen (M1, M2), of the same dimensions, with 5 embedded multiplexed FBGs each. The optical sensors were placed again in specimen's longitudinal symmetry axis and the Bragg gratings were located around the specimen's medial. The objective was to investigate if the strain field is homogeneous, in the area where single FBGs were located, and corroborate the already obtained results. For the needs of this work, the distance between the multiplexed sensors was decided to be 5 mm while FBG sensors had a length of 1 mm (Fig. 5.3). In order to define accurately the location of Bragg gratings, in reference to the specimen's longitudinal axis, Optical Low Coherence Reflectometry (OLCR) technique was employed, after specimen's solidification stage was completed.
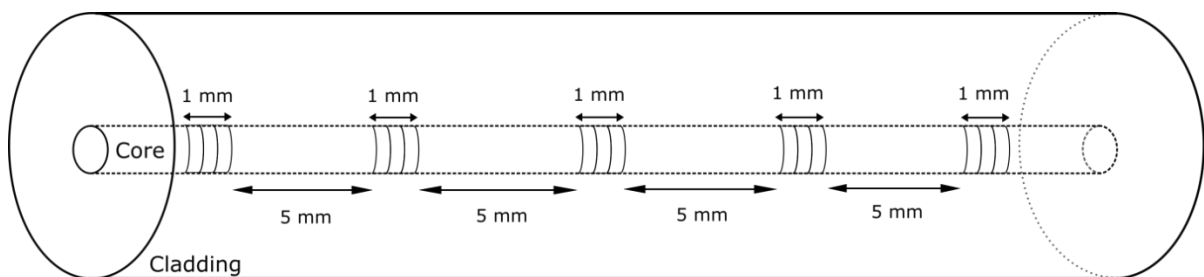
Fig. 5.3 : FBG lengths and their between distance, in multiplexed sensing used for this study.

OLCR setup, schematically depicted in Fig. 5.4, is based on Michelson interferometer whose arms are labeled as test and reference arm. Light from the broadband source and tunable laser are alternatively introduced using the optical switch. The transferred signal passes through an optical circulator and subsequently into the test and the reference arm, using a 3dB directional coupler. Afterwards, the light from reference and test arm is reflected back and enters the coupler, only if the optical length difference of the two arms is smaller than the coherence

length (~25µm) of the light source. The resulting interference signal corresponds to the impulse response, smoothed over a few micrometers, and also to the half of the coherence length. Moving the mirror of the reference arm, the optical distance is changing the causing light, reflected from the mirror, to interfere with the light coming from different FBG positions. An induced displacement Δz of the mirror in the reference arm "selects" the light back reflected from the FBG in the test arm at a slightly different distance from the previous point. The FBG in the test arm is then completely scanned with a maximum spatial resolution given by half the coherence length of the light source (83).
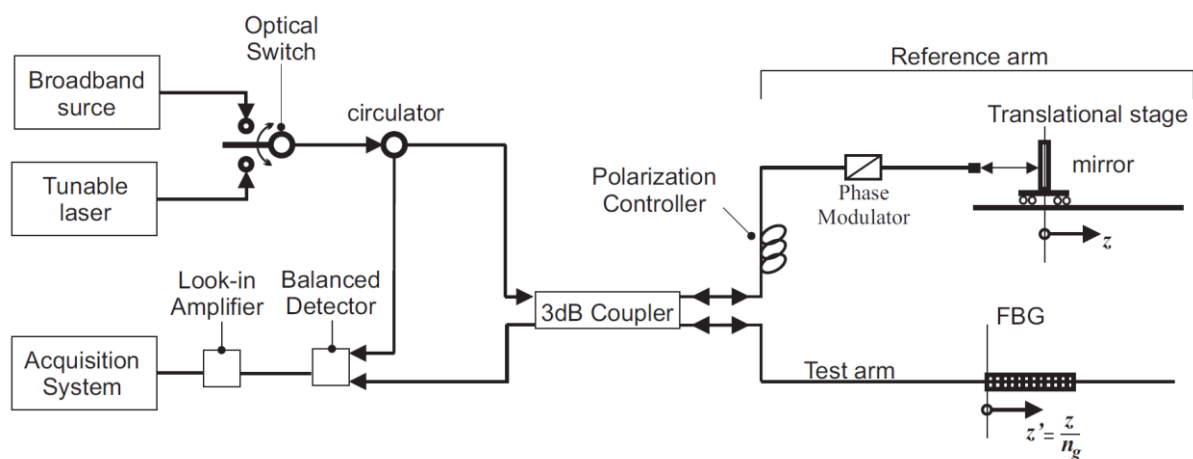
Fig. 5.4 : OLCR setup. Figure retrieved from **(83)**.

The data obtained from implementation of OLCR technique revealed that the Bragg gratings were located symmetrically to the midst of the specimen's longitudinal axis and are schematically illustrated in Fig. 5.5. More specifically, the middle Bragg grating (FBG 3) hardly deviated from specimen's midst (z=0), as their between distance was found to be only 0.1 mm. Additionally, FBG 2 and FBG 4 had a distance, from z=0, of 5.4 mm and 5.7 mm, respectively, while FBG 1 and FBG 5 were found to abstain (from z=0) 11.3 mm and 11.9 mm, respectively. Since all embedded Bragg gratings had a distance more than 8 mm from the edges of the specimens, there were no edge effects that could affect the calculated strains (85).
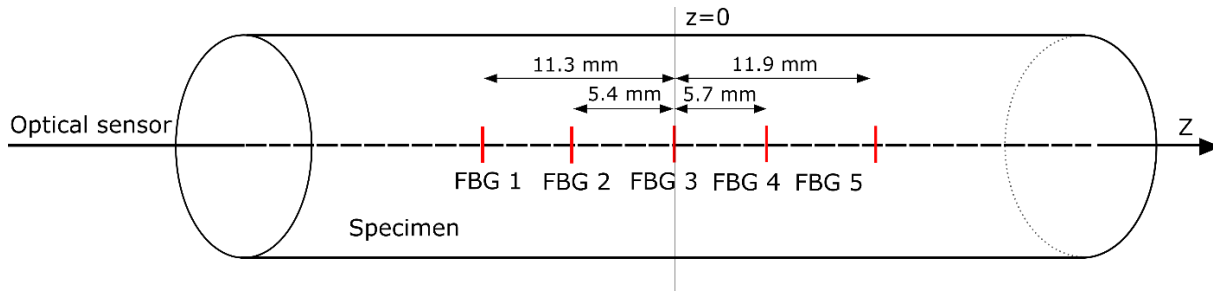
Fig. 5.5 : Locations of the embedded multiplexed FBGs, in reference to specimen's longitudinal axis midst (z=0), obtained by using OLCR technique.

5.2.2 Results

5.2.2.1 Solidification

As far it concerns solidification period, the interrogated wavelengths (λ_{B0}, λ_B) and corresponding strains (ε_s) for single and multiplexed embedded FBGs are presented in Table 5.1, for two characteristic stages (initial and final) of this time period. The first one (before FBG embedment) corresponds in a state where the optical sensor is mounted on the mould, but no CPC paste has been casted in the mould's cavity. The reflected wavelength of this state will be considered as a reference value (λ_{B0}). As final stage of the solidification period was chosen the state where each specimen was recovered from the mould and before its immersion in the hardening liquid, at a free state. The two different interrogated wavelengths (λ_{B0}, λ_B) were used in Eq. 5.4, from which the induced strains (ε_s) were calculated. Each presented value is the mean value obtained from 10 consecutive measurements during FBG's interrogation and the maximum difference between them was found to be ~25 µε.

It can be seen that the strains obtained from single FBGs are compressive which means that there were induced residual strains during solidification. Nevertheless are of low magnitude, while a variation is exhibited. More specifically, in S1, S2, S3 and S5 specimens the exhibited strains were between -514 and -795 µε, while for S4 specimens the calculated strains are -1113 µε. In the case of multiplexed FBGs (specimens M1 and M2), the calculated strains from the interrogation of multiplexed FBGs in specimens M1 and M2 are also compressive and a variation is exhibited again. Specifically for specimen M1, from three FBGs (FBGs 1, 2 and 5) the exhibited strain values were between -281 and -117 µε while for FBG 3 and 4 were -803

and -737 $\mu\varepsilon$ respectively. In M2 specimen the obtained strain values are more comparable between them, as they range between -431 and -642 $\mu\varepsilon$.

Specimen		Before FBG embedment		After specimen's recovery and before immersion in the hardening liquid	
		λ_{B0} (nm)	ε ($\mu\varepsilon$)	λ_B (nm)	ε_s ($\mu\varepsilon$)
Single FBGs	S1	1550.385	-	1549.760	-513.54
	S2	1550.260	-	1549.86	-328.69
	S3	1550.222	-	1549.945	-345.12
	S4	1550.189	-	1548.835	-1112.66
	S5	1550.146	-	1549.442	-578.54
Multiplexed FBGs M1	FBG 1	1541.021	-	1540.680	-280.97
	FBG 2	1545.923	-	1545.778	-117.09
	FBG 3	*1550.930*	*-*	*1549.952*	*-803.12*
	FBG 4	1556.039	-	1555.139	-737.13
	FBG 5	1561.000	-	1560.647	-288.321
M2	FBG 1	1541.027	-	1540.507	-430.614
	FBG 2	1545.981	-	1545.340	-528.831
	FBG 3	*1550.964*	*-*	*1550.219*	*-612.851*
	FBG 4	1556.016	-	1555.244	-632.164
	FBG 5	1560.987	-	1560.200	-642.281

Table 5.1: Obtained reflected wavelengths and the corresponding strains from the embedded single and multiplexed FBGs, at two different stages of solidification period.

From the obtained strain values the exhibited range in strain magnitudes is considerably high, in reference to the strain values, however this cannot be attributed to the existence of a non-homogeneous strain field. The latter is based on the fact that the strains calculated from the multiplexed FBGs of M2 specimen are comparable between them. Consequently, a number of factors, presented in the next paragraph, have introduced non-negligible errors.
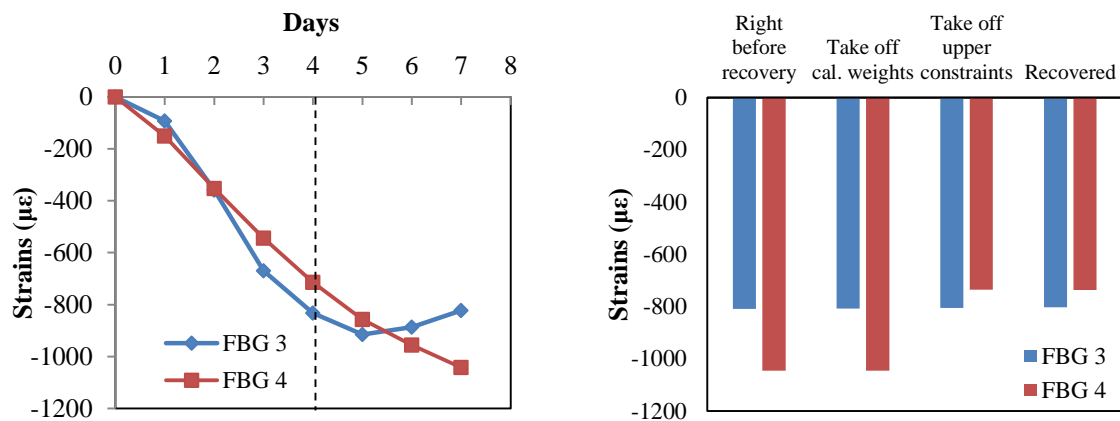
Fig. 5.6 : (left) Obtained strain values from 2 FBGs of M1 specimen during solidification period (right) obtained strain values during recovery of M1 specimen from the same FBGs.

A parameter that resulted in different strain values is the different solidification levels among the regions where FBGs were embedded. This was concluded when solidification period was prolonged to 7 days for M1 specimen, while daily measurements were taken and the corresponding results for FBG 3 and 4 are presented in Fig. 5.6a. As it can be observed, while in FBG 3 the obtained strain value was practically levelled off after 4 days, in FBG 4 was still developing even after 6 days since solidification period started. In general, solidification process is strongly related to (a) humidity levels of the mould's surrounding environment and (b) to the amount of the aqua solution the CPC slurry has. As a result any slight changes in these parameters could have introduced differences in the magnitude of the obtained strains. Moreover in Fig. 5.6b are presented the calculated strain values at 4 characteristic stages of M1 specimen recovery. While for FBG 3 there are practically no changes in the magnitude of the calculated strains, this does not apply in the case of FBG 4. Consequently, non-negligible errors were also introduced during the specimens' recovery.

Another parameter that has affected the exhibited strain values may be the existence of air void(s) in the specimen, close to the region where the FBGs were embedded. The latter is supported by the figures presented in Fig. 5.7, recorded when microscopy investigation was also implemented for a cylindrical specimen with an embedded optical fiber that simulated an optical FBG sensor (dummy fiber). As it can be seen, large voids exist in the region close to the optical fiber and they even prevent the creation of an interface between the bone cement and the fiber. Given the fact that several voids of hundreds of microns exist in the bone cement,

as it has been demonstrated in section 4.2.2, one can conclude that FBG measurements can be affected from local edge effects, because of the voids, in the examined material.
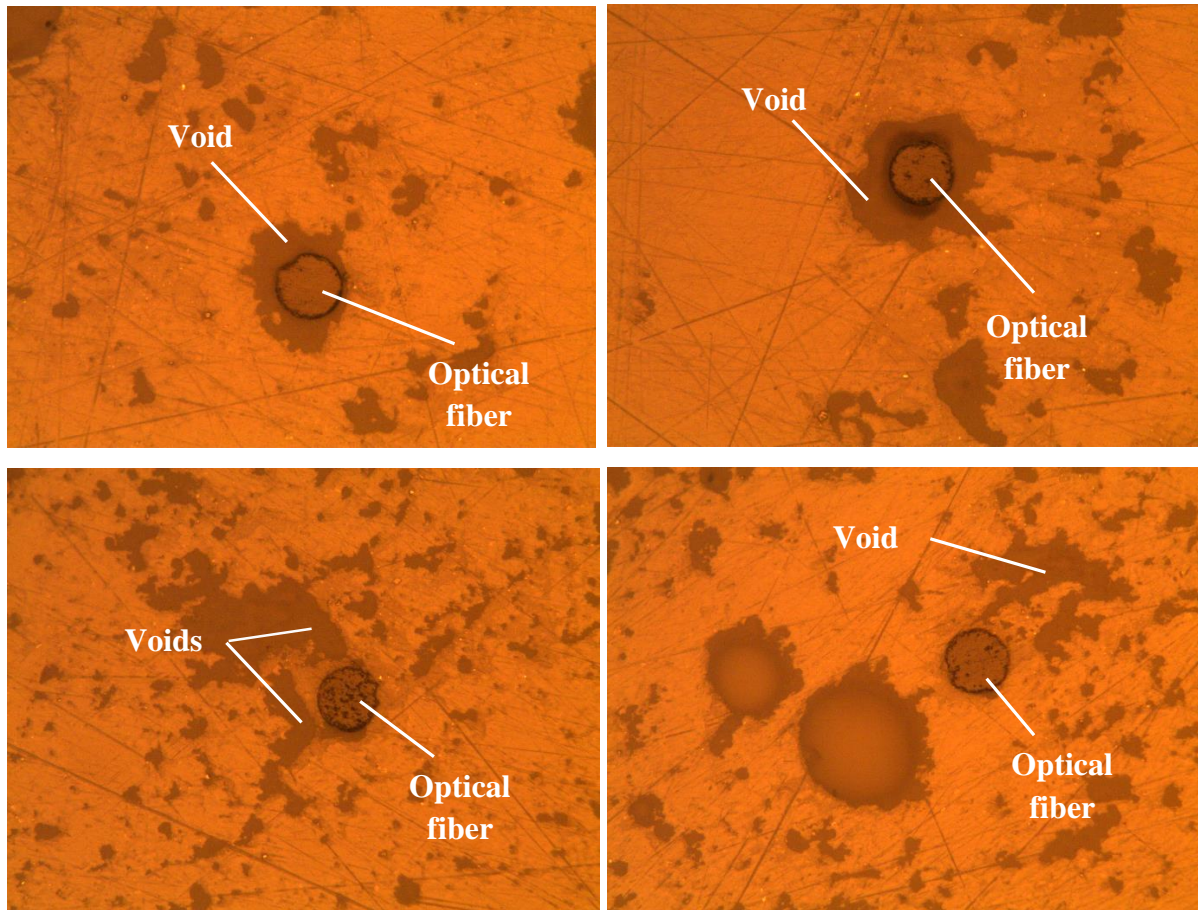
Fig. 5.7 : Observed air voids in the bone cement, that environ the embedded optical fiber.

5.2.2.2 Hardening

In Fig. 5.8 the strain values (ε_h), obtained from the implementation of Eq. 5.4, that concern the hardening stage are presented in a diagram. Hardening process lasted at least 15 days, since during in this time interval microstructural changes take place as demonstrated in section 4.1, and was completed when the stain values were levelled off. The interrogated reflected wavelength from specimens S2 and S3 coincided with the reference wavelength (when the optical fiber was not embedded), suggesting that the interface between the bone cement and the optical fiber was severely damaged. As a result they were not taken into account. It is also noted that the strain values of "0 day" were obtained after several minutes passed since

specimen's immersion in the hardening liquid. Hence, any significant effect of the absorption phenomenon in the strain values, thoroughly discussed in section 5.2.2.3.1, is excluded from these measurements. From a first rough analysis, it can be observed that the calculated strain values from all specimens range between ~-390 με and ~-244 με after their immersion in the Ringer solution and are slowly decreasing until they reach a magnitude of ~-100 με where they were stabilized. The latter was also confirmed from the strain values obtained from specimen S4 after the 30 days of hardening, when the hardening period for this specimen was prolonged for 10 more days.

For the rest specimens, during the first days (3-7 days) an initial linear behavior of the FBG-based recorded strains is exhibited. During this time interval an initial crystal growth was observed during SEM investigation (section 4.1.1) and depicted in Fig. 4.1a-c, leading to the conclusion that the change in strain readings over time could be attributed to the formation of the observed crystal structures. After the first days of hardening passed, strain values exhibit a new, of different slope, linear pattern until the 30th day of immersion. For the same time interval a clear entanglement of the created crystal structures was observed for the first time from the SEM images (Fig. 4.1d). In the following days, the entanglement became more complex as it is depicted from Fig. 4.1e and f, recorded at 8 and 10 days of immersion. The entanglement of the crystal structures that resulted in a complex network, appears to be the cause that strain values exhibited a different linear slope. The obtained strain values from specimen S1 exhibits a different strain pattern. Specifically, during the first 12 days of immersion in the Ringer solution, strain values exhibit a plateau of a mean value of -230 με, while afterwards a new, second plateau appears where the strains retain a mean value of -90 με. However, in the case of S1 specimen hardening stage took place in a room environment while for the rest specimens in an environmental chamber, with settable temperature. Thus, it is concluded that unavoidable room temperature variations, during hardening of S1 specimen, have affected the strain measurements.
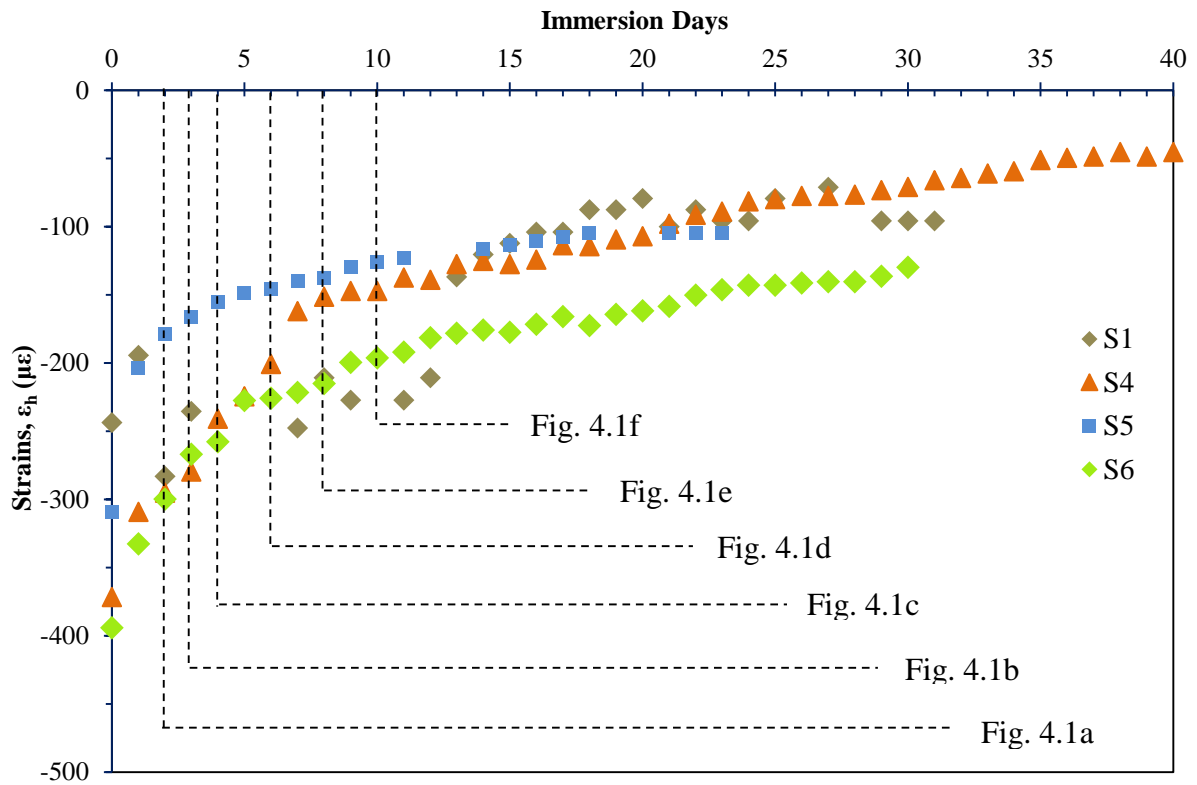
Fig. 5.8 : Induced strains obtained from single FBGs, during hardening period.

Ginebra et al. (27) and Komlev et al. (53) have conducted SEM investigations in self-setting calcium phosphate bone cements during hardening stage. They have reported that the observed microstructural changes were completed after 12-15 days of samples' immersion into the hardening liquid instead of ~25 days obtained in the present study. However, Zhang et al. (6) reports that various parameters such as smaller particle size, higher setting temperature and low liquid-to-powder ratio can affect kinetics and as a consequence CPCs' setting time. Considering that the aforementioned parameters were not the same with the ones of the present study, such differences in the time period where microstructural changes take place are expectable.

Fig. 5.9 : Induced strains obtained from multiplexed FBGs, during hardening period.

Specimens M1 and M2, with the embedded multiplexed FBGs, were also hardened in a room temperature (23 ^{0}C), for 20 and 11 days respectively, and the calculated strains from the interrogation of the Bragg gratings are presented in Fig. 5.9. As it can be observed the exhibited strain values, when the specimens were initially immersed in the hardening liquid (0 day), are between -420 με and -183 με which is comparable to the exhibited strain interval obtained from single FBGs (~-390 με and ~-244 με). In the following days the calculated strains were progressively decreased but slight differences exist in the exhibited strain patterns. More specifically, the calculated strain values obtained from the multiplexed FBGs embedded in M1 specimen present a single linear behavior during the whole hardening period. It can also be observed that the slope of this linear behavior is similar to the slope exhibited in strain readings obtained from single FBGs, after the first 3-7 days of hardening. In the case of M2 specimen, strain values are slightly lower than the one obtained in M1 specimen and seem to present 2 different slopes: the first one which is defined from the first two strain values (0 and 1 day) and

the second one, not that steep as the first one, which is defined from the rest strain values and is similar to the slope exhibited from strains values of M1 specimen.

The low magnitude of the obtained strains, also corroborated from the multiplexed FBGs, suggest that no significant residual strains were created during the bone's cement immersion in the Ringer solution and the subsequent hardening. Thus, deformation due to hardening is negligible and the specimen preserves its dimensions when immersed in the liquid media. This later property is crucial since parts made from this material in the human body can preserve their dimensions during hardening.

5.2.2.3 Re-immersion

5.2.2.3.1   Liquid environment

After hardening period, one of the single FBG instrumented specimen (S5) was dried in 50 ^{0}C for 2 hours, in order to subtract the liquid content absorbed during hardening period, and then re-immersed in the Ringer solution. Meanwhile the reflected wavelength from the Bragg gratings was interrogated every minute for the first 13 minutes. Thus, the developed c strains (ε_{hygro}) were calculated and presented in Fig. 5.10, by implementing Eq. 5.5. More measurements were also taken from the Bragg sensor in the following days, every 24 hours, until saturation levels were reached and the calculated strains are presented in Fig. 5.12. Since the experiment was conducted twice, the obtained results were numbered as (I) and (II), respectively Additionally, in the presented graphs are also included the results reported in section 4.4, that concern the weight gain (W_L) of a same cylindrical CPC specimen without embedded FBG sensor (specimen D). For both experimental runs, designated as ε_{hygroI} and $\varepsilon_{hygroII}$, a rapid strain evolution takes place reaching values of -305×10^{-6} ($\mu\varepsilon$) and -254×10^{-6} ($\mu\varepsilon$) respectively, within the first two minutes of immersion into the Ringer solution, while at the same time a rapid liquid uptake occurred. In the following minutes and days, a further evolution of the hygroscopic strains is exhibited, but with a lower rate, until saturation levels were reach and the developed strain values were levelled off at -290×10^{-6} and -250×10^{-6} ($\mu\varepsilon$), at the first and second conduction of the experiment respectively. It is noted that the differences in the recorded strain values can be possibly attributed to the fatigue of the interface between the FBG sensor and the bone cement material, due to the successive drying-swelling process that the

sample had to undergo to repeat the re-immersion experiments. Moreover, the fact that the measured hygroscopic strains exhibited the same behavior as the specimen's liquid gain, suggest that the material's absorption process can be monitored in an effective way leading to the conclusion that FBGs can be used to investigate CPCs kinetics.
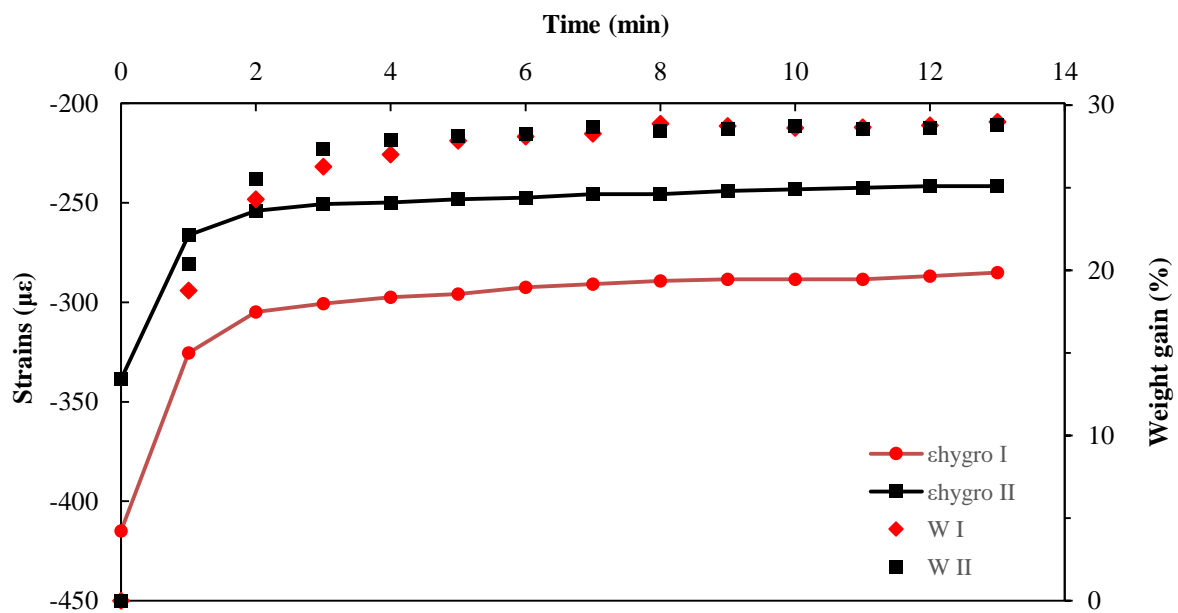
Fig. 5.10 : Evolution of hygroscopic strains, in liquid environment, during the first 13 minutes of immersion.

The fact that low magnitude hygroscopic strains are developed during specimen's immersion in liquid media is also corroborated from the obtained results of another conducted experiment, based on an optical method. Specifically specimen D was dried and then placed in a metallic support on the bottom of a small bath. Then the bath was filled with Ringer solution in order to completely cover the specimen and subsequently let to reach fully saturated conditions. At the same time several images were acquired with a camera, placed vertically to the specimen's longitudinal axis at a certain height, with the use of a metallic bracket. It is noted that the metallic support, the bath as well as the metallic bracket were strictly fixated. For each recorded image a specific length in the specimen's surface, that was pre-marked with a pencil, was software measured in terms of number of pixels, designated as l(t). Then, any developed

longitudinal expansion (ε_o) of the specimen was calculated through the implementation of the following equation:

$$\varepsilon_o = \frac{l_t - l_0}{l_0} \tag{5.7}$$

where l_0 is the pre-marked length measured from the camera when the specimen was placed in the empty bath at a dry state. The above described configuration is illustrated in Fig. 5.11. From the obtained results no developed strains were found, suggesting that their magnitude was well-below the resolution of the method, which corresponds to ~1000 $\mu\varepsilon$ for a change of 1 pixel in the measured length.
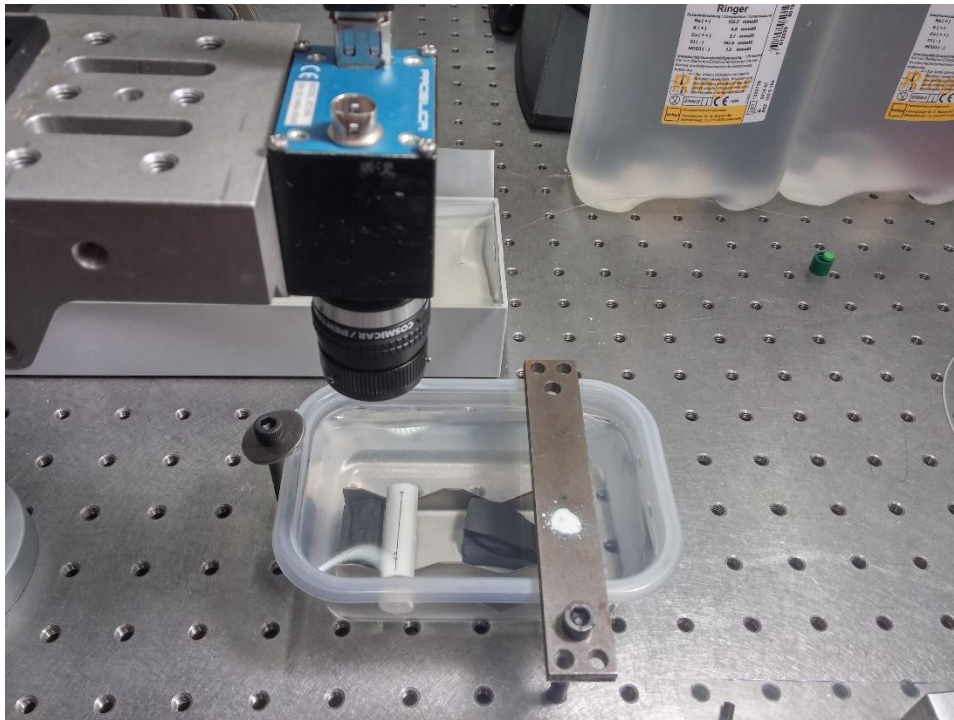
Fig. 5.11 : The experimental configuration for the investigation of the developed hygroscopic strains, with an optical method.

The developed hygroscopic strains are also presented as a function of sample's weight gain in Fig. 5.13 where the data can be approximated by two slopes. The first slope is exhibited when the sample's weight gain is between $0 \leq W < 29$ % and its value was calculated to be $B_{(1I)} = 3.75 \times 10^{-6}$/%w/w ($r^2 = 0.971$) and $B_{(1II)} = 2.74 \times 10^{-6}$/%w/w ($r^2 = 0.9059$) for the two experimental trials (I and II), respectively. The second slope is appearing for a liquid uptake

range of $29 \leq W < 37$ %, where the corresponding values were $B_{(2I)}=16.2 \times 10^{-6}$/% w/w ($r^2=0.9856$) and $B_{(2II)}=11.3 \times 10^{-6}$/% w/w ($r^2=0.9929$). In order to calculate the material's coefficient of moisture expansion (CME), designated as β in Eq. 5.5, an equilibrium must be achieved between the specimen and the surrounding environment, when the weight gain and the hygroscopic strains were obtained. Hence, the value of β can be approximated from the values of specimen's weight gain (W) and the corresponding hygroscopic strains (ε_{hygro}) obtained at two different conditions, in which the aforementioned requirement is met: (a) in a completely dry state of the specimen where (W, ε_{hygro})=(0,0) and (b) in completely saturated conditions of the specimen, where W =37 % according to the obtained experimental data. Thus the following values of β were calculated, based on the first and second experimental run respectively: $\beta_I=7.02 \times 10^{-6}$/% w/w, $\beta_{II}=4.96 \times 10^{-6}$/% w/w.
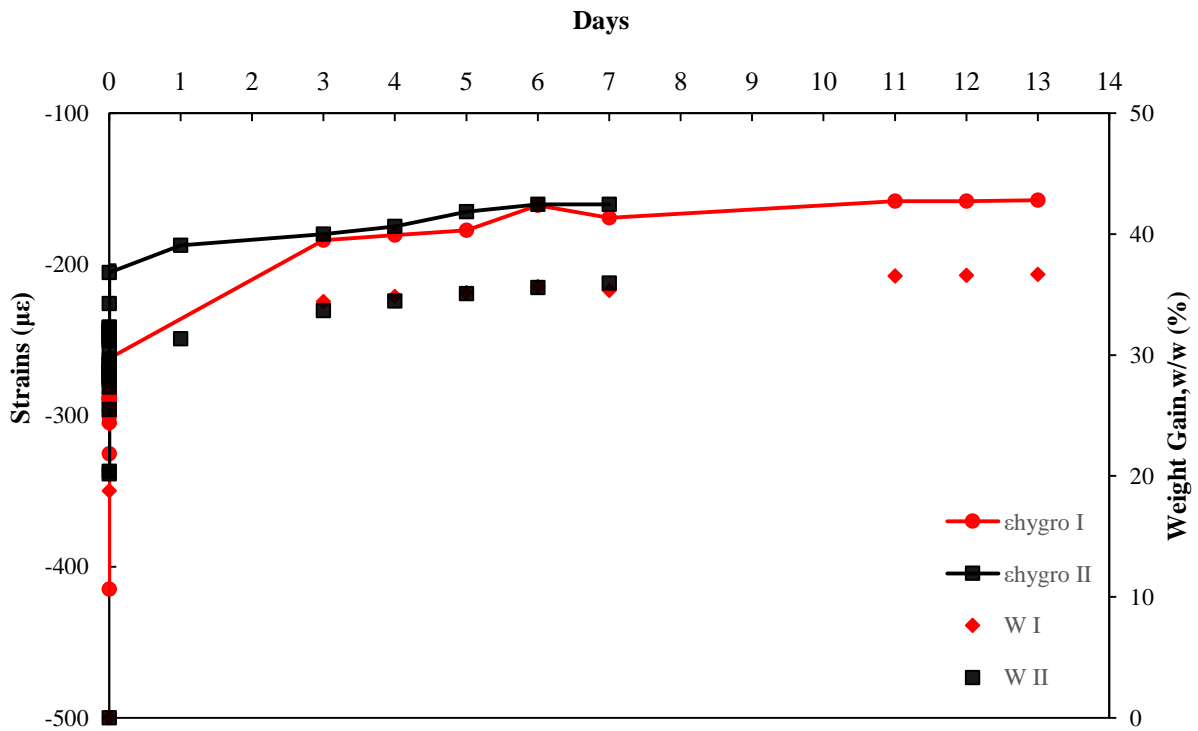
Fig. 5.12 : Evolution of hygroscopic strains, in liquid environment, until sample's saturation.
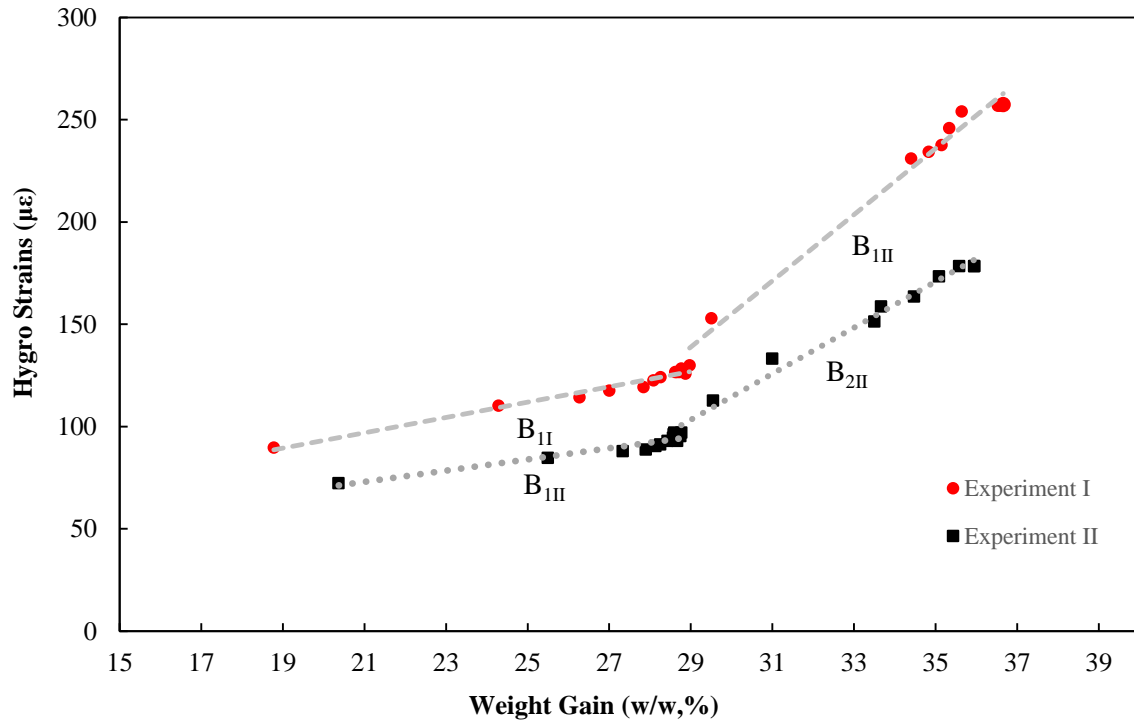
Fig. 5.13 : Hygroscopic strains as a function of sample's liquid content.

5.2.2.3.2 Humid environment

Specimen S6, after the hardening period, was also dried for at least 2 hours in an oven and then was placed in an environmental chamber with settable values of relative humidity (RH), under a stable temperature of 23 ^{0}C. The initial set value of RH was 25% and was increased by 5% each time, when equilibrium between the sample and the surrounding environment was achieved, and up to a maximum value of RH (80%) reached by the environmental chamber. At the end of each RH increment, the sample was weighed using the same method followed in section 5.2.2.3.1 and the peak wavelength from the optical fiber was recorded. In Fig. 5.14 the developed hygroscopic strains as a function of sample's moisture content, designated as W_H, in a humid environment are presented. The strains values exhibit a variation trend that was found to have a slope value of $\beta=3.98 \times 10^{-4}$/%w/w for a moisture uptake range of $0.9 \leq W_H < 3.8$. The calculated slope was found to be two orders of magnitude higher than the ones obtained for the case of the liquid immersed specimens. As one can conclude, the hygro-strain values range between the magnitudes exhibited when the specimen is dried (solidified) and fully

saturated. Hence, this high difference in slopes, between humid and liquid environment, can be attributed to the presence of different and complex diffusion mechanisms (86) and specimens' fabrication parameters such as pore size, interconnectivity of pores, tortuosity, and in general to the different way with which the pores are filled in a humid environment, seem to have contributed in this exhibited difference of CME values between humid and liquid environment for the examined material.
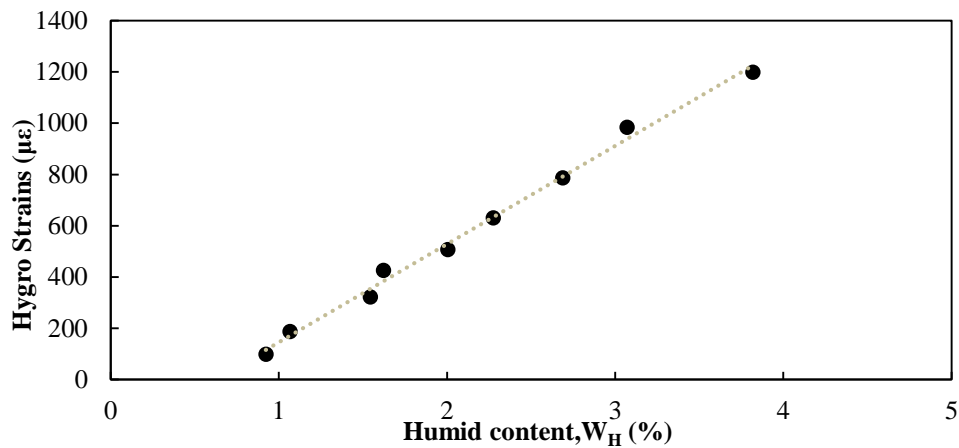
Fig. 5.14 : Hygroscopic strains as a function of sample's humid content.

In Fig. 5.15 a linear variation of weight change to relative humidity is presented for the examined RH interval (25-80%). A similar linear behavior up to 90% RH is reported by Shinsaku Tada et al. work (87) for a cement based material while a sharp increase of its slope was observed for 90-100% RH.
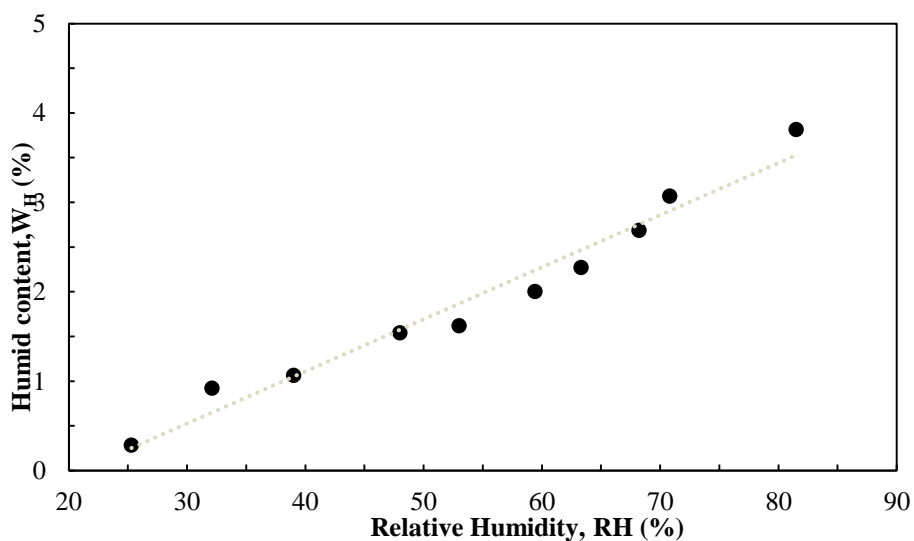
Fig. 5.15 : Hygroscopic strains, in humid environment, as a function of relative humidity.

Chapter 6

Modeling and Finite Element Analysis

6.1 Introduction

The use of simulation models aims either to validate any obtained experimental results or to investigate a case which is too challenging to be implemented in reality for various reasons e.g. need of complex configurations, limitations in material quantities etc. The first simulation attempts were achieved using analytical models, at times where the development of computers was still in early stages and the available computational power was limited. Hence, several drawbacks existed in developing reliable models and any obtained results often suffered in terms of accuracy since the models concerned over-simplified cases which abstained a lot from the reality. However, in the recent years the use of computers became widespread and the processing power has greatly increased, leading to a wider development of complex, credible simulation models which verge on reality and provide high precision results. Moreover, finite differences method as well as Finite Element Method (FEM), that require high computational resources, are now broadly used for implementing 2-D and 3-D models. In this work, an implementation of simulation models, using the above mentioned methods, was achieved: the first one simulated the absorption phenomenon, using finite differences method, and its results were imported in a FEM model in order to calculate the induced strains, when the studied CPC is immersed in wet environments. Moreover, a complex 3-D model was developed in a simulation software, using Finite Element Analysis, for the investigation of the distributed stress fields in the examined CPC as well as for the whole system configuration, in a real-life application (case study).

Finite difference is a numerical method for solving differential equations, based on the following equation:

$$f'(a) \approx \frac{f(a+h)-f(a)}{h} \tag{6.1}$$

which comes from Taylor's theorem. Since the use of this method is dominant to numerical solutions of partial differential equations (88), it was used in order to develop diffusion models that simulate the absorption phenomenon in the studied material. The cylindrical specimens, used to obtain the weight gain experimental results, present symmetry in x and y axis thus an axisymmetric model was considered. In this case the area of interest is modelled with a mesh of $[(x_1, y_1), \ldots, (x_i, y_j)]$ points, the time in $(t_1, \ldots, t_n)$ steps, where a non-uniform partition both in space and time intervals is considered for the needs of this work. A graphic representation of the above exists in Fig. 6.1. Since diffusion models, thoroughly presented in 6.2, have second-order differential terms three different approaches exist in expressing them with finite difference method:

(a) using forward difference at time n and position (i,j):

$$\frac{u_{R+1}^n - 2u_{R+1}^n + u_{R-1}^n}{h^2}, R = i, j \tag{6.2}$$

(b) using backward difference at time $n+1$ and position (i,j):

$$\frac{u_{R+1}^{n+1} - 2u_{R+1}^{n+1} + u_{R-1}^{n+1}}{h^2}, R = i, j \tag{6.3}$$

(b) using Crank-Nicolson method at time $n, n+1$ and position (i,j):

$$\frac{1}{2} \left(\frac{u_{R+1}^{n+1} - 2u_{R+1}^{n+1} + u_{R-1}^{n+1}}{h^2} + \frac{u_{R+1}^n - 2u_{R+1}^n + u_{R-1}^n}{h^2} \right), R = i, j \tag{6.4}$$

The explicit scheme (forward difference) is the least accurate and can be unstable, however is the easiest to implement and the least numerically intensive. As a result, this approach was adopted.

In the case of Finite Element Method the area or volume to be modelled is sub-divided into smaller, elementary parts (Fig. 6.2). As a result a mesh of finite elements is created, where each element is constituted of a number of nodes. Then for a given set of boundary and initial conditions, field parameters such as stress, strain, displacement, temperature distribution, etc.

can be obtained in these nodes and consequently for the whole modelled area or volume. This is achieved by solving a system of N equations with N unknowns ([N]x[N] system), where N corresponds to the number of nodes times the number of unknown field parameter components per node (85). The above described procedure is achieved through the use of a user-friendly commercial software, in which suitable commands are given. For the needs of this work, Abaqus 6.11® simulation software package was employed for the implementation and analysis of Finite Element models.
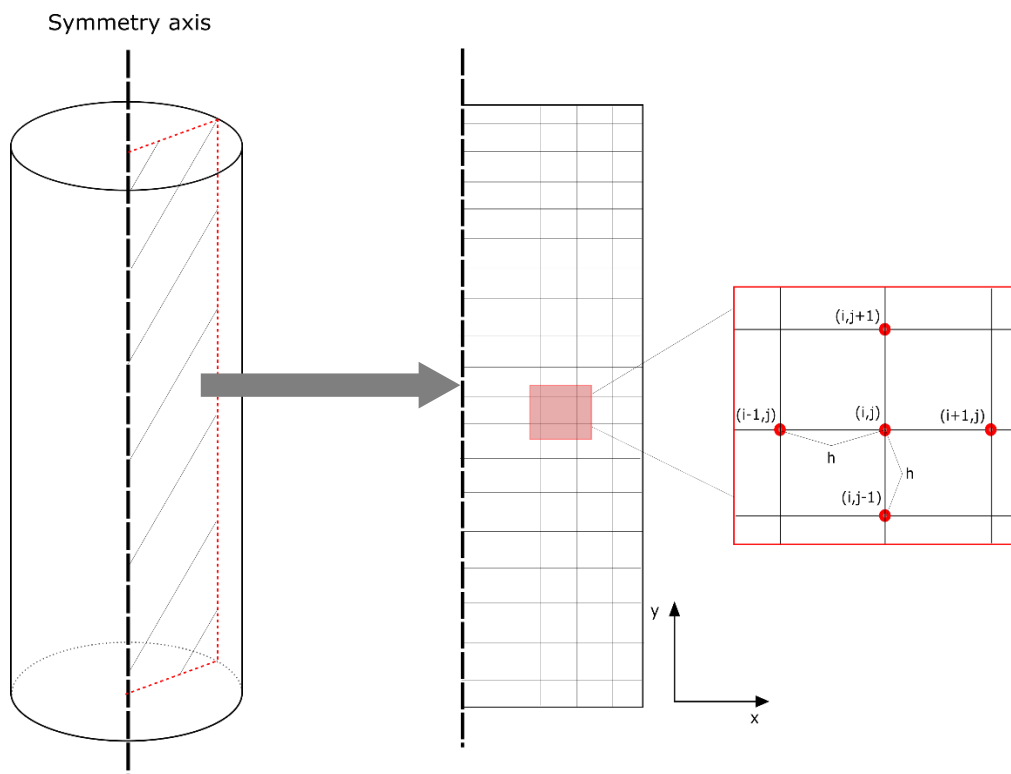
Fig. 6.1: Graphic illustration of the considered axisymmetric modelling, for a cylindrical geometry.

A number of parameters influence the accuracy of the results obtained from a Finite Element Analysis (FEA). For instance, the results error is depended on the size of the elements, in respect to the dimensions of the modelled area, especially in regions where the researched fields may vary with high gradient, or complex phenomena are simulated e.g. friction. However the needed computational power for a large number of elements is also increased and as a result an offset must be found between the available computational resources and the number of elements. This is often achieved by sufficiently refine the element mesh in the regions of

interest. Additionally, the accuracy of the obtained results from a FE Analysis is related to the distortion in which the elements are "subjected" in the analysis, especially in the case of a 3-D model. For this reason, different categories of elements exist and the most suitable must be chosen in every case, in order to keep the distortion to a minimum level. In general no simple rule applies for the number, size and geometry of elements that should be used in a developed model and only a posteriori parametric study can provide information on the reliability of the results (85).
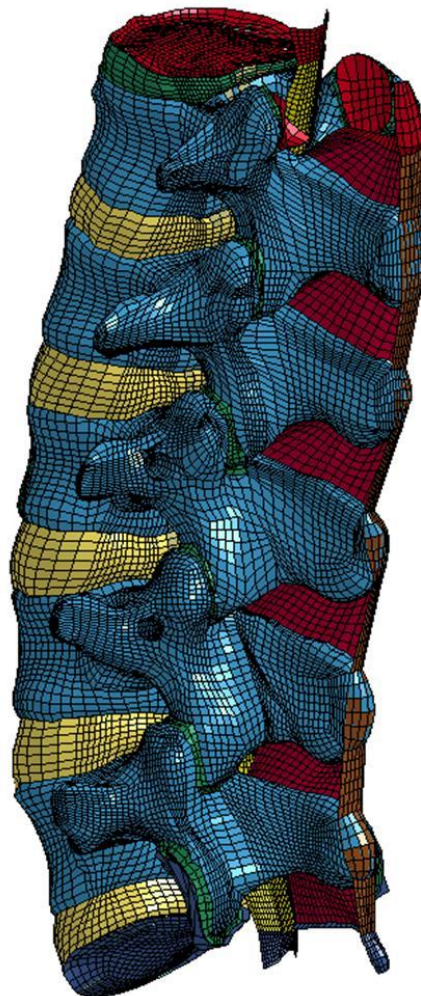
Fig. 6.2 : A finite element model of the lumbar spine **(89)**.

6.2 Absorption phenomenon and developed hygro strains

In order to model the absorption phenomenon with the use of finite difference method, 3 different models that describe the diffusion phenomenon were developed:

i) Fick's law:

$$\frac{\partial u}{\partial t} = D_f \left(\frac{\partial^2 u}{\partial^2 x} + \frac{\partial^2 u}{\partial^2 y} \right) \tag{6.5}$$

where (u) is the normalized weight gain, (D_f) is the diffusion coefficient,

ii) Langmuir law:

$$\frac{\partial u_f}{\partial t} + \frac{\partial u_b}{\partial t} = D_l \left(\frac{\partial^2 u}{\partial^2 x} + \frac{\partial^2 u}{\partial^2 y} \right), \frac{\partial u_b}{\partial t} = \gamma u_f - \beta u_{fb} \tag{6.6}$$

where (u_f) is the normalized weight gain of the liquid that has not been absorbed yet, (u_b) is the normalized weight gain of the absorbed liquid, (D_l) is the diffusion coefficient and γ and β are constants called probabilities,

iii) Power law

$$\frac{\partial u}{\partial t} = D_m \left[\frac{\partial}{\partial x} \left(u^m \frac{\partial u}{\partial x} \right) + \frac{\partial}{\partial y} \left(u^m \frac{\partial u}{\partial y} \right) \right] \tag{6.7}$$

where (u) is the normalized weight gain, (D_m) is the diffusion coefficient and (m) an exponential constant.

From the three diffusion models, Fick's and Langmuir law diffusion models were successfully implemented in Matlab® software. In order to face the instability issues short spatial increments were used in the nodes that were close to the edges and increased towards the symmetry axis. The same approach was also used for the time increments: the first time increments were short and were increased towards the end of analysis. As weight gain results, in each time increment, was considered the sum of the calculated (u) values from all calculated time increments. Random values were given to the unknown parameters for the implementation, however they were defined though a process described in the next paragraph. In the case of implementing power law diffusion model the arised instabilities could not be overpassed and as a result this diffusion model was dropped. For reasons of time saving, the modeling concerned the first 100 minutes of immersion, since it is a large enough time interval to simulate the weight gain as

well as induced hygro-strains, as it was demonstrated in sections 4.4 and 5.2.2.3.1 respectively. Moreover the required computational resources for a longer simulated time interval would be heavily increased, due to the fact that a considerably denser mesh of nodes and time would be necessary in order to avoid any instability issues. Although both models can describe with high accuracy the weight gain for the considered time interval (Fig. 6.3), Fick's law cannot predict any additional weight gain for time periods longer than the one simulated. The reason is that a single value of absorbed liquid concentration (u) is calculated for each time increment which is levelled off once saturation levels are reached. On the other hand, in Langmuir law apart from the gained liquid quantity (u_b) it is also taken into account a liquid concentration which is "free" and available for absorption (u_f). For this reason, Langmuir law is suggested for porous materials, where u_f represents the concentration of liquid media that has occupied the materials' pores but has not been absorbed from the material. Considering this difference between the models, Langmuir's diffusion model was finally chosen to simulate the absorption phenomenon, for the needs of this work

The next step was to define the unknown parameters of Langmuir law, though optimization process. Specifically in Origin® software, the experimental data of material's weight gain in liquid environment for the first 100 minutes were imported (see section 4.4) as well as the approximate analytical solutions for a cylindrical geometry, described from the following equations respectively (90):

$$\frac{M_t}{M_\infty} \approx \frac{\beta}{\beta+\gamma}\exp(-\gamma t)\left[1 - \exp\left(-7.3\left(\frac{D_l t}{(2\pi r h)^2}\right)^{0.75}\right)\right] + \frac{\beta}{\beta+\gamma}\exp(-\beta t) + [1 - \exp(-\beta t)] \qquad (6.8)$$

where M_t is the amount of liquid media absorbed at (t) time and M_∞ at saturation levels. Then the software, though an iteration process, defined the values of the unknown parameters with which the results of analytical solutions present the best fitting with the experimental data: D_l= 0.13 mm²/sec, (γ) = 0.00257 and (β) = 0.06862. It is stressed out that the defined diffusivity coefficient (D_l) acts as the effective diffusivity coefficient (D_{eff}) of the specimen, since it is porous, which is correlated with the material's diffusion coefficient, porosity and tortuosity through the following equation:

$$D_l = D_{eff} = \frac{D'\varepsilon}{\tau} \qquad (6.9)$$

where D' is the diffusion coefficient of the cement's crystals, ε is the exhibited porosity and τ accounts for the tortuosity of the interconnected porosity (11).
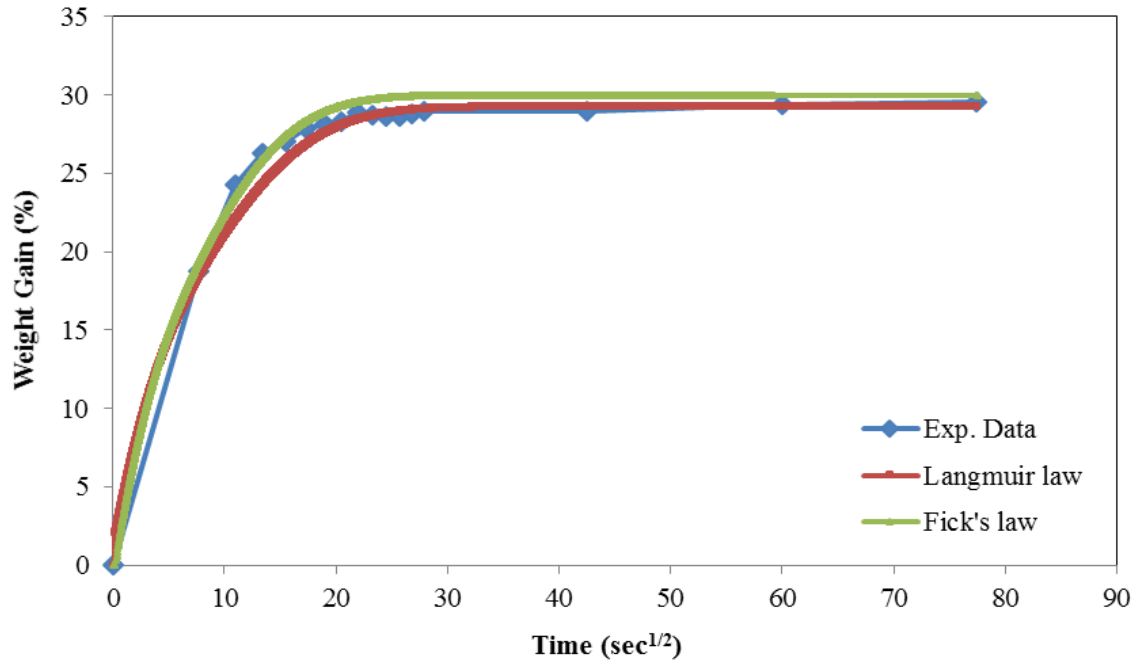
Fig. 6.3 : Experimental and simulation results of weight gain for a cylindrical specimen.

Afterwards, a simulation model was developed in Abaqus® simulation software package for the calculation of the induced hygro-strains, due to absorption phenomenon. An axisymmetric modeling was used and the area of interest was consisted of 12000 elements (Fig. 6.4). The optical sensor was also simulated, which was located in the longitudinal axis of the specimen. An exported file from the implemented Langmuir's diffusion model, was used as input file that included the simulation weight gain results, for each node and time increment. Moreover the values for the Elastic modulus (E) and Poisson's ratio (v) were given for the bone cement [(E,v)= (721 MPa, 0.28)] as well as for the optical sensor (glass): [(E,v)= (72 GPa, 0.30).
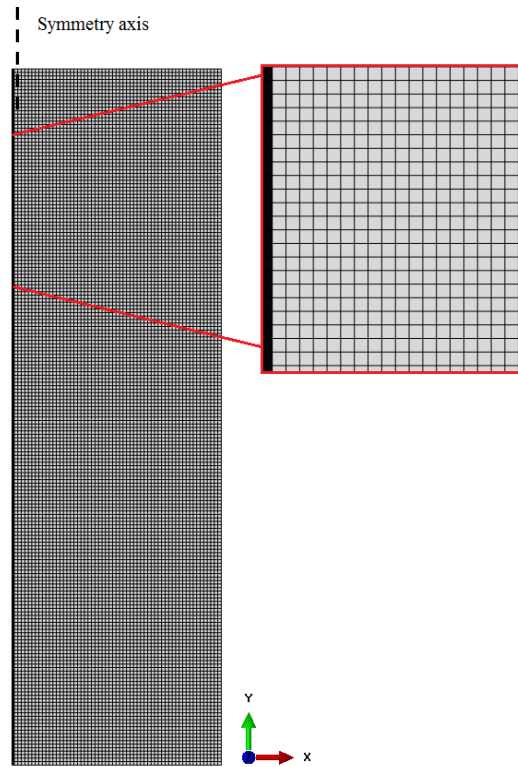
Fig. 6.4 : Implemented Finite Element axisymmetric model. The thick black elements on the left side, represent the optical sensor.

Then, the induced strains in each element were calculated through the following formula:

$$[\varepsilon] = \beta_{sim}[\Delta u] \tag{6.10}$$

where $[\varepsilon]$ is the matrix of calculated strains, resulted by multiplying weight gain change expressed in $[\Delta u]$ matrix, with a coefficient β_{sim}. As simulation hygro-strain results were considered the obtained strain values for all time increments, from the node that was located in the same position as the Bragg sensor in the used specimen (midst of the specimen's longitudinal axis). Several runs were conducted where various values were given to β_{sim} in order to achieve the optimum fitting of the simulation results with the experimental data (hygro-strains), obtained from the first run of the corresponding experiment (see section 4.4). Ultimately, for a value of β_{sim}= 5.32x10^{-6}/% w/w, the simulation results presented the best achieved convergence with the corresponding experimental results, as it can be observed in Fig. 6.5. It can be noted that for the first 2 minutes (0-12 sec$^{1/2}$) the simulation results almost coincide with the experimental results while for the rest time period a difference between them can be observed, that varies between ~1-16%.
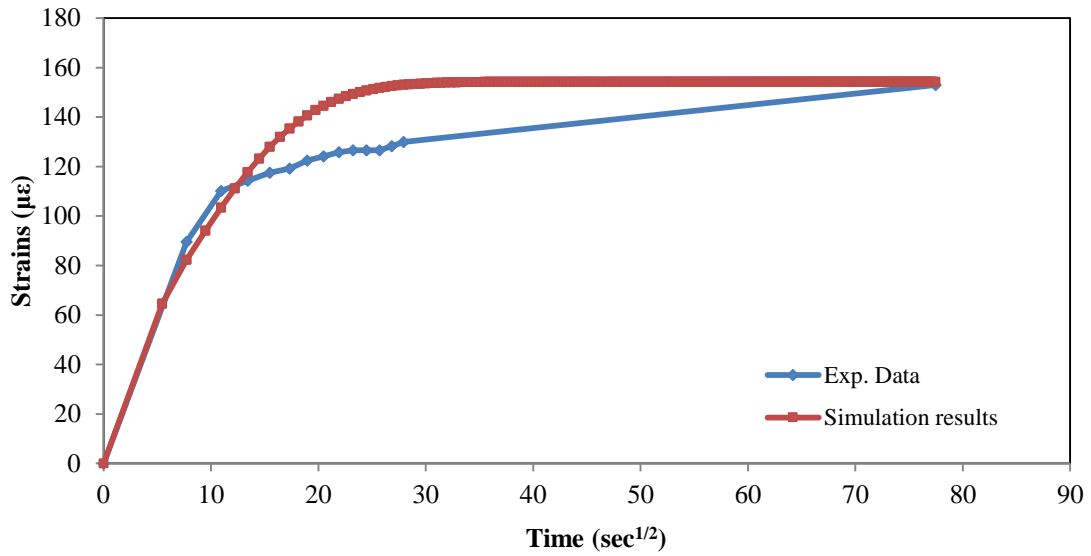
Fig. 6.5 : The obtained hygro-strains from the FEM analysis run, for $\beta=5.32 \times 10^{-6}/\%$ w/w, compared with the experimental data.

Although the β_{sim}, obtained from the simulations, is comparable with the one calculated from the experimental data in section 5.2.2.3.1 ($\beta_I=7.02 \times 10^{-6}/\%$ w/w), this above presented modeling of the diffusion phenomenon and the induced hygro-strains is considered a simplified approach of the corresponding phenomena for two main reasons. The first one has to do with the fact that material's exhibited porosity presents unique features (e.g. pores of various diameters, special interconnectivity, pores' dispersion etc.) as it is demonstrated in section 4.2, that influence the evolution of absorption phenomenon. However in our modeling it is only taken into account indirectly, by setting a high value in effective diffusivity coefficient (D_l). Secondly, in FEM model that simulated the developed hygro-strains, the porosity could not be taken into account. The only way to achieve it would be through a detailed CAD model that represents the exhibited porosity of the examined CPC, however such an attempt is very challenging and time consuming.

6.3 A case study of CPC medical application: Total Hip Replacement

6.3.1   Where Total Hip Replacement is implemented?

The human hip bone is one of the body's largest joints, considered as a ball-and-socket joint. The socket is formed by the acetabulum, which is part of the large pelvis bone, while the ball is the femoral head, which is the upper end of the femur (thighbone). The bone surfaces of the ball and socket are covered with articular cartilage, a smooth tissue that preserves and protects the ends of the bones and enables them to move easily. Also, a thin tissue called synovial membrane surrounds the hip joint. In a healthy hip, this membrane makes a small amount of fluid that lubricates the cartilage and ensures a frictionless hip movement (91).
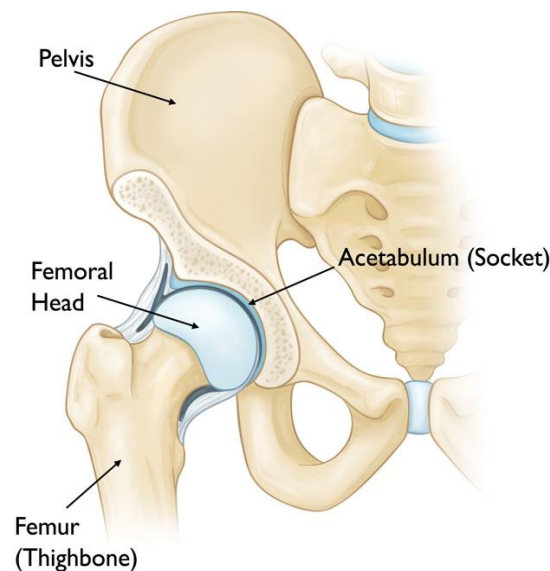
Fig. 6.6 : The anatomy of a human femur bone **(91)**.

One of the most common hip disease is arthritis, where the cartilage cushioning the bones of the hip, wears away. As a result, the bones rub against each other, causing hip pain and stiffness. In this case a Total Hip Replacement (THR) surgical procedure is necessary, in which the damaged femoral head is removed and replaced with a metal stem that is placed into the hollow center of the femur. The femoral stem may be either cemented or "press fit" into the bone. (Fig. 6.7). For the needs of this work, a cemented stem placed in a femoral bone will be investigated through a developed simulation, thoroughly presented in the next section. The main goal is to evaluate the mechanical performance of the bone cement in such application as well as to

discuss the developed stress fields and their patterns in the components of the whole configuration system.
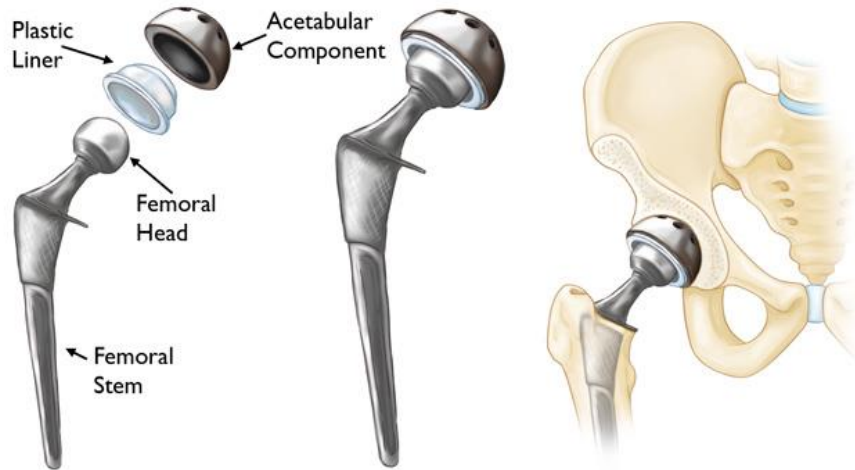
Fig. 6.7 : The individual components of a total hip replacement and how the implant fits into the hip **(91)**.

6.3.2 Modeling

- CAD models

Initially, a replicated model of a femur bone was created by 3-D scanning a femur sawbone. The resulting CAD file (Fig. 6.8) was consisted of small surfaces, stitched between them, which formed a closed shell-type model.
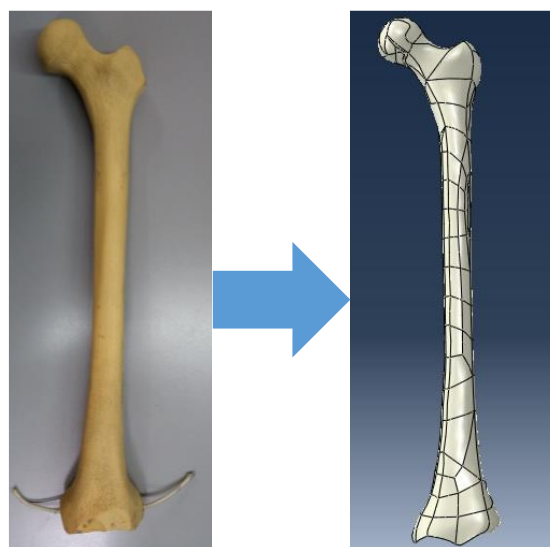
Fig. 6.8 : The 3-D scanned sawbone and the resulting CAD model.

Afterwards, the obtained CAD file was imported in Abaqus® simulation software package where a number of steps were followed, in order to create the final model that was used for the implemented simulation. Initially, as soon as the CAD model was imported in the simulation software, the shell-type geometry was converted into a solid 3-D model Then, the bottom part of the femur model was subtracted, since the area of interest concerns the upper half part of the femur bone, where the stem implant is placed. This consideration is also found in several studies, in which loading of a stem implant placed in a femur bone was also simulated [92], [93], [94], [95]. Subsequently, the femoral head was subtracted with a cut perpendicular to its basis, like the one performed in THR surgery. Also, a refinement of the model's external surfaces was conducted by merging the small surfaces, since the quality of the generated mesh is strongly depended on them. Afterwards, a cavity was created on the inside of the femur model in which the stem implant as well as a structure that will surround the stem implant and resemble the bone cement, will be placed in. The above-described are illustrated in Fig. 6.9.
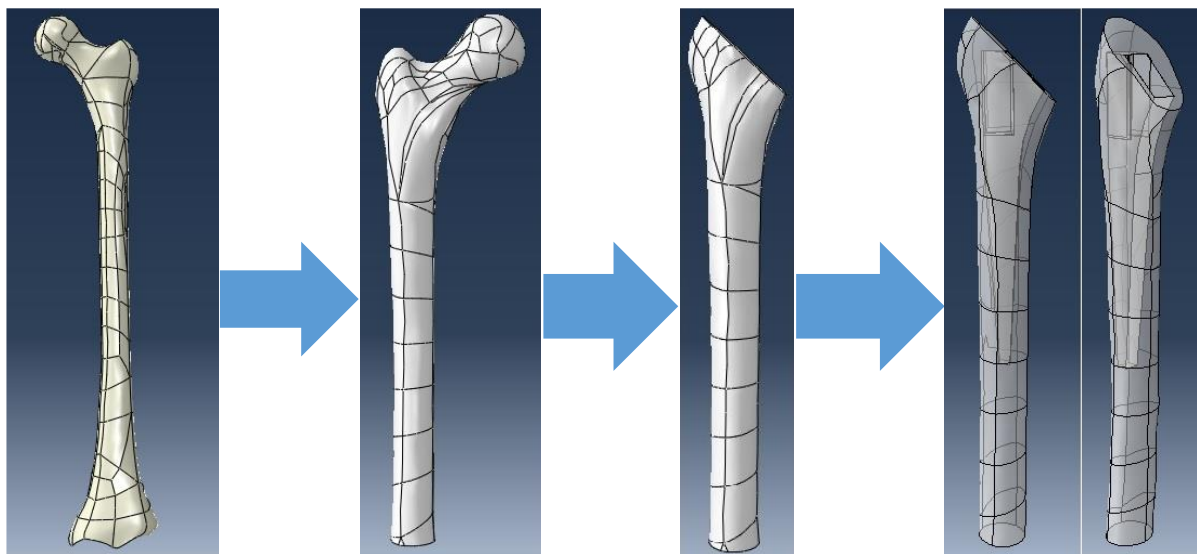
Fig. 6.9 : The processing of the femur bone CAD model.

In reality, the human femur bone is consisted of 2 different structures that exhibit different material properties: the trabecular (or cancellous/spongy) bone which is located on the inside of the femur bone, having a spongous structure, and the cortical bone on the outside that acts as a hull (Fig. 6.10). Thus, the femur bone CAD model was partitioned in 2 different structures: a "shell" of variable thickness along its longitudinal axis (1.8-3 mm) and the inner "core". This

way, a more realistic approach of the femur bone was also simulated, where the "shell" and the "core" resembles the cortical and spongy bone, respectively (Fig. 6.11).
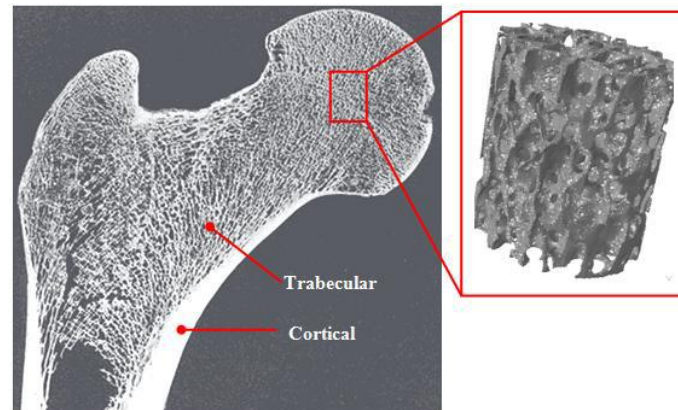
Fig. 6.10 : A human femur bone composed of the trabecular bone, in the inner side, and the cortical bone, on the outer side **(96)**.
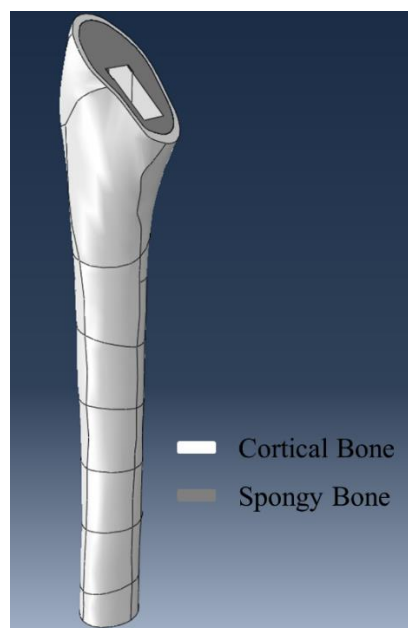
Fig. 6.11 : The final version of the femur bone CAD model.

A real stem implant was also 3-D scanned and a corresponding CAD model of a stem implant was obtained. However, the used simulation software did not allow the implementation of a load in a non-planar surface and as a result the femoral head was subtracted.
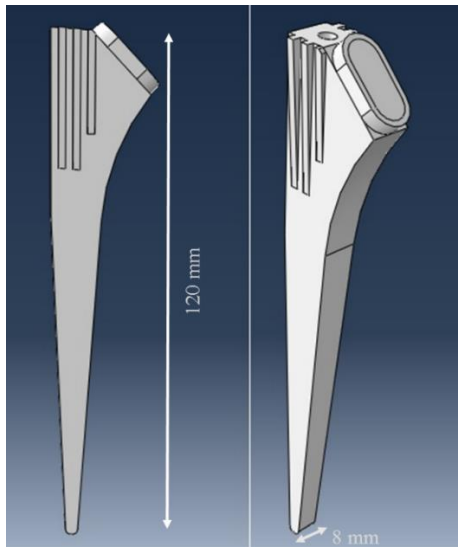
Fig. 6.12 : The CAD model of the stem implant.

Based on the CAD model of the stem implant, a new structure was created which surrounded the stem implant and simulated the bone cement. This was achieved through 3 steps: (I) creation of a main 3-D structure having a similar, simplified geometry as the one of the stem implant (Fig. 6.13a), (II) sufficiently increase its thickness (Fig. 6.13b) (III) subtraction of the volume that corresponds in the stem implant, which led to a cavity creation (Fig. 6.13c). The thickness varied between 1-3.5 mm, since in reality a small amount of bone cement is used in cemented THR.
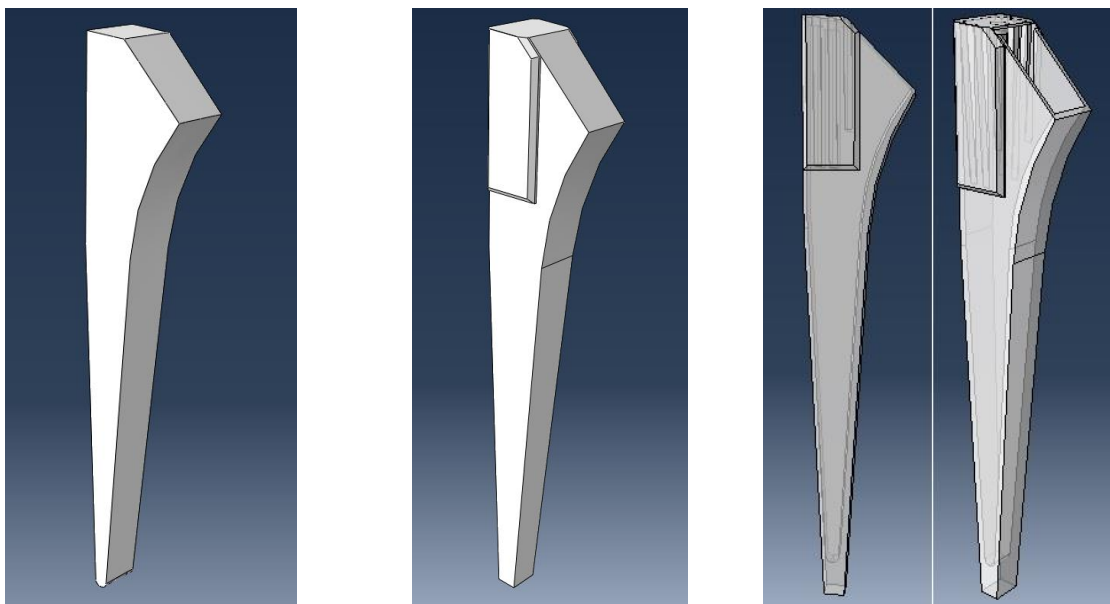
Fig. 6.13a-c: Three implemented stages from which the model of bone cement came from.

- Material properties

Afterwards, the material properties were given for each part instance. Specifically the stem implant was considered to be made of titanium, hence Young modulus E=110 GPa and Poison's ratio v =0.3 was assigned (93). For the bone cement, 2 different runs were implemented where in the first as Young modulus was assigned the one obtained from low-load indentation tests (E=721 MPa), while in the second was assigned the Young modulus obtained from compression tests (E= 1.7 GPa). Bone cement's Poisson's ratio was set to v =0.28 (97). As far it concerns the femur bone model, linear transverse isotropic properties that apply for a cortical bone were assigned to the cortical bone model version: E_{xx}=11.5 GPa / G_{xx}=11.5 GPa / v =0.31, E_{yy}=11.5 GPa / G_{yy}=11.5 GPa / v =0.31, E_{zz}=17 GPa / G_{zz}=11.5 GPa / v =0.31 (98), (99). For the spongy bone, its Young Modulus and Poisson's ratio was respectively set to: E=2.13 GPa, v =0.3 (93). A summary of the assigned material properties can be found in Table 6.1.

Material	Plane	Young modulus, E (GPa)	Shear modulus, G (GPa)	Poisson ratio, v
Cortical bone	xx	11.5	3.6	0.31
	yy	11.5	3.3	0.31
	zz	17	3.3	0.31
Spongy bone	-	2.13	-	0.3
Bone cement	-	0.72 / 1.7	-	0.28
Stem implant	-	110	-	0.3

Table 6.1: Assigned material properties in the components of the model.

- Generated mesh

10-node quadratic tetrahedron type elements (C3D10) were used in order to mesh all the femur component models, which is suggested for 3-D stress simulations. A total number of 828588 elements was generated for all meshed models, which was considered enough in order to avoid the generation of distorted elements, either in shape or size that would have an impact in the results. A mesh refinement was also implemented in the areas where the geometry was more complicated as well as in the surfaces in which a friction model was assigned. Afterwards, the meshed models were suitably assembled, as Fig. 6.14 illustrates.

- Initial and boundary conditions

Although the simulated loading conditions can differ, depending on the examined case, in general similar load values are used in order to simulate a femur bone's loading. In this study, two distributed loads were implemented that correspond in static loading conditions of a 70 kg weight average person (98), (99). Specifically, a distributed load of 1946 N/cm^2 was assigned in the planar surface of the stem implant's upper part, in a 20^0 angle in reference to femur bone's longitudinal axis, which corresponds to a 3 kN point load. Moreover a distributed load of ~317 N/cm^2 was also assigned at the lateral side of the femur bone, in the same orientation as of the stem load, being equivalent to a 1.25 kN point load. This load simulated the abductor muscle load, which partially reliefs the femur bone from the loads it is subjected. Also in the bottom of the model, a 3-axis displacement limitation was set.

Between the external surfaces of the stem and bone cement model, a Coulomb friction model was chosen having a friction coefficient value 0.3 (93) while between the bone cement and the femur bone a friction coefficient value of 0.5 was set. Moreover, the cortical and spongy bone were tied between them.
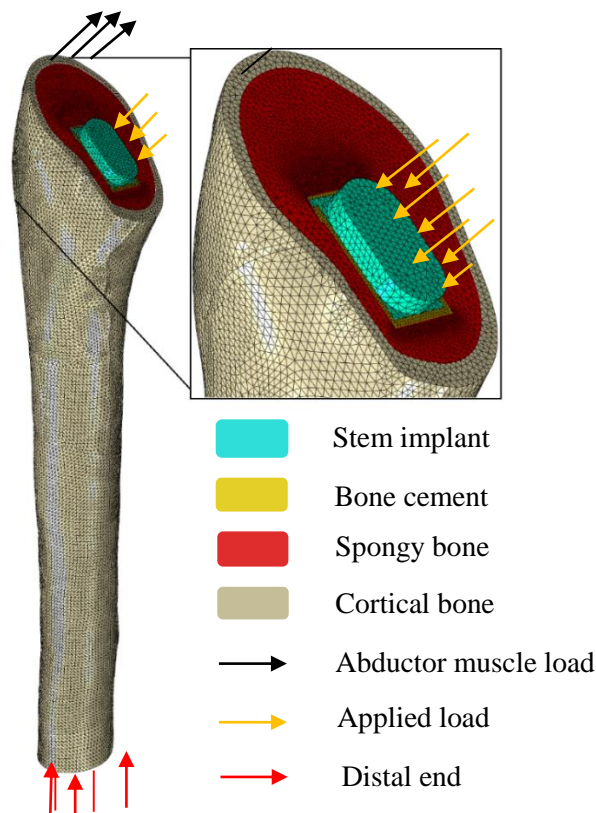
Fig. 6.14: The assembled meshed models and the implemented initial/boundary conditions.

6.3.3 Results

The stress field, obtained from the analysis run, which concerns the stem implant is presented in Fig. 6.15. As one can observe the developed stresses range between ~0.1 and ~250 MPa, where the high stress values are located around the edges of the backside (~180 MPa) and foreside (~250 MPa). The low stress values, observed in Fig. 6.16a for a higher accuracy stress scale, are exhibited around the neck of the stem (1-20 MPa) and are increased to ~30 MPa, along a zone between posterior and anterior side of the stem. A node-defined path was set at the backside of the stem implant, indicated with a red line, and the corresponding stress graph (Fig. 6.16b), according to maximum principle stress, was plotted as a function of the stem's posterior length. Oshkour et al. (93), also conducted a FEM simulation on a cemented femur stem implant and among other results a similar stress graph is also presented (Fig. 6.16c). In this graph, if the part of the first ~50 mm of prosthesis length is ignored since in the referred study the head of the femoral implant was included, it can be observed that it is very comparable with the one of this work not only in terms of stress value interval but also in the exhibited stress magnitudes for the same prosthesis lengths.
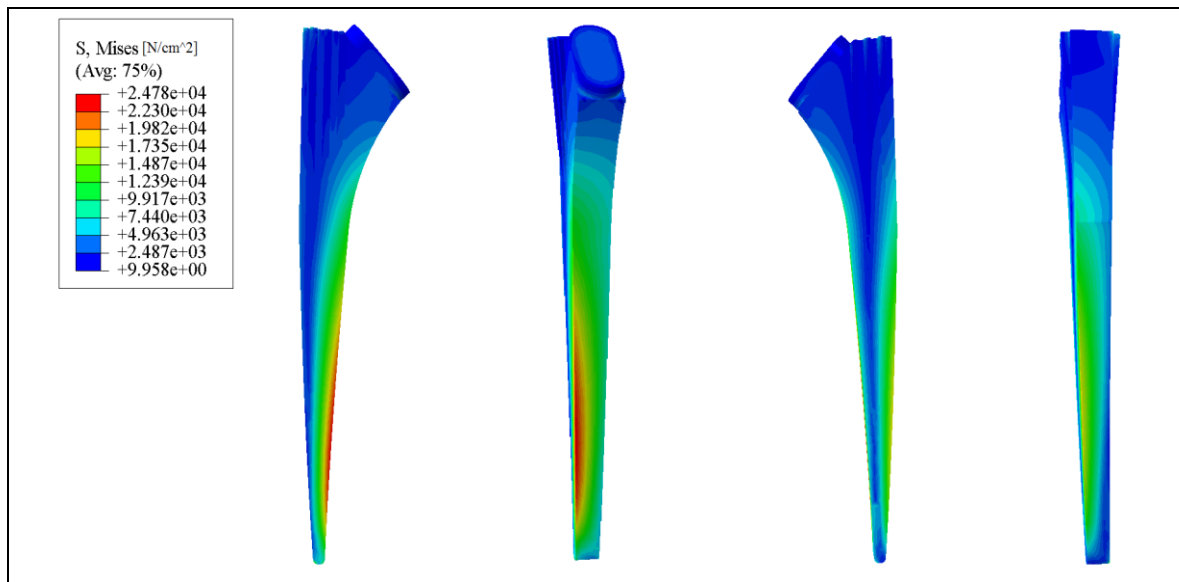
Fig. 6.15 : The stress field in the stem implant obtained from FE Analysis.
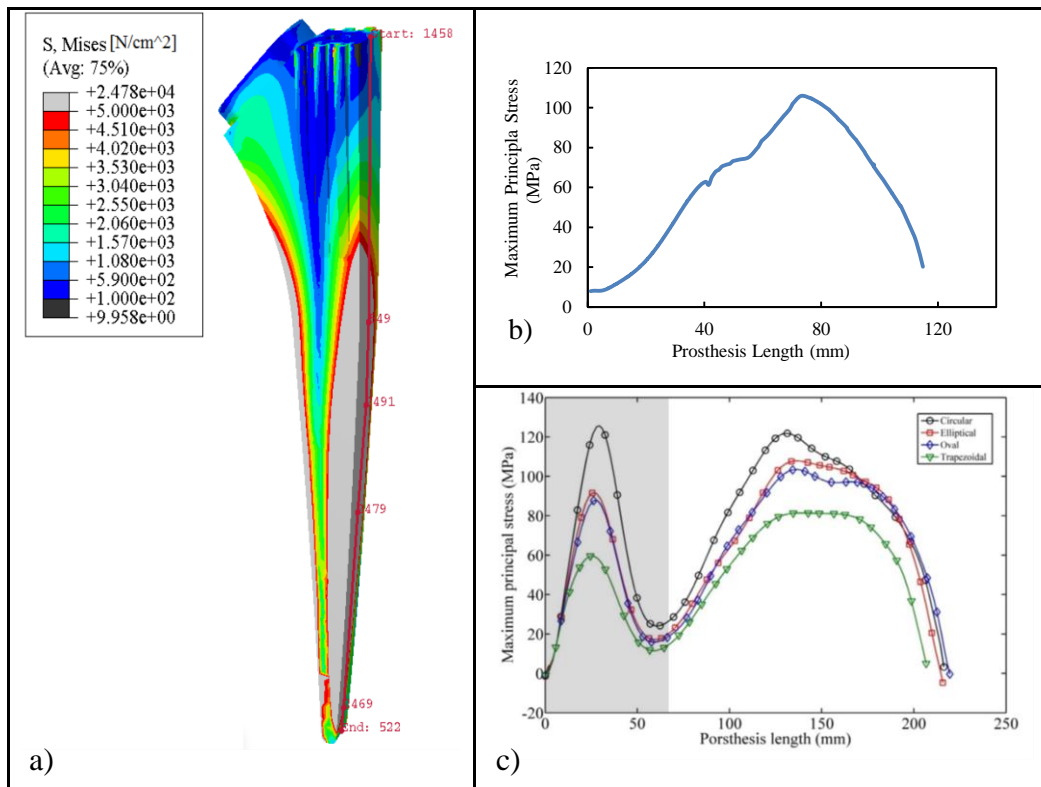
Fig. 6.16 : (a) The stress field in the stem implant for a higher accuracy stress scale and the node-defined path at the femur's backside (b) the resulting stress graph from the defined path (c) a similar graph obtained from **(93)**.

Passing to the bone cement, the exhibited stress field is presented in Fig. 6.17 for the case its Young modulus was assigned to 721 MPa. The stress magnitudes are very low and do not exceed 10 MPa, except for a region in the lower part, represented with grey color, in which stress values reach up to ~45 MPa. A free-body cut was performed in the midst of the specimen, perpendicular to the longitudinal axis, and its projection in the cut plane, towards the inner sider, can be found in Fig. 6.18a. As one can observe in the bottom of the cavity, where the bottom part of the stem relies to, stress values have the same high magnitude (45 MPa). For the analysis run where the Young modulus was set to 1.7 GPa instead of 721 MPa, the results are presented in Fig. 6.17b. As it can be observed relatively higher stress values are exhibited, for the same regions, yet they do not exceed 10 MPa. Moreover, higher maximum stress magnitudes are exhibited (~87 MPa instead of 45 MPa), located in the same area as in the previous case.
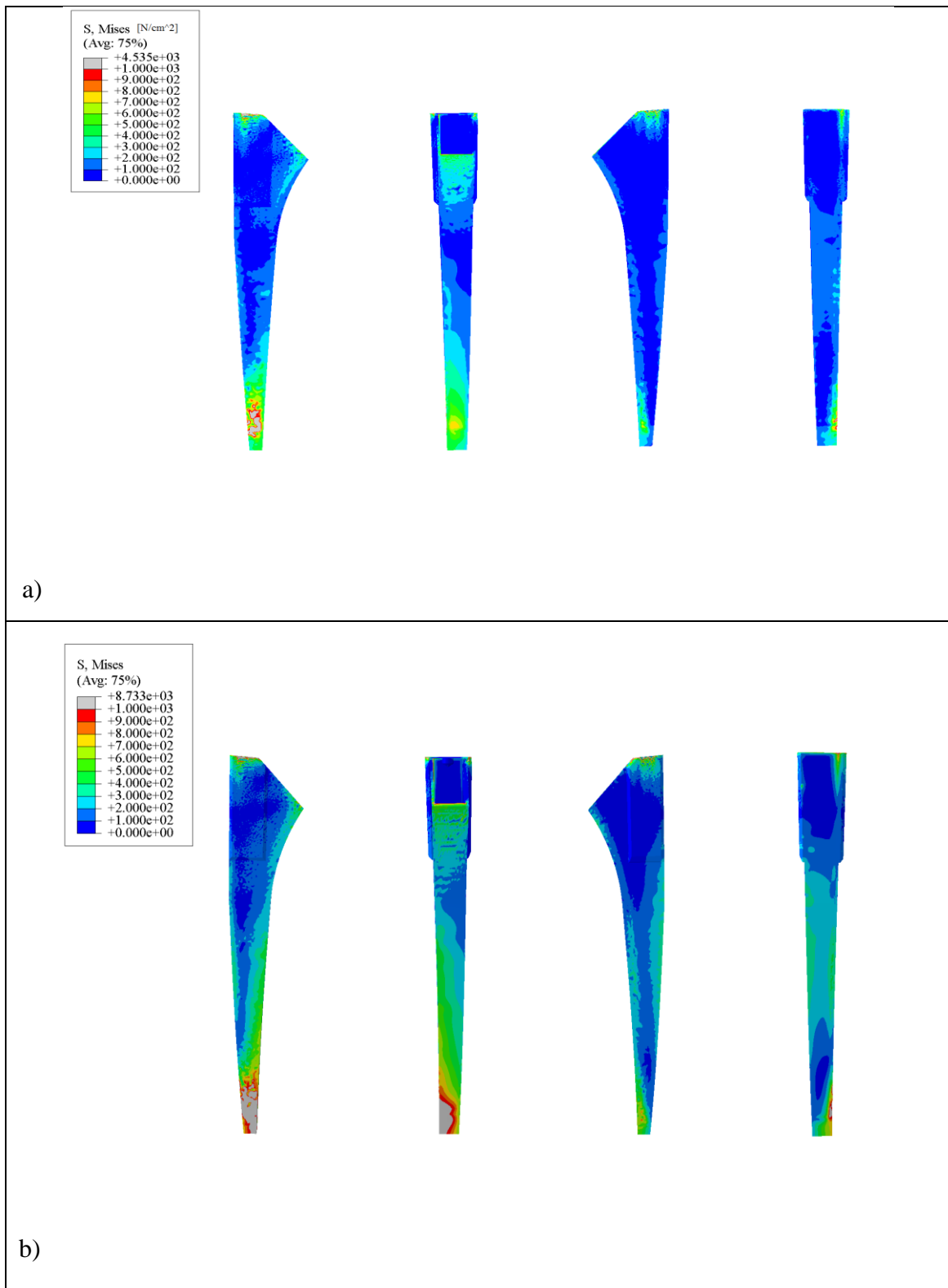
Fig. 6.17 : The stress field in the bone cement obtained from FE Analysis, for 2 different Young modulus values: (a) 721 MPa (b) 1.7 GPa.
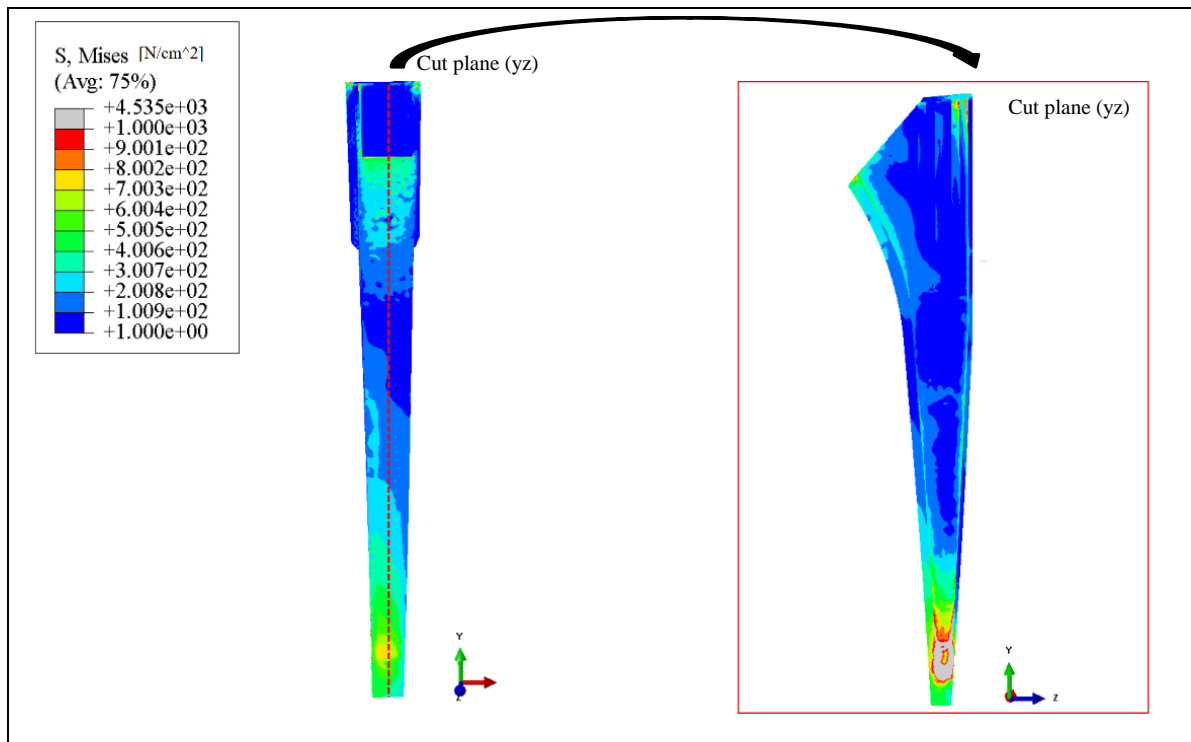
Fig. 6.18 : A free-body cut (dashed line) in the midst of the specimen, perpendicular to the longitudinal axis, and its projection to the cut plane towards the bone cement's inner side.

The exhibited stress field in the spongy bone, for the case where bone cement's Young modulus was set to 721 MPa, is presented in Fig. 6.19. The majority of the exhibited stress values range between 1 and ~40 MPa while in some areas are too low (<0.1 MPa). However, the corresponding node(s) in this area were successfully tied to the cortical bone and consequently higher stresses were obtained. It can be also observed that the exhibited stress values are lower for the part area where the femoral head is located and are progressively increased towards bottom. The same loading scenario was ran again but this time the Young modulus of the bone cement was set to 1.7 GPa. Interestingly, similar stress fields were obtained and little changes were observed, when compared with the previous results.

In Fig. 6.20 the stress field of the cortical bone, for a bone cement's Young modulus equal to 721 MPa, is presented. Its mechanical response due to stem's loading is similar to the one exhibited from the metallic implant: in the area around the femoral head the exhibited stress values range between ~1-40 MPa, as well as in a narrow zone between backside and foreside of the cortical bone. Stresses above 40 MPa are exhibited on the rest part of the cortical bone

while the highest stress values (~120 MPa) are located in the foreside of the lower part of the model, like in the case of the spongy bone.
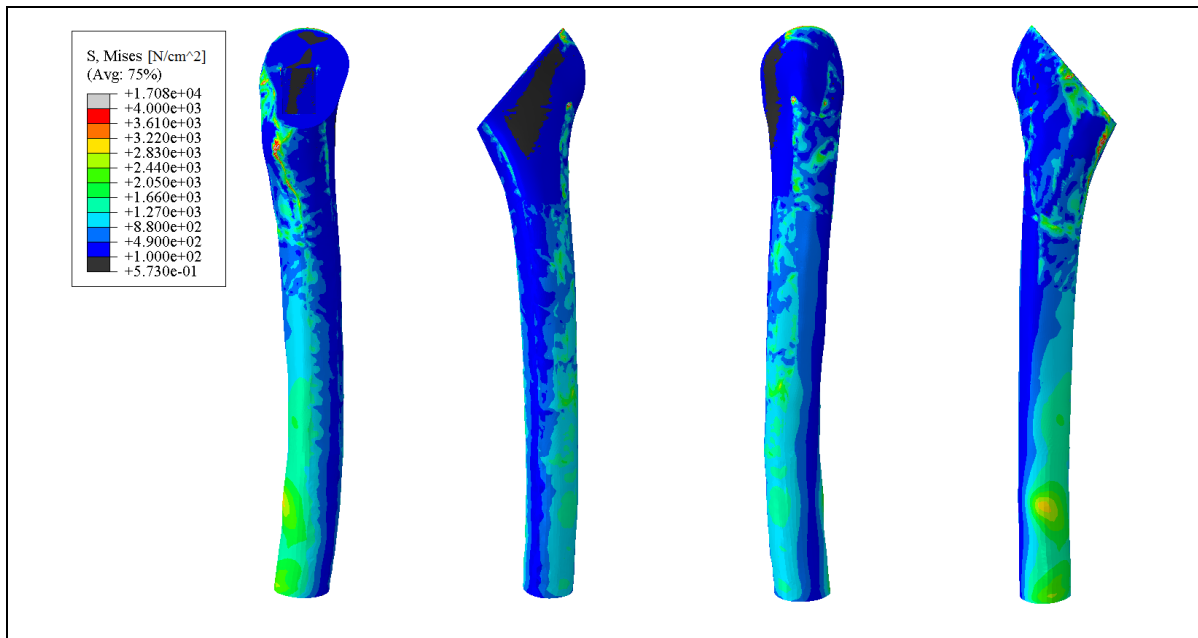
Fig. 6.19 : The stress field in the cancellous (spongy) bone obtained from FE Analysis.

In a local area, indicated with yellow, vivid red and grey color, stress values exceed that limit due to the fact that the thickness of the cortical bone in this region is too thin (>0.5 mm), compared to the thickness of a real human femur bone. As a result, they should not be taken into account. Moreover the obtained results, using a higher value in bone cement's Young modulus (1.7 GPa instead of 721 MPa) are very similar with the above presented and almost no differences can be found.

From the above presented stress distributions, it can be noted that the highest stress values are exhibited from the stem implant (~150-250 MPa), which is reasonable due to its high Young modulus, located on the posterior and anterior side of the implant. The same behavior can be also observed in the spongy and cortical bone, in which the higher stress magnitudes are exhibited also on the posterior and anterior side of their main body. Also, the bone cement and the spongy bone have a similar stress value range: (1-40 MPa) in the case where bone cement's Young modulus is 721 MPa, while for a higher Young modulus value (1.7 GPa) the maximum stress values exhibited in the bone cement are increased to ~85 MPa. However, a different stress distribution is exhibited between them: in the bone cement the stress magnitudes are

between 0-1 MPa and are greatly increased in the cavity's bottom region, while in the spongy bone the stress distribution is more uniform.

Conclusively, it can be stated that the load with which is subjected the stem implant is transferred to the cortical bone and also to the spongy bone, to a less degree, in the posterior and anterior side of their main body, while in the regions around femoral head low magnitude stress values are developed. Moreover, their mechanical response do not seem to be significantly affected by a change of bone cement's Young modulus from 721 MPa to 1.7 GPa. As far it concerns the bone cement it appears to be subjected in low magnitude stresses, except the region of the bottom's cavity where the last part of the stem implant relies to. It is worth mentioning that in a similar experimental work for an acrylic bone cement (PMMA) (100), the same area of the bone cement was mostly found to fail after several load cycles. Thus, this particular area should be considered of high importance for any future studies that will investigate the failure mechanisms in a cemented THR.
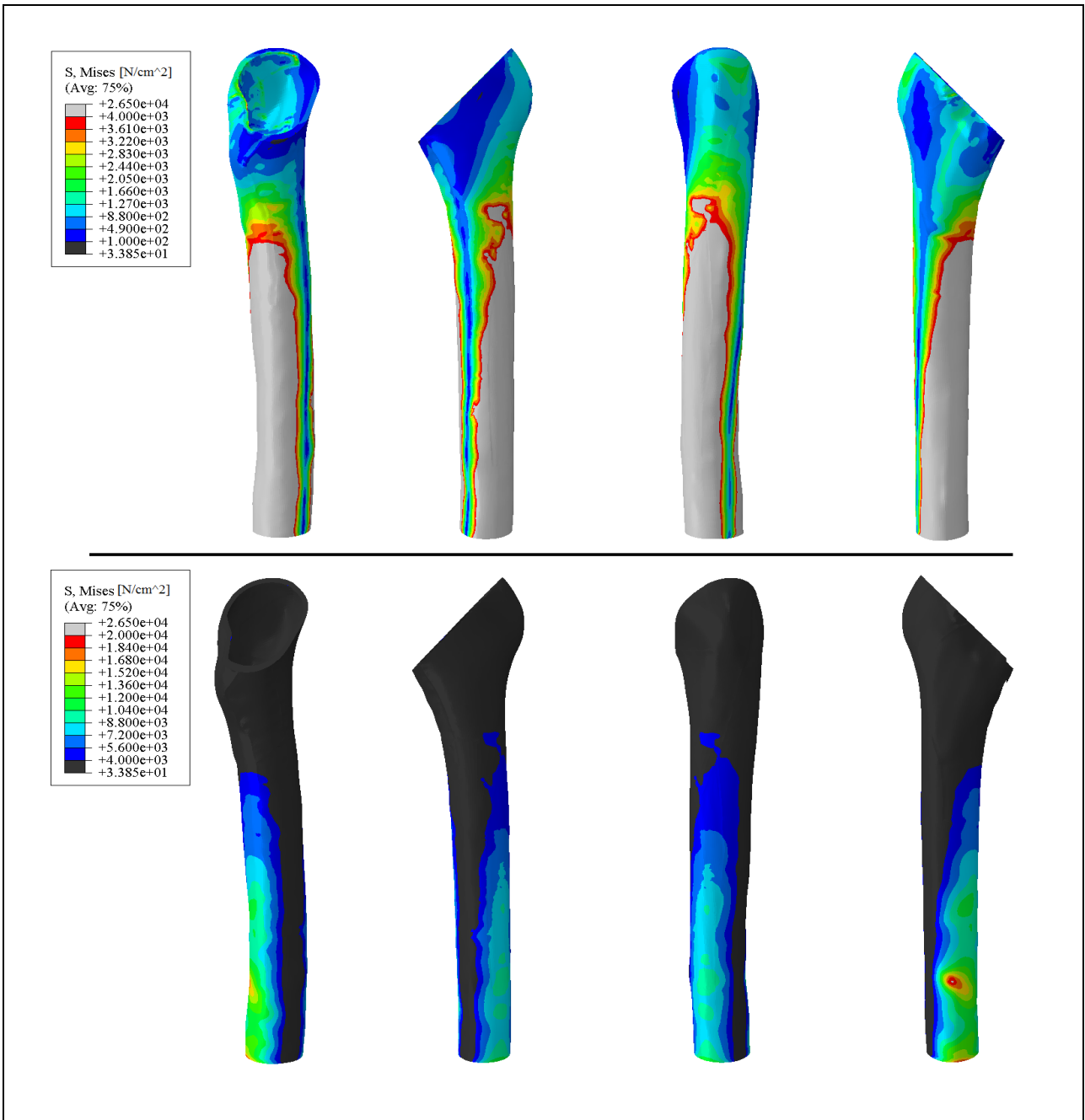
Fig. 6.20 : The stress field in the cortical bone obtained from FE Analysis.

Chapter 7

Conclusions and future work

7.1 Conclusions

In this thesis a thorough mechanical characterization on a self-setting apatitic cement, fabricated from pure α-TCP powder, is conducted and driven by the following sections:

- FBG-based strain investigation before, during and after material's hardening stage
- Investigation of material microstructure during hardening period
- Material's mechanical testing
- Evaluation of the material's exhibited porosity
- Material's absorbability in wet environment

Additionally, simulation models were also implemented for the absorption phenomenon and the resulted hygroscopic strains, during material's submerge in wet environment, as well as for a potential use of a CPC in a medical application. From the results, reported in Chapters 4-6, the following conclusions can be drawn:

- A FBG-based strain investigation of the examined biocement before, during and after hardening was successfully conducted while from the reported results interesting conclusions, presented below, are drawn. Up to the author's knowledge no such studies exist in the literature.

- After solidification stage, the calculated strain values are low. Moreover, no significant deviations were exhibited in strain magnitudes, obtained from different locations of the investigated specimen, suggesting a homogeneous strain field.

- Needle-like and plate-like crystal structures are developed in the investigated biocement, during hardening period, which is in accordance with the literature. Upon the end of hardening stage, a dense, entangled network of crystals is created.

- The obtained strain readings during hardening stage are also of low magnitude, thus the material retains its structural stability in liquid environment. Such finding is valuable since this kind of material are meant to be used in wet environment like human body. An also significant conclusion is that the linear patterns of the recorded hardening strains, are attributed in the two different phases of crystal structures' development (growth, entanglement).

- The fact that crystal structures are responsible for the enhancement of the hardended biocement's mechanical performance, necessitate the investigation of the crystal's dispersion throughout the material since their distribution may has an impact on how the material fails under loading. In this work the dispersion is characterized by uniformity. It is stressed out that the implemented method for the investigation of the crystals' distribution (μ-CT imaging), can be also useful in studies where the dispersion of crystals is modified with the addition of additives in the calcium phosphate powder.

- Material's compressive strength and Young modulus is considerably increased during hardening stage, due to crystals' development. Although the Young modulus obtained from compression and low-load indentation tests considerably differ, this is justified from the fact that the latter applies only during the early stages of loading.

- A Mohr-Coulomb failure criterion is proposed for the examined hardened biocement, based on the obtained results from compression and indirect compression test. However, the conduction of more tests is suggested that would further contribute to obtain cohesion (c) and internal friction angle (φ) values with higher accuracy.

- The hardened material exhibits an intrinsic porosity while pores' size vary within the order of magnitude of few microns. In the material's porosity are also included cavities, created due to air entrapment during paste casting in the moulds.

- The investigated bone cement, after its hardening, uptakes a significant amount of liquid within a short time period upon its submerge in liquid environment. The volume of the absorbed liquid coincides with the total volume of the material's pores, suggesting the following: (a) an interconnectivity of the pores (b) in this time period diffusion can be considered negligible.

- The measured hygroscopic strains, during material's re-immersion in wet environment, exhibit the same behavior as the specimen's liquid uptake, hence the absorption process can be monitored in an effective way with the use of a FBG sensor. Such potential can be exploited in cases where CPCs are also used as drug eluting carriers and monitoring of drug loading or release is essential.

- Two simplified simulation models are implemented, concerning the absorption phenomenon and the resulted hygroscopic strains, upon material's submerge in liquid environment. Through the proposed absorption simulation the experimental results of weight gain can be reproduced for a cylindrical specimen, by setting suitable values in the unknown parameters of the implemented diffusion model, while the resulted hygroscopic strains can be approached by assigning a suitable value in β parameter (material's coefficient of moisture expansion - CME).

- A 3-D simulation model, based on a potential real-life application of calcium phosphate cement in Total Hip Replacement, is implemented and proposed. Through this model the distribution of the developed strain fields can be obtained, not only in the bone cement but also in the femur bone as well as in the stem implant. From the obtained results of a static analysis run, it can be concluded that the highest stress values in femur bone and stem implant structures are exhibited in the anterior and posterior side of the same longitudinal area (midst of femur bones' upper part). In bone cement structure the highest stress values are exhibited in the bottom of the cavity, where the lower part of the stem relies to. Hence, this region should be considered of high importance as it appears to determine the mechanical strength a bone cement should exhibit in order to successfully sustain the simulated loading conditions.

7.2 Future work

Through the conduction of this work a number of proposals can be made and suggested as future work, to further enrich the mechanical investigation on self-setting calcium phosphate bone cements:

I) *Incorporation of geopolymers in calcium phosphate cements*

Geopolymers have been proven to be non-toxic and eco-friendly materials. Their potential use in calcium phosphate bone cements would be very interesting, both in a scientific and a medical point of view. Hence, several experiments which will investigate if and in which degree the addition of geopolymers in CPCs have a positive impact on the material's mechanical properties and performance, are strongly suggested.

II) *Investigation of TCP powders with different characteristics (granulometry, stoichiometry, sample volume etc.) and variable curing conditions (pH, hardening solution etc)*

In this work it was demonstrated that the mechanical performance of hardened self-setting calcium phosphate bone cements is strongly dependent on the developed crystal structures, during hardening stage. However those crystals are actually products of a chemical reaction (hydrolysis), which can be affected by several parameters such as grains size, pH of hardening liquid, temperature of the surrounding environment etc. As a result, a parametric study in which these parameters will be investigated and determined in order to achieve the optimum mechanical properties in a hardened CPC, is considered of high value. Although several works have been conducted which investigate some of these parameters, no systematic study exists in the literature.

III) *Conduction of more experiments (i.e biaxial testing, pure shear tests) through which the mechanical performance of CPCs will be further researched.*

As it was noted, the mechanical strength of the examined CPC in tensile stress, obtained from diametral compression testing, was ~7 times lower that the exhibited mechanical strength in compression stress. Consequently, the failure of CPCs may be dominated from their strength

in tensile stresses and not in compressive stresses. The investigation of such allegation becomes more important considering that the developed stress fields in potential applications of CPCs, like Total Hip Replacement, are complex and include tensile stresses. Moreover, such information would provide more precise information to better assess the Mohr-Coulomb failure criterion, though which CPC mechanical performance in shear stresses can be evaluated.

IV)   *Further investigation on the exhibited ability of FBGs to sense the development of microstructural changes during hardening period.*

The finding that the linear patterns of the recorded hardening strains are correlated with the development of crystal structures is considered of high value. However the crystals development rate is affected not only from temperature changes but also by several other parameters (pH, grain size etc.), which in this study were not controlled. Hence, deviations may were introduced in strain readings. For this reason, the conduction of more experiments that concern FBG-based strain investigation during hardening period are suggested, in which any parameter that influence the α-TCP hydrolysis rate will be controlled.

Bibliography

1. Ancient Origins. [Online] [Cited: 11 28, 2016.] http://www.ancient-origins.net/news-history-archaeology/archaeologists-discover-2300-year-old-dental-implant-iron-age-burial.

2. Wikipedia. [Online] [Cited: 12 04, 2016.] https://en.wikipedia.org/wiki/Biomaterial.

3. F. H. Silver, Ch. Doillon. *Biocompatibility—interactions of biological and implantable materials.* New York : VCH Publisher Inc., 1989.

4. *Bone cement.* R. Vaishya, M. Chauhan, A. Vaish. 2013, Journal of Clinical Orthopaedics and Trauma, Vol. 4, pp. 157–163.

5. Clive, L. The Mechanical Properties of PMMA Bone Cement. *The Well-Cemented Total Hip Arthroplasty.* Berlin Heidelberg : Springer, 2005, pp. 60-66.

6. *Review: Calcium Phosphate Cements (CPCs) for bone substitution: chemistry,handling and mechanical properties.* J. Zhang, W. Liu, V. Schnitzler, F. Tancret, J.M.Bouler. 2013, Acta Biomaterialia, Vol. 10, pp. 1035-1049.

7. *Local and Systemic Effects of Unpolymerised Monomers.* S.S. Gosavi, S.Y. Gosavi, R.K. Alla. 2010, Dental Research Journal, Vol. 7, pp. 82-87.

8. International, ASM. *Characterization and failure analysis of plastics.* Ohio : ASM International, 2003.

9. Poitout, D.G. *Biomechanics and Biomaterials in Orthopedics.* London : Springer, 2004.

10. *Calcium phosphate ceramic systems in growth factor and drug delivery for bone tissue engineering: A review.* S. Bose, S. Tarafder. 2012, Acta Biomaterialia, Vol. 8, pp. 401-421.

11. *Calcium phosphate cements as bone drug delivery systems: A review.* M.P. Ginebra, T. Traykova, J.A. Planell. 2006, Journal of Controlled Release, Vol. 113, pp. 102-110.

12. *Calcium Phosphate Bone Cements.* S. M. Barinov, V. S. Komlev. 2011, Inorganic Materials, Vol. 47, pp. 1470–1485.

13. *Biphasic calcium phosphate bioceramics: preparation, properties and applications.* R. Z. LeGeros, S. LinR. Rohanizadeh, D. Mijares, J. P. LeGeros. 2003, Journal of Materials Science: Materials in Medicine, Vol. 14, pp. 201–209.

14. *Preparation and characterization of bioceramics produced from.* O. Andriotis, O. L. Katsamenis, D. E. Mouzakis, and N. Bouropoulos. 3, 2010, Crystal Research Technology, Vol. 45, pp. 239-243.

15. *Calorimetry investigations of milled a-tricalcium phosphate (a-TCP) powders to determine the formation enthalpies of a-TCP and X-ray amorphous tricalcium phosphate.* K. Hurle, J. Neubauer, M. Bohner, N. Doebelin, F. Goetz-Neunhoeffer. 2015, Acta Biomaterialia, Vol. 23, pp. 338–346.

16. *Calcium phosphate cements as drug delivery materials.* M.P. Ginebra, C. Canal, M. Espanol, D.Pastorino, E.B. Montufar. 2012, Acta Biomaterialia, Vol. 64, pp. 1090-1110.

17. *Bioceramics of calcium orthophosphates.* Dorozhkin, S.V. 2010, Biomaterials, Vol. 31, pp. 1465–1485.

18. *Injectability of calcium phosphate pastes.* M. Bohner, G. Baroud. 2005, Biomaterialia, Vol. 26, pp. 1553-1563.

19. *Mehcanicsms underlying the limited injectability of hydraulic calcium phosphate cement.* M. Habib, G. Baroud, F. Gitzhofer, M. Bohner. 2008, Acta Biomaterialia, Vol. 4, pp. 1465-1471.

20. *Addition of cohesion promoter to calciun phosphate cements.* I. Khairoun, F. Driessens, M.G. Boltong, J.A. Planell, R. Wenz. 1999, Biomaterialia, Vol. 20, pp. 393-398.

21. S. Sakka, J. Bouaziz, F.B. Ayed. Mehcanical properties of Biomaterials Based on Calcium Phosphates and Bioinert Oxides for Application in Biomedicine. *Advances in Biomaterials Science and Biomedical Applications.* 2013.

22. *Effects of hudroxypropyl methycellulose and other gelling agents on the handling properties of calcium phosphate cement .* A. Cheng, S. Takagi, L.C Chow. 1997, Journal of Biomedical Material Research, Vol. 35, pp. 273-277.

23. *The influence of different cellulose ethers on both the handling and mechanical properties of calcium phosphate cements for bone substitution.* W. Liu, J. Zhang, P. Weiss, F. Tancret, J.M. Bouler. 2013, Acta Biomaterialia, Vol. 9, pp. 5740-5750.

24. *Study of the reactivity and in vitro bioactivity of Sr-substituted α-TCP cements.* S. J. Saint-Jean, C.L. Camire, P. Nevsten, S. Hansen, M.P. Ginebra. 2005, Journal of Material Science: Materials in Medicines, Vol. 16, pp. 993-1001.

25. *Injectable and rapid-setting calcium phosphate bone cement with dicalcium phosphate dehydrate.* E.F Burguera, H. Xu, M.D Weir. 2006, Journal of Biomedical Material Research, Vol. 77B, pp. 126-134.

26. *High-strength resorbable brushite bone cement with controlled drug-releasing capabilities.* M. P. Hofmann, A.R Mohammed, Y. Perrie, U. Gbureck, J.E Barralet. 2009, Acta Biomaterialia, Vol. 5, pp. 43-49.

27. *Setting reaction and hardening of an Apatitic Calcium Phosphate Cement.* M.P. Ginebra, E. Fernández, E.A De Maeyer, R.M. Verbeeck, M.G. Boltong, J.Ginebra , F.C Driessens. 1997, Journal of Dental Research, Vol. 76, pp. 905-912.

28. A.H Burstein, D.T Reilly, V.H Frankel. Failure Characteristics of Bone and Bone Tissue. *Perspectives in Biomedical Engineering.* s.l. : Palgrave Macmillan UK, 1972, pp. 131-134.

29. *Mechanical characterization of brushite and hydroxyapatite cements.* E. Charriere, S. Terrazzoni, C. Pittet, P. Mordasini, M. Dutoit, J. Lemaitre, Ph. Zysset. 2001, Biomaterials, Vol. 22, p. 2937}2945.

30. *Processing and mechanical properties of hydroxyapatite pieces obtained by the gelcasting method.* S. Padilla, M. Vallet-Regi, M. P. Ginebra b, F. J. Gil. 2005, Journal of the European Ceramic Society, Vol. 25, pp. 375–383.

31. *Amorphous calcium phosphates: Synthesis, properties and uses in biomaterials.* C. Combes, C. Rey. 2010, Acta Biomaterialia, Vol. 6, pp. 3362–3378.

32. *Fabrication and mechanical properties of calcium phosphate cements (CPC).* J.T. Zhang, F. Tancret, J.M. Bouler, J.T. Zhang, F. Tancret, J.M. Bouler. 2011, Materials Science and Engineering C, Vol. 31, pp. 740–747.

33. *Self-hardening calcium deficient hydroxyapatite/gelatine foams.* E. B. Montufar, T. Traykova, E. Schacht, L. Ambrosio, M. Santin, J. A. Planell, M. P. Ginebra. 2010, Journal of Materials Science: Materials in Medicine, Vol. 21, pp. 863-869.

34. *Bioactive calcium sulfate/magnesium phosphate cement for bone.* G. Yang, J. Liu, F. Li, Z. Pan, X. Ni, Y. Shen, H. Xu, Q. Huang. 2014, Materials Science and Engineering C, Vol. 35, pp. 70-76.

35. *Influence of porosity on the mechanical resistance of hydroxyapatite ceramics under compressive stress.* J.C Le Huec, T. Schaeverbeke, D. Clement, J. Faber, A. Le Rebeller. 1995, Biomaterials, Vol. 16, pp. 113-118.

36. *Surface modifications of hydroxyapatite ceramics in aqueous media.* S. Amrah-Bouali, C. Rey, A. Lebugle, D. Bernache. 1995, Biomaterials, Vol. 15, pp. 269-272.

37. *Technological issues for the development of more efficient calcium.* M. Bohner, U. Gbureck, J.E. Barralet. 2005, Biomaterials, Vol. 26, pp. 6423-6429.

38. *Evaluation of the ultrasonication process for injectability of hydraulic calcium phosphate pastes.* M. Habib, G. Baroud, L. Galea, M. Bohner. 2012, Acta Biomaterialia, Vol. 8, pp. 1164-1168.

39. *Influence of anti-washout agents on the rheological properties and injectability of a calcium phosphate cement.* X.P. Wang, L. Chen, H. Xiang, J.D. Ye. 2007, Journal of Biomedical Materials Research Part A, Vol. 81B, pp. 410-418.

40. *Calcium orthophosphate cements for biomedical application.* Dorozhkin, S.V. 2008, Journal of Materials Science, Vol. 43, pp. 3028-3057.

41. L.C. Chow, L.D. Eanes. Octacalcium Phosphate. *Calcium phosphate cement.* Basel : Monogr Oral Sci, 2001, pp. 148-163.

42. *Next generation calcium phosphate-based biomaterials.* Chow, L. C. 2009, Dental materials, Vol. 28, pp. 1-10.

43. *Calcium phosphate bone cements for clinical applications - part i: solution chemistry.* E. Fernandez, F. J. Gil, M. P. Ginebra, F. Driessens, J. A. Planell, S. M. Best. 1999, Journal of Materials Science: Materials in Medicine, Vol. 10, pp. 169-176.

44. *Ionic modification of calcium phosphate cement viscosity. Part i: hypodermic injection and strength improvement of apatite cement.* U. Gbureck, J. E. Barralet, K. Spatz, L. M. Grover, R. Thull. 2004, Biomaterials, Vol. 25, pp. 2187-2195.

45. *High-strength apatitic cement by modification with α-hydroxy acid salts.* J. E. Barralet, M. Hofmann, L. M. Grover, U. Gbureck. 2003, Advanced Materials, Vol. 15, pp. 2091-2094.

46. *Preparation of macroporous calcium phosphate cement tissue engineering scaffold.* J. E. Barralet, L. Grover, T. Gaunt, A. J. Wright, I. R. Gibson. 2002, Biomaterials, Vol. 23, pp. 3063-3072.

47. *Reinforcement of a self-setting calcium phosphate cement with different fibers.* H. Xu, F. C. Eichmiller, A. A. Giuseppetti. 2000, Journal of Biomedical Materials Research Part A, Vol. 52, pp. 107-114.

48. *Development of a bovine collagen-apatitic calcium phosphate cement for potential fracture treatment through vertebroplasty.* R. M. O'Hara, J. F. Orr, F. J. Buchanan, R. K. Wilcox, D. C. Barton, N. J. Dunne. 2012, Acta Biomateralia, Vol. 8, pp. 4043-4052.

49. *Incorporation of biodegradable electrospun fibers into calcium phosphate cement for bone regeneration.* Y. Zuo, F. Yang, J. Wolke, Y. B. Li, J. A. Jansen. 2010, Acta Biomaterialia, Vol. 6, pp. 1238-1247.

50. *Fiber reinforced calcium phosphate cement.* L. A. Dos Santos, L. C. de Oliveira, E. Rigo, R. G. Carrodeguas, A. O. Boschi, A. de Arruda. 2000, Artificial Organs, Vol. 24, pp. 212-216.

51. Bouropoulos, N. Unpublished results.

52. Schizas, C. *Διερεύνηση κατασκευής βιο-συμβατής μικρο-βαλβίδας με τη μέθοδο της μικρο-στερεολιθογραφίας.* Piraeus : University of Piraeus, 2010.

53. *Phase development during setting and hardening of a bone cement based on α-tricalcium and octaplacium phosphates.* V.S Komlev, I.V. Fadeeva, S.M Barinov, J.V Rau, M. Fosca, A.N. Gurin, N.A Gurin. 2012, Journal of Biomaterial Applications, Vol. 26, pp. 1051-1068.

54. *Monitoring of hardening and hygroscopic induced strains in a calcium phosphate bone cement using FBG sensor.* A. Bimis, D. Karalekas, N. Bouropoulos, D. Mouzakis, S. Zaoutsos. 2016, Journal of the Mechanical Behavior of Biomedical Materials, Vol. 60, pp. 195-202.

55. *Simultaneous Incorporation of Carbonate and Fluoride in synthetic Apatites: Effect on Crystallograpgic and Physico-Chemical Properites.* F. Yao, J.P. LeGeros, R.Z. LeGeros. 2009, Acta Biomaterialia, Vol. 5, pp. 2169-2177.

56. *Guidelines for assessment of bone microstructure in rodents using micro-computed tomography.* M.L. Bouxsein, S.K. Boyd , B.A. Christiansen, R.E Guldberg, K.J. Jepsen, R. Müller. 2010, Journal of Bone and Mineral Research, Vol. 25, pp. 1468–1486.

57. *Effect of micro-computed tomography voxel size and segmentation method on trabecular bone microstructure measures in mice.* Christiansen, B. 2016, Bone Reports, Vol. 5, pp. 136–140.

58. *The coefficient of expansion of muscle.* Wilkie, D.R. 1953, The Journal of Physiology, Vol. 119, pp. 369-375.

59. Wikipedia. [Online] [Cited: October 23, 2016.] https://en.wikipedia.org/wiki/Confocal_microscopy.

60. *Modulation of porosity in apatitic cements by the use of a-tricalcium phosphate—calcium sulphate dihydrate mixtures.* E. Fernandez, M. D. Vlad, M. M. Gel, J. Lopez, R. Torres, J. V. Cauich, M. Bohner. 2005, Biomaterials, Vol. 26, pp. 3395–3404.

61. *Mechanical characterization of dense calcium phosphate bioceramics with interconnected porosity.* Y.H. Hsu, I.G Turner,A.W. Miles. 2007, Journal of Materials Science: Materials in Medicine, Vol. 18, pp. 2319-2329.

62. *Elaboration and characterization of nanostructured biocements for biomedical applications.* N.H.A Camargo, C. Soares , E. Gemelli. 2007, Journal of Material Research, Vol. 10, pp. 135-140.

63. *Mechanics of Biological Systems and Materials, Volume 4.* F. Barthelat, P. Zavattieri, C. S. Korach, B. C. Prorok, K. Jane Grande-Allen. 2013. Annual Conference on Experimental and Applied Mechanics.

64. *Spherical instrumented indentation of porous nanocrystalline zirconia.* R.K. Chintapalli, E. Jimenez-Pique, F.G. Marro, H. Yan, M. Reece, M. Anglada. 1, 2012, Journal of the European Ceramic Society, Vol. 32, pp. 123-132.

65. *An improved technique for determining hardness and elastic modulus using load and displacement sensing indentation experiments.* W. C Oliver, G. M. Pharr. 6, 1992, Journal of Materilas Research, Vol. 7, pp. 1564-1583.

66. *Depth-sensing indentation of low-density brittle nanoporous solids.* S.O. Kucheyev, A.V. Hamza, J.H. Satcher Jr., M.A. Worsley. 12, 2009, Acta Materialia, Vol. 57, pp. 3472-3480.

67. *Rational synthesis of a nanocrystalline calcium phosphate cement exhibited rapid conversion to hydroxyapatite.* I. S. Neira, Y. V. Kolenko, O. I. Lebedev, G. V. Tendeloo, H. S. Gupta, N. Matsushita, M. Yoshimura, F. Guitián. 7, 2009, Material Science and Engineering:C, Vol. 29, pp. 2124-2132.

68. *Mechanical characterization of brushite cements: a mohr circles' approach.* C. Pittet, J. Lemaitre. 2000, Journal of Biomedical Material Research, Vol. 53, pp. 769-780.

69. *The effects of temperature on the behaviour of an.* M.P. Ginebra, E. Fernadez, F.C.M. Driessens, M.G. Boltong, J. Muntasell, J. Font, J.A. Planell. 12, 1995, Journal of Materials Science: Materials in medicine, Vol. 6, pp. 857-860 .

70. *Injectable and rapid-setting calcium phosphate bone cement with dicalcium phosphate dihydrate.* E.F Burguera, H. Xu, M.D Weir. 2006, Journal of Biomedical Material Research, Vol. 77, pp. 126-134.

71. S. Timoshenko, J. N. Goodier. *Stresses in a circular disk.* New York : McGraw-Hill, 1951.

72. D3967-08, ASTM. Standard Test Method for Splitting Tensile Strength of Intact Rock Core Specimens. West Conshohocken, PA : ASTM International, 2008.

73. *On Coulomb's Law of Failure in Soils.* Shield, R.T. 1955, Journal of the Mechanics and Physics of Solids, Vol. 4, pp. 10-16.

74. *The Mohr-Coulomb criterion for intact rock strength and friction – a re-evaluation and consideration of failure under polyaxial stresses.* A. Hackston, E. Rutter. 2016, Solid Earth, Vol. 7, pp. 493-508.

75. *Study on internal friction angle and tensile strength of plain concrete.* Y. Fujita, R. Ishimaru, S. Hanai, Y.Suenaga. 1998. Fructure Mechanics of Concrete Structure Proceedings.

76. Massoudi, M. Constitutive modelling of flowing granular materials: A continuum approach. *Granular Materials: Fundamentals and Applications.* s.l. : Royal Society of Chemistry, 2004, pp. 63-107.

77. *The use offiber Bragg grating sensors in biomechanics and rehabili-tation applications: the state-of-the-art and ongoing researchtopics.* E. Al-Fakih, N.A.A Osman, F.R.M. Adikan. 2012, Sensors, Vol. 12, pp. 12890–12926.

78. Botsis, J. Fiber Bragg grating applied to in situ characterization of composites. [book auth.] John Botsis. *Wiley Encycplopedia of Composites.* New Work : Wiley, 2011, pp. 1-15.

79. *Assessment of thermoset cure-induced strains by fiber Bragg grating sensor.* L. Robert, G. Dusserre. 2013, Polymeric Engineering Science.

80. *On the effects of the lateral strains on the fiber Bragg grating response.* M. Lai, D. Karalekas, J. Botsis. 2013, Sensors, Vol. 13, pp. 2631-2644.

81. *Characterisation of residual stresses in a single fibre composite with FBG sensor.* F. Colpo, L. Humbert, J. Botsis. 9, 2007, Composites Science and Technology, Vol. 67, pp. 1830-1841.

82. *Dual-Configuration Fiber Bragg Grating SensorTechnique to Measure Coefficients of Thermal Expansion and Hygroscopic Swelling.* Y. Sun, Y. Wang, Y. Kim, B. Han. 2014, Experimental Mechanics, Vol. 54, pp. 593–603.

83. Lai, M. *Hygrothermal Ageing and Damage Characterization in Epoxies and in Epoxy-Glass Interfaces: a Micromechanical Approach Using Embedded Optical Sensors.* Lausanne : EPFL, 2011.

84. Measures, R.M. Structural monitoring with fiber optic technology. 2001.

85. Colpo, F. *Residual stress characterization in a single fibre composite specimen by using FBG sensor and the OLCR technique.* Lausanne : EPFL, 2006.

86. *Moisture diffusion in cementitious materials: Adsorption isotherms.* X. Yunping, PB Zdeněk , MJ Hamlin. 248-257, 1994, Advanced Cement Based Materials, Vol. 1.

87. *Dynamic determination of sorption isotherm of.* T. Shinsaku, W. Kazumasa. 2005, Cement and Concrete Research, Vol. 35, pp. 2271-2277.

88. Wikipedia. [Online] [Cited: 11 01, 2016.] https://en.wikipedia.org/wiki/Finite_difference_method.

89. University, Brigham Young. BYU Applied Biomechanics Engineering Laboratory. [Online] [Cited: December 23, 2016.] https://babel.byu.edu/content/lumbar-spine-fea.

90. *Anomalous Moisture Diffusion in an Epoxy Adhesive Detected by Magnetic Resonance Imaging.* G. LaPlante, A. V. Ouriadov, P. Lee-Sullivan, B. J. Balcom. 2008, Journal of Applied Polymer Science, Vol. 109, pp. 1350–1359.

91. Surgeons, American Academy of Orthopaedic. [En ligne] [Citation : 10 11 2016.] http://orthoinfo.aaos.org/topic.cfm?topic=a00377.

92. *Comparison of Mechanical Stress and Change in Bone Mineral Density Between Two Types of Femoral Implant Using Finite Element Analysis.* Y. Hirata, Y. Inaba, N. Kobayashi, H. Ike, H. Fujimaki, T. Saito. 2013, The Journal of Arthroplasty, Vol. 28, pp. 1731-1735.

93. *Three-dimensional finite element analyses of functionally gradedfemoral prostheses with different geometrical configurations.* A.A. Oshkour, N.A. Abu Osman, M. Bayat, R. Afshar, F. Berto. 2014, Materials and Design, Vol. 56, pp. 998-1008.

94. *Cement mantle fatigue failure in total hip replacement: Experimentaland computational testing.* J. R.T. Jeffers, M. Browne, A. B. Lennon,P. J. Prendergast, M. Taylor. 2007, Journal of Biomechanics , Vol. 40, pp. 1525–1533.

95. *Finite element and experimental models of cemented hipjoint reconstructions can produce similar bone and cement strainsin pre-clinical tests.* J. Stolk, N. Verdonschot, L. Cristofolini, A. Toni, R. Huiskes. 2002, Journal of Biomechanics, Vol. 35, pp. 499-510.

96. R. Hambli, N. Hattab. Application of Neural Network and Finite Element Method for Multiscale Prediction of Bone Fatigue Crack Growth in Cancellous Bone. *Multiscale Computer Modeling in Biomechanics and Biomedical Engineering.* s.l. : Springer Berlin Heidelberg, 2012, pp. 3-30.

97. *The elastic properties of hard tissues and apatites.* Dale, L. Katz, R. S. Gilmore, and R. Murty,. 3, 1972, Journal of Biomedical Materials Research, Vol. 6, pp. 221–233.

98. *Static, dynamic and fatigue behavior of newly designed stem shapes for hip prosthesis using finite element analysis.* A. Z. Senalp, O. Kayabasi, H. Kurtaran. 5, 2007, Materials & Design, Vol. 28, pp. 1577–1583.

99. *The effects of static, dynamic and fatigue behavior on three-dimensional shape optimization of hip prosthesis by finite element method.* O. Kayabasi, B. Ekici. 8, 2007, Materials and Design, Vol. 28, pp. 2269–2277.

100. *Cement mantle fatigue failure in total hip replacement: Experimentaland computational testing.* J. R.T. Jeffers, M. Browne, A. B. Lennon, P. J. Prendergast, M. Taylor. 2007, Journal of Biomechanics, Vol. 40, pp. 525–1533.